Toxic-Metal-Free Nanocrystals for Technological Applications

Panagiotis Rodosthenous

University of Leeds

School of Electronic and Electrical Engineering

Submitted in accordance with the requirements for the degree of

Doctor of Philosophy

30^{th} November 2021

Submitted in accordance with the requirements for the degree of Doctor of Philosophy.

The candidate confirms that the work submitted is his own, except where work which has formed part of jointly authored publications has been included. The contribution of the candidate and the other authors to this work has been explicitly indicated below. The candidate confirms that appropriate credit has been given within the thesis where reference has been made to the work of others.

The right of Panagiotis Rodosthenous to be identified as Author of this work has been asserted by Panagiotis Rodosthenous in accordance with the Copyright, Designs and Patents Act 1988.

We only regret the chances we didn't take.

Acknowledgements

It is my pleasure to express my gratitude to few, but important people who stood by me all these years, encouraging and guiding me through the completion of this project. I would like to thank my main supervisor Marco Califano for believing in me at the first place and who has always been supportive with my research. His vast knowledge on semiconductor physics, his ability to write scientific papers and his excellent computational skills were all a motivation and of assistance to me. I would also like to thank my secondary supervisor Francisco Gomez-Campos who always was willing to provide excellent discussions and clarifications on almost every theoretical aspect.

I would like to thank Grigorios Itskos from University of Cyprus, who gave me an opportunity for a conference talk and for his decisive advice.

It would be a shame not to thank my parents, who have never stopped believing in me and their support all these years was invaluable. I also thank the rest of my family, friends and people in my life.

I appreciate and thank the staff in our School and my colleagues, for the past 8 years that I have been there.

I gratefully acknowledge financial support from EPSRC through a Doctoral Training Grant.

I also acknowledge and thank Advanced Research Computing (ARC) resources. This work was undertaken on ARC3, part of the High Performance Computing facilities at the University of Leeds, UK.

Panagiotis Rodosthenous, November 2021

Abstract

Throughout the years, semiconductor NCs emerge to be promising building blocks for a wide range of applications due to their unique electronic and optical properties at nanoscale. Particularly, colloidal quantum dots (CQDs) have drawn the interest of researchers since, apart from their unprecedented size, shape-tunable and composition-dependent properties, require cheap and easy synthesis, making them preferable for device fabrication. However, the majority of the materials that are currently used are either toxic or heavy-metal-based, which limits the application of devices and their commercialization. Taking this into consideration, we decided to investigate new nanomaterials that fulfill a vital criterion: to be environmentally friendly, free of toxic or heavy-metal elements. In this way, their currently used counterparts can be replaced with these new materials and hence expand the commercialization of devices. The atomistic semi-empirical pseudopotential method (SEPM) is used for this investigation of mainly In-based and Ga-based materials. Our results are compared with available theoretical and experimental data. In this way, we enrich the knowledge on unexplained or insufficiently explained aspects in the properties of such NCs, proposing potential applications in realistic systems according to the calculated properties.

In this theoretical research we characterize a new nanomaterial that has not been synthesized before in colloidal form. GaSb colloidal QDs is an example of an environmentally friendly material that has high potential once synthesized. We predict a direct-to-indirect confinement-induced bandgap transition in the reciprocal space, at relatively large NC sizes ($R < 36\mathring{A}$) due to strong quantum confinement effects. We show that emission can be tuned throughout the visible spectrum and that is accompanied by large Stokes's shifts and long radiative lifetimes, attributed to the indirect nature of the bandgap. These results suggest that GaSb NCs can be ideal candidates in solar cells applications and memory storage, but most importantly, in a photocatalytic CO_2 reduction with water.

Additionally, our investigation included the modelling of InP NCs that have been widely used for decades in many applications. Considering the poor surface passivation of such NCs at the experimental level and that particular optical properties lack a satisfactory explanation, we applied the SEPM predicting an unprecedented relationship between the surface of the NC and the relative optical properties. By applying a newly derived passivation set achieving an ideally passivated surface, we show that colloidal InP NCs can still exhibit low QY, depending on their surface composition (i.e., to whether the surface is In- or P-rich), a prediction that gives new insights into the optical properties of this material and highlights the importance of NC surface.

We expanded our investigation to different structures: we modelled 2D QD films made of In-based and Ga-based materials, following an atomistic tight-binding model (TBM). We show how toxic-free NCs can find application in band-like carrier transport, proposing potential alternatives for specific toxic materials that are currently used. In this investigation we show how the NC composition and stoichiometry can enhance the carrier mobility and lead to QD films more resilient to temperature changes.

An ongoing investigation in the optical properties of GaP NCs showed that these NCs exhibit long radiative lifetimes and fast Auger recombination lifetimes. The aim of this work is to provide the first insights of such processes in GaP NCs, that are considered, among others, a potentially promising candidate for replacing toxic elements.

The purpose of this thesis is to provide useful information about the unique properties of environmentally friendly nanomaterials, with the main objective to help experimental groups to replace their toxic counterparts.

Abbreviations

CB	**C**onduction **B**and
CBM	**C**onduction **B**and **M**inimum
ARC3	**A**dvanced **R**esearch **C**omputing **3**
CI	**C**onfiguration **I**nteraction
CQD	**C**olloidal **Q**uantum **D**ot
DCM	**D**iret **C**arrier **M**ultiplication
DFT	**D**ensity **F**unctional **T**heory
EPM	**E**mpirical **P**seudopotential **M**ethod
FSM	**F**olded **S**pectrum **M**ethod
LED	**L**ight **E**mitting **D**iode
MBE	**M**olecular **B**eam **E**pitaxy
MOVPE	**M**etal**O**rganic **V**apour **P**hase **E**pitaxy
NC	**N**ano**C**rystal
PL	**P**hoto**L**uminescence
QD	**Q**uantum **D**ot
QY	**Q**uantum **Y**ield
SEPM	**S**emi **E**mpirical **P**seudopotential **M**ethod
SP	**S**ingle **P**article
TBM	**T**ight–**B**inding **M**odel
VB	**V**alence **B**and
VBM	**V**alence **B**and **M**aximum
WZ	**W**urt**Z**ite
ZB	**Z**inc**B**lende

List of publications [1]

1. Califano, M.; Rodosthenous, P. *Theoretical Characterization of GaSb Colloidal Quantum Dots and Their Application to Photocatalytic CO_2 Reduction with Water.*, ACS Appl. Mater. Interfaces **11**, 640−646 (2019).

2. Rodosthenous, P.; Gomez, F. M.; Califano, M. *Tuning the Radiative Lifetime in InP Colloidal Quantum Dots by Controlling the Surface Stoichiometry.*, J. Phys. Chem. Lett. **11**, 10124−10130 (2020).

3. Rodosthenous, P.; Skibinsky-Gitlin, E. S.; Rodríguez-Bolívar, S.; Califano, M.; Gómez-Campos, F. M. *Band-like Transport in 'Green' QD Films: The Effect of QD Composition and Stoichiometry.*, J. Chem. Phys. **156**, 2022

4. Hahn, R.; Rodríguez-Bolívar, S.; Rodosthenous, P.; Skibinsky-Gitlin, E. S.; Califano, M.; Gómez-Campos, F. M. *Optical Absorption in N-Dimensional Colloidal Quantum Dot Arrays: Influence of Stoichiometry and Applications in Intermediate Band Solar Cells.*, ACS Applied Nano Materials, 2022 (under review).

List of conference presentations [2]

1. Califano, M.; Rodosthenous, P. *Theoretical Characterization of GaSb Colloidal Quantum Dots and Their Application to Photocatalytic CO_2 Reduction with Water.* **Oral**, XXXIII Panhellenic Conference on Solid State Physics and Material Science XXXIII Materials 2018, Nicosia, Cyprus, 2018.

2. Gómez-Campos, F. M.; Skibinsky-Gitlin, E. S.; Rodríguez-Bolívar, S.; Califano, M.; Rodosthenous, P.; López-Villanueva, J. A.; Carceller, J. E. *Influence of dimensionality and stoichiometry in the electronic structure of InAs quantum dot solids.* **Contributed work**, 2021 13^{th} Spanish Conference on Electron Devices (CDE), Sevilla, Spain, 2021.

[1] Publications 1,2 and 3 are relevant for work presented in this thesis. Publication 4 is under review.

[2] Conference paper 1 is part of this thesis. Conference paper 2 is not presented in the thesis.

Contents

List of Figures

List of Tables

Chapter 1

Introduction

Throughout the years, technology has advanced to such a level that materials are studied at the nanoscale, exhibiting peculiar electronic and optical properties depending on shape, type of material, composition, stoichiometry and size. Semiconductor nanomaterials are particularly interesting as their tunable properties are beneficial to existing technological applications such as light emission, photovoltaics, imaging, photocatalysis, biomedicine, bio-imaging. However, many of these currently used nanomaterials contain toxic heavy metal elements which limit the commercialization of products or make them not environmentally friendly when it comes to their disposal. Having this in mind, in this project we aimed to find promising environmentally friendly materials with similar or better properties compared to the currently widely used toxic materials and propose possible replacement of those materials, resulting in toxic-free products. By using the state-of-the-art semiempirical pseudopotential method, we were able to characterize such nanocrystals, identifying their properties. In this chapter, we provide an introduction to colloidal NCs and their applications, addressing basic principles such as the quantum effect, coulomb exchange interaction and carrier multiplication.

1.1 Spherical Semiconductor NCs

Spherical nanocrystals (NCs), also known as quantum dots (QDs) or artificial atoms, have drawn the interest of researchers since their reduced dimensions

confine the carriers (electrons and holes) in all three directions yielding promising properties, which are different compared to the bulk. The NCs in this study are zero-dimensional (the electron's degrees of freedom are reduced to zero), which means that the quantum confinement effects are strong, making these NCs ideally suited for a range of applications[1]. However, many of the materials used so far limit the commercialization of products since either they are toxic, or they contain heavy metals[2]. Examples are Pb-based and Cd-based materials. Our research focused on the investigation of the electronic and optical properties of non-toxic nanomaterials and the identification of potential application according to the respective properties.

Different types of semiconductor QDs are the self-assembled quantum dots that are usually synthesized by molecular beam epitaxy (MBE) or metalorganic vapour phase epitaxy (MOVPE)[3], the electrostatic quantum dots[4], and the colloidal quantum dots[5]. The latter are considered to be particularly promising for a wide range of applications[6], due to the achievable small NC sizes and inorganic nature. Typically, colloidal NCs are synthesized in two steps: the nucleation of an 'initial' seed and the growth. The former involves the decomposition of the precursors, forming the monomers, followed by the nucleation of NCs. Then, the nuclei grow by incorporating existing monomers that are available in the solution. The system consists of three components, namely, the precursors, the organic surfactants and the solvents. The procedure is based on the heating of a reaction medium, where the precursors chemically transform into active atomic or molecular species (known as monomers). Subsequently, the monomers form the actual NCs. The growth of the NCs depends on the surfactant molecules presence in the solution[7]. Not only their cheap and easy synthesis but their size and shape tunable electronic and optical properties make these NCs ideal for lighting application, optoelectronics, photovoltaics and bio-labeling. Further, their size monodispersity (typically up to 5%) is also an advantage when it comes to the synthesis of NCs[8, 9, 10]. Another advantage is that their chemical flexibility allows the synthesis in different forms such as 3D superlattices, quantum dot molecules, closed-packed films, incorporation with high densities into sol gels, glasses, or polymers. Scientists found that the shape and size of such NCs affect their properties (e.g., emission at different wavelengths by different shaped and sized

NCs), which makes these NCs promising candidates for not only new applications but also for potential replacement of their existing toxic counterparts[11, 12, 13]. Our modeling approach gave us the required tools to fully understand and explain the behavior of these size-dependent properties for several nanomaterials.

1.2 Basic principles behind semiconductor NCs

1.2.1 Quantum confinement effect

Understanding the basic principles behind these interesting and promising properties of semiconductor NCs is crucial for the characterization of new materials with unprecedented properties. By substantially reducing the size of the material, unique properties arise due to the *quantum confinement* of the carriers[14, 15, 16] where the size of the NC becomes smaller compared to the wavelength of the electron. The NCs need to reach a size of few nanometers in order to experience this effect[17]. This effect derives from the particle-in-a-box formalism[18], which leads to an opening in the gap with decreasing size (increased confinement). Unlike in the bulk state, at the nanoscale the sizes of the structure is comparable or smaller than the exciton Bohr exciton radius (a_x). In general, the Bohr radius is defined as the separation between an electron-hole ($e-h$) pair in the bulk. At the nanoscale, however, the spatial extent of the $e-h$ pair state is defined by the dimensions of the actual NC. This leads to an increase in the Coulomb interaction due to the smaller e-h separation. Consequently, we have spatial confinement-dependent electronic properties, as shown in Fig. 1.1, where by controlling the NC dimensions we can achieve a tuning of the electronic energies.

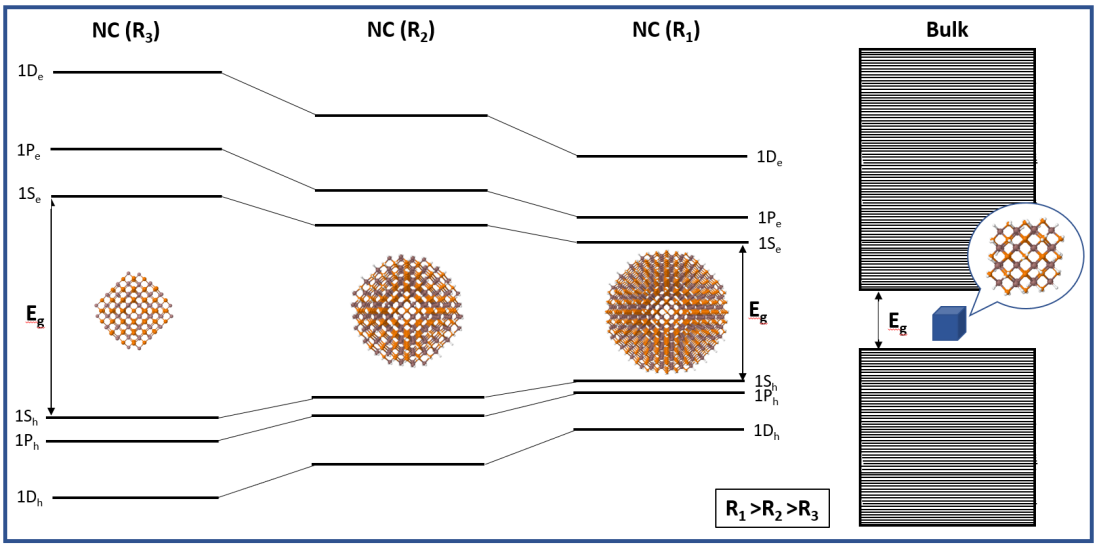

Figure 1.1: Illustration of the size effect and the resulting quantum confinement of carriers. The smaller the NC the larger the energy separation.

In the bulk state, there is no quantization of energy but only a fixed bandgap. As the dimensions are reduced, the NCs exhibit discrete energy levels, and a size-dependent bandgap[19, 20, 21]. The smaller the dimensions, the larger the energy separation and thus the bandgap (E_{CBM} - E_{VBM}). The quantized energy levels can be classified based on the angular momentum (l) of the envelope wave functions that includes information about the carrier movement in the low-dimensional confinement potential[22]. In a NC the state may be classified based on the symmetry and angular momentum (S for l=0, P for l=1 and D for l=2), following the order 1S,1P and 1D. In some cases, however, the symmetry of the band edges could have a p-like character instead of the expected s-like character[23, 24]. The symmetry of the single-particle states is important when it comes to the investigation of the origins of the respective optical transitions.

1.2.2 Coulomb and exchange interaction

Considering the small dimensions of structures, the carriers are confined to smaller scales compared to the Bohr radius which enhances greatly the Coulomb interactions[25]. This interaction energy can be quantified in terms of either the

biexciton binding energy (ϵ_{xx}) that shows the strength of the exciton-exciton interaction, or the exciton binding energy (ϵ_x) that corresponds to the strength of the $e-h$ pair interaction. With decreasing NC size, this interaction energy increases very fast[26], especially due to the reduced dielectric screening in small NC. Consequently, the Coulomb interaction energy could reach an increase of around 100 meV, yielding biexciton energies of around tens of meV[27, 28].

Apart from the Coulomb interaction, the *electron-hole* exchange interaction is an intrinsic property of NCs that determines the excitonic structure, including the ordering of the optically allowed (bright) and forbidden (dark) excitonic states[30]. This yields a size-dependent splitting in the absorbing and emitting states[31], determined by the electron-hole charge density overlap. Specifically, for InP this interaction is found to be inversely proportional to the square of the NC radius, as R^{-2}[29]. Consequently, this dark-bright splitting significantly affects the optical properties of band-edge excitons and, subsequently, the radiative and non-radiative decay rates. These processes are competitive and thus are particularly important especially for light-emitting applications. As a summary, the enhancement of the carrier Coulomb interactions in semiconductor NCs results in large splitting of electronic states (induced by e-h exchange interactions)[32], e-h energy transfer and thus efficient intraband relaxation[33], ultra-fast multiexciton Auger recombination[34] and efficient generation of multiple e-h pairs or multiexcitons coming from single photons through carrier multiplication (CM)[35]. CM, as will be explained further on, is significantly important for lasing[36] and photovoltaics[25, 37].

1.2.3 Direct carrier multiplication

Due to their size-tunable optical properties, colloidal NCs became attractive for applications in light-emitting diodes (LEDs), lasers, solar cells and solid-state lighting. However, the realization of such applications requires a thorough understanding of the interactions between carriers (Coulomb and exchange interactions) as they highly affect both the recombination and the photogeneration dynamics. Another interesting property of semiconductor NCs is carrier multiplication or direct carrier multiplication (DCM), which involves the direct photogeneration of

multiexctions by a single photon[38, 39]. This is considered as an Auger-like process involving the relaxation of a high-energy carrier with excess energy $\Delta E \geq \epsilon_g$ to the corresponding band edge, transferring this energy to an electron in the valence band exciting it to the conduction band. In the case of the absorption of a photon with energy $h\nu \geq 2\epsilon_g$, two electron-hole pairs (excitons) can be generated, as long as the excess energy is not dissipated as heat. This process is illustrated in Fig. 1.2.

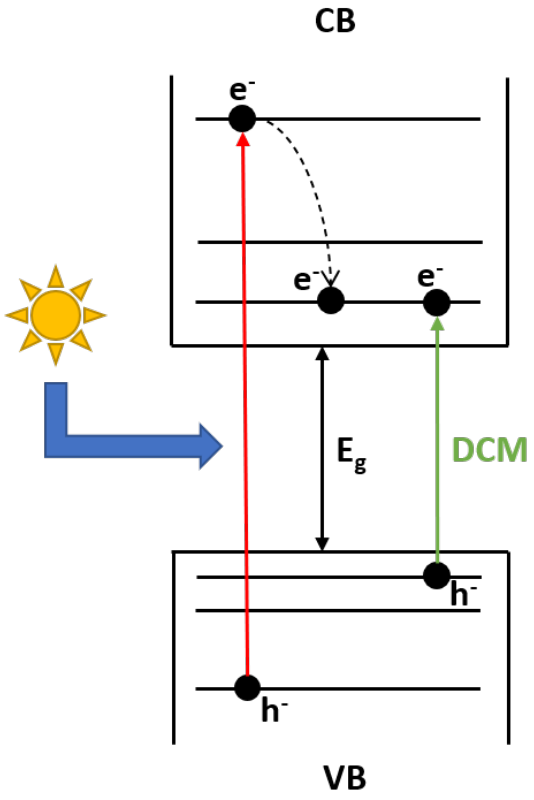

Figure 1.2: Direct carrier multiplication (DCM) and generation of second electron-hole pair with the excitiation of an electron from VB to CB.

Atomistic electronic structure calculations showed that DCM can be induced by electron-hole Coulomb interactions in an impact-ionization-like process. Additionally it was found that the most important factor for DCM efficiency is the degeneracy of the band edges, the higher the degeneracy of the CBM and VBM

the higher the DCM rates. Furthermore, the energy spacing between the CB minima at the high symmetry points (Γ, X, and L) of the bulk band structure is important for direct $\Gamma-\Gamma$ materials, since an electronic transition of the CBM character in the reciprocal space (e.g. Γ - L transition) can lead to higher DCM. Finally, it was found that the effective masses have a negligible effect on the DCM. These findings can be beneficial for the material choice when it comes to the fabrication of devices that benefit from DCM. Multiexciton generation is attributed to the confinement of carriers and increased Coulomb electron-hole interactions, which greatly increase the rate of exciton multiplication in semiconductor NCs. Such mechanisms are beneficial for photovoltaics and light-harvesting applications, since a higher solar cell power can be converted into current without reducing the open-circuit voltage, thus improving the overall efficiency. The inverse process is known as the Auger Recombination (AR) which is a non-radiative process and it constitutes the main limiting factor for the performance of lasers and LEDs[40]. Carrier multiplication in spherical NCs can be controlled with NC size and shape effect, interface engineering for suppressing the Auger decay[41]. It was previously shown that NC elongation is a promising approach for enhancing the CM efficiency by manipulating the strength of the carrier-carrier Coulomb coupling[42, 43].

1.3 Applications of semiconductor NCs

The size-, shape-tunable and stoichiometry-dependent electronic and optical properties of colloidal semiconductor NCs along with their easy and cheap chemical synthesis, make them promising candidates for a wide range of technological applications[1]. In addition to this, scientists nowadays tend to follow a new research route, involving the investigation of new emerging, environmentally friendly nanomaterials for potential replacement of the currently used toxic heavy metal materials, expanding the commercialization of devices[6]. Here, we present an overview on the applicability of such NCs in real world applications.

Colloidal nanomaterials are promising for light-emitting applications as they can be synthesized in high monodispersity and can be easily deposited in multilayers, enhancing the optical gain. The main light-emitting application is the

LEDs that benefit from such properties. Apart from the size-tunable emission throughout the whole visible spectra, these applications are favored by the suppression of the non-radiative processes (Auger) that limit the radiative recombination. In this regard, many studies have reported colloidal NCs ideal for reducing the non-radiative recombination rates by decreasing the overlap of electron and hole wave functions in real or reciprocal space[41] (which can also reduce the optical yield), or via dielectric screening[44], or by using weakly n-type HgSe colloidal quantum dots[45]. Colloidal NCs yield high efficiency in light emission[46, 47, 48, 49, 50, 167] and thus are preferred for such applications compared to epitaxial quantum dots. Furthermore, quantum dot lasers are used in medical, storage and data processing applications[52]. Colloidal NCs are beneficial for lasing applications due to the low optical-gain thresholds and high temperature stability of lasing characteristics[53, 54, 55, 56, 57]. This is an advantage compared to quantum well lasers[58] since the well-separated states in colloidal NCs are size-dependent, which means that at small sizes (where the confinement is stronger) the energy states are higher in energy compared to the thermal energy. Consequently, the thermal population of the lower states is reduced which leads to a temperature-independent threshold for lasers. One of the main properties of semiconductor NCs is the size-tunable emission, which in this case leads to a range of colours for lasers by engineering the NC size.

One of the main applications that benefit from the properties of colloidal semiconductor NCs is photovoltaics, where the solar cell efficiency can be greatly increased[59, 60, 61, 62]. The direct carrier multiplication in semiconductor NCs is highly enhanced compared to the bulk material, due to the strong confinement of carriers and stronger Coulomb interaction. The efficiency of such systems could be further improved if the material exhibits long recombination lifetimes, which gives a sufficient time window for the excited electrons to be collected and transferred to the electrodes before their recombination. Recently, it was found that perovskite semiconductor NCs could be considered as promising alternatives for increasing the efficiency of solar cells[63, 64, 65]. In addition, semiconductor NCs are widely used in multi-junction solar cells, where several materials with different bandgap (for absorbing a wide range wavelength of incoming radiation) are used to increase the photon absorption efficiency[66, 67, 68].

Colloidal semiconductor NCs are also used in 2D films, where the films are made from QDs with small interdot distances. In this way, the transport of carriers is achieved between the neighbouring dots via a band-like mechanism[69] that heavily depends on temperature and interdot distance. Two-dimensional QD arrays find applications in photovoltaics, LEDs, transistors[70]. Properties such as high carrier mobilities can help in the creation of higher performance devices. However, existing QD films are mainly made of toxic or heavy-metal-based materials, a factor that limits their commercialization. Consequently, researchers look for non-toxic alternatives, with similar or even better properties, to replace their currently used counterparts.

Nowadays, colloidal nanomaterials have been identified as ideal candidates for photocatalytic applications[71, 72, 73, 74, 75]. These NCs enable a variety of chemical transformations owing to their strong light-absorbing properties and high degree of size-, shape-, and composition-tunability. Additionally, they have performed well in homogeneous photoreduction reactions, including the degradation of organic dyes and hydrogen generation[76]. Such NCs are ideal for a wide range of photocatalytic reactions such as reductions, oxidation and redox reactions[77].

Semiconductor NCs are also used in quantum information processing[78, 79, 80, 81, 82, 83], biological and biomedical[84, 85, 86, 87, 88, 89] applications. Their photostability, broad absorption and narrow emission make these systems ideal fluorescent probes in biomedical and imaging applications. Such nanocrystals were previously used in an ultrasensitive biological labeling and multicolour optical encoding applications[90].

1.4 Thesis outline

Following this introduction section, the theoretical framework is explained thoroughly in Chapter 2. Specifically, the atomistic Semi-Empirical Pseudopotential Method (SEPM) is described, as it constitutes the base of our calculations of the electronic and optical properties of NCs. We explain how the semiconductor NCs and the actual pseudopotentials used in our calculations are created and how the single particle Schrodinger equation is solved by using the Folded Spectrum

Method (FSM) and how many-body effects leading to the excitonic structure are included. We then explain how the absorption and emission spectra, Stokes shifts, radiative and non-radiative lifetimes are calculated. Finally, the tight-binding model used to calculate the transport properties in 2D colloidal QD films is explained. In Chapter 3, our published work on the characterization of GaSb NCs is presented. This new nanomaterial, that has not been synthesized before in colloidal form, exhibit unprecedented electronic and optical properties due to its peculiar structure: the predicted confinement-induced direct-to-indirect bandgap transition yields large Stokes shifts, long radiative lifetimes and a size-tunable emission in the visible spectrum, which make this nanometarial an ideal candidate for photovoltaics, memory storage and most importantly photocalysis. Our research on InP NCs is presented in Chapter 4, where we investigate the effect of Phosphorous (P) atoms at the NC surface on the optical properties. We find that NCs with P-rich surfaces have faster radiative lifetimes and higher quantum yield (QY), explaining several experimental findings. As a consequence, we suggest that it is possible to modify the radiative lifetimes by manipulating the surface stoichiometry of the NCs. Our research on environmentally friendly NCs was expanded in the investigation of the transport properties in environmentally friendly 2D QD arrays. Chapter 5 presents our work on In-based and Ga-based QD films, promising for replacing their currently used Pb-based and Cd-based toxic counterparts. We calculate the mobility in such films by following an atomistic tight-binding model, taking into account the effect of increasing temperature and interdot distance. We show how the NC composition and stoichiometry affect the transport properties by performing a quantitative analysis on our results, linking our results with realistic systems. In Chapter 6 the ongoing investigation on GaP NCs and their optical properties is presented. We calculate the SP bandgap along with the corresponding optical properties for small NCs, which are compared with other non-toxic NCs. We find that GaP NCs exhibit long radiative lifetimes and fast Auger recombination lifetimes, both attributed to their indirect bandgap. We propose the continuation plan for this work. Finally, Chapter 7 presents the concluding remarks and future developments of this research.

Chapter 2

Theoretical Framework

This chapter will describe the theoretical framework that applies to all principles, methods, and calculations presented in this research. Starting from the state-of-the-art atomistic pseudopotential method we will give an insight into the calculation of the electronic and optical properties of the NCs. Furthermore, aspects regarding the generation of the NCs and the corresponding pseudopotentials will be discussed. In addition, the method for solving the single-particle problem, and subsequently the approach of taking into account the many-body effects will be explained. Next, the calculations of the optical properties (absorption and emission spectra, Stoke shifts, radiative and non-radiative lifetimes) will be described. Lastly, the tight-binding model used for the calculation of the transport properties in NC films will be explained.

2.1 Atomistic Semi-Empirical Pseudopotential Method

Methods based on atomistic first principles (*ab initio*), such as the density functional theory (DFT), have been developed over the years to effectively calculate the electronic and optical properties of structures at the nanoscale. However, these methods are unable to deal with systems including more than a few hundred atoms.

On the other hand, the semi-empirical pseudopotential method (SEPM) is based on a different approach, and follows the steps presented in Fig. 2.1. This method consists of three main components: (i) solving the single-particle Schrödinger equation, (ii) calculating the many-body effects, and (iii) calculating the optical properties of the NCs[91]. The first in the ground-state calculation, is the generation of the input geometry i.e., the construction of a supercell that contains the actual NC.

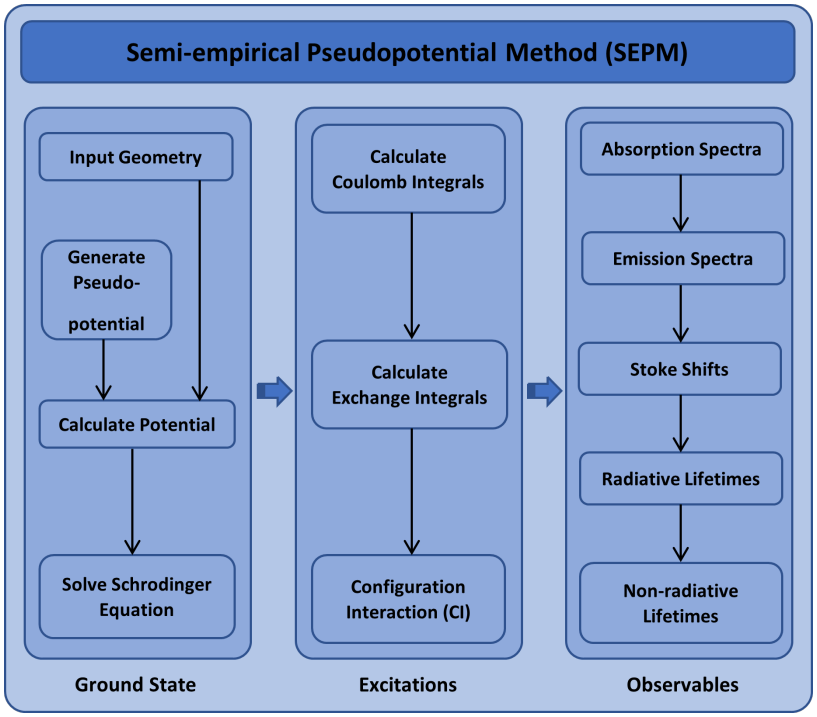

Figure 2.1: Flowchart of the steps followed to form the SEPM and result in the calculation of the electronic structure and optical properties.

The advantage of this approach compared to other methods such as the DFT[92, 93, 94] is that it can handle larger systems with more atoms. The next step is the generation of the empirical pseudopotentials for the specific material that are fitted to the experimental band structure and wavefunctions (more details will be given in the next subsection). Once the pseudopotentials are created, the total crystal potential can be calculated, defining the main parameters

for solving the single-particle Schrödinger equation by utilizing the Folded Spectrum Method (FSM). This method has the advantage of utilizing a reference energy in the electronic structure calculations, which, as it will be explained later on, gives the ability to calculate eigenstates near the CBM or VBM (according to where the reference energy is set). After obtaining the single-particle energies and wavefunctions, the excitations can be calculated. This is achieved by, firstly, calculating the Coulomb integrals and then the exchange integrals. Subsequently, the configuration interaction (CI) method is used to include many-body effects. The optical properties for a system with/without an electron-hole pair, such as absorption/emission spectra, radiative/non-radiative lifetimes can then be calculated.

2.2 Semicoductor NCs: How are they created?

The generation of the atomic positions, that form the actual spherical NCs or QDs, is the first step before any calculations. In our investigations, we considered both anion-centered and cation-centered spherical NCs with the zinc-blende crystal structure. The generation of the NC structures was achieved by adding atom layers up to a pre-specified cutoff radius r_{cutoff}. Surface atoms with 3 dangling bonds were removed as they are unstable for dissociation. The effective radius r_{eff} was determined as $r_{\text{eff}} = \text{a}(\gamma N_{\text{dot}})^{\frac{1}{3}}$, where a is the lattice constant, $\gamma = 3/(32\pi)$ for this crystal type (see Appendix 1) and N_{dot} is the number of atoms in the nanocrystal. Materials such as InP, GaSb, and GaP have different NC sizes for the same number of atoms due to the difference in their lattice constants.

2.3 Surface passivation

Once the atomic structures were created, the next step was to properly passivate their surface eliminating any unsaturated bonds. By following the procedure described by[95] we adjusted the passivation parameters to eliminate any trap states in the gap, according to the material and the corresponding atomic types. The unsaturated bonds at the dot surface are passivated here using pseudo-hydrogenic, short-range potentials with Gaussian form,

$$v(\mathbf{r}) = \alpha e^{-(|\mathbf{r}-\mathbf{R}(\gamma)|/\sigma)^2} \tag{2.1}$$

Each passivant is therefore characterized by (i) the amplitude α and (ii) the width σ of the Gaussian potential, and by (iii) the distance γd from the surface atom along the ideal bond line connecting it with the missing atom (d is the bond length and $\mathbf{R}(\gamma)$ is the ligand position) [95, 96, 97]. As the electronic structure calculations are performed in Fourier space, the real space parameters have associated q-space parameters and thus Eq. 2.1 needs to be Fourier transformed into [95]

$$v(\mathbf{q}) = \alpha\pi^{1.5}\sigma^3 e^{i\mathbf{q}\cdot\mathbf{R}} e^{-(\sigma|\mathbf{q}|/2)^2} \tag{2.2}$$

to obtain the relationship between real-space parameters and q-space ones (which are the actual input to the calculations): $a = \alpha\pi^{1.5}\sigma^3$, $b = \sigma/2$, and $c = \gamma$.

2.4 Pseudopotentials: How are they created?

One of the main advantages of the SEPM, compared to other well-known methods (such as the effective-mass approximation and the $\mathbf{k}\cdot\mathbf{p}$ method), is its atomistic approach that takes into account the atomistic nature of semiconductor NCs[91].

We start with the most general, time-dependent Schrödinger equation, that describes a system that evolves with time and is given by

$$i\hbar\frac{d}{dt} \mid \Psi(t)\rangle = \hat{H} \mid \Psi(t)\rangle \tag{2.3}$$

where $\mid \Psi(t)\rangle$ is the state vector of the system and $\hat{H}$ is the Hamiltonian operator. Considering the particle in three-dimensions, Eq. 2.3 can be expressed as

$$i\hbar\frac{d\psi(\mathbf{r},t)}{dt} = -\frac{\hbar^2}{2m}\nabla^2\psi(\mathbf{r},t) + V(\mathbf{r})\psi(\mathbf{r},t) \tag{2.4}$$

where V is a real function and stands for the potential energy. This time-dependent form is then used to derive the time-independent equation (that will be used in this work), by expressing the wavefuntion as the product $\psi(\mathbf{r},t) = \psi(\mathbf{r})f(t)$. Then, the time-dependent equation becomes

$$\psi(\mathbf{r})i\hbar\frac{df(t)}{dt} = f(t)\left[-\frac{\hbar^2}{2m}\nabla^2 + V(\mathbf{r})\right]\psi(\mathbf{r}). \tag{2.5}$$

Rearranging Eq. 2.5, we get

$$\frac{i\hbar}{f(t)}\frac{df}{dt} = \frac{1}{\psi(\mathbf{r})}\left[-\frac{\hbar^2}{2m}\nabla^2 + V(\mathbf{r})\right]\psi(\mathbf{r}). \tag{2.6}$$

In this way, the left side is time-dependent and the right side is time-independent. From that we can extract the time-independent Schrödinger equation assuming $f(t) = e^{(-i\epsilon t/\hbar)}$, yielding

$$-\frac{\hbar^2}{2m}\nabla^2\psi(\mathbf{r}) + V(\mathbf{r})\psi(\mathbf{r}) = \epsilon\psi(\mathbf{r}) \tag{2.7}$$

Solving for a solid, the Hamiltonian ($\hat{H}$) of the following form is considered

$$\hat{H} = \hat{H}_{elec} + \hat{H}_{nuc} + \hat{H}_{elec-nuc}, \tag{2.8}$$

where $\hat{H}_{elec}$ is the Hamiltonian for the electrons and is illustrated as

$$\hat{H}_{elec} = \sum_{\mu}\left(-\frac{\hbar^2}{2m_0}\nabla_{\mu}^2 + \sum_{\lambda<\mu}\frac{1}{4\pi\epsilon_0}\frac{e^2}{\mid \mathbf{r}_{\lambda} - \mathbf{r}_{\mu} \mid}\right) \tag{2.9}$$

and $\hat{H}_{nuc}$ is the Hamiltonian for the nuclei, illustrated as

$$\hat{H}_{nuc} = \sum_{n}\left(-\frac{\hbar^2}{2M_n}\nabla_{n}^2 + \sum_{\lambda<n}\frac{1}{4\pi\epsilon_0}\frac{Z_{\lambda}Z_n e^2}{\mid \mathbf{R}_{\lambda} - \mathbf{R}_{n} \mid}\right) \tag{2.10}$$

where $\mathbf{r}_{\lambda}$ represents the position of the electrons, m_0 represents the electron effective mass, ϵ_0 is the vacuum permittivity, $\mathbf{R}_n$ are the positions of the nuclei, Z_n are the atomic numbers and M_n is the mass of the nuclei.

Finally,

$$\hat{H}_{elec-nuc} = \sum_{\mu,n}\left(\frac{1}{4\pi\epsilon_0}\frac{Z_n e^2}{\mid \mathbf{R}_n - \mathbf{r}_{\mu} \mid}\right) \tag{2.11}$$

Dealing with the complete Hamiltonian, however, could lead to a complicated, insolvable situation especially when the system has a huge count of electrons. This problem could be addressed with the *frozen core* approximation, which is considered the foundation of the pseudopotential theory. Specifically, the Hamiltonian, as illustrated in Eq. 2.8 is simplified by assuming the existence of core electrons and valence electrons in the system. In more detail, the core

electrons are localized in the core region (inner-shell) and are imperturbable since they are tightly bound to the nucleus. On the other hand, the valence electrons are considered to be localized on the outer shell (non-local) interacting with neighboring potentials, thus forming an inter-atomic binding. Assuming that between the two types of electrons, only the latter is important for the calculations, the Schrödinger equation can be simplified since a reduced number of particles is considered. In addition to this, the core electrons screen the valence electrons from the charge of the central nucleus, which leads to a smoothing of the potentials. This is particularly important since smoother potentials mean fewer terms in the generation of the wavefunctions through a Fourier series calculation. Additionally, the adiabatic approximation allows the decoupling of nuclei and electron motions, since there is no energy transfer to electrons in the case of a change in the nucleus coordinates. Finally, the electron-electron interactions are replaced by a time-averaged potential through the independent electron approximation. Consequently, the complete Hamiltonian is simplified to a one-electron problem with the form

$$\hat{H} = -\frac{\hbar^2}{2m_0}\nabla^2 + V_c \tag{2.12}$$

For this research, we used semi-empirical pseudopotentials (thus SEPM). This method is essentially an improvement of the empirical pseudopotential method (EPM). This improvement was implemented by Wang and Zunger[98] in 1995, when they came up with a two-step process. Firstly, they created spherically symmetric and structurally averaged atomic potentials (SLDA) by inverting the self-consistently screened local-density-approximation (LDA) potentials for a range of bulk crystal structures and unit cell volumes. As a result, they could reproduce the LDA band energies and wavefunctions with high accuracy for widely used structures. Secondly, by adjusting the potentials they managed to achieve a fitting of the bulk band structure to the experimental excitation energies measurements. This adjustment of the potentials involved a small perturbation over the SLDA potential, preserving the wave function overlap with the original LDA values. Consequently, they presented a new way of combining LDA wavefunctions with excitation energies, effective masses, and deformation potentials coming from

experimental environments. In this method, a representation of the total system potential is achieved by a superposition of non-self-consistent screened pseudopotentials. The reciprocal space pseudopotential $V(G)$ is fitted to quantities like effective masses of bulk material, bandgap, etc that were measured experimentally, assuming that the total crystal screened pseudopotential is expressed as a superposition of atomically screened potentials $\upsilon_\alpha(\mathbf{r})$ at sites R_n for atom type α:

$$V(\mathbf{r}) = \sum_{\alpha,j,n} \upsilon_\alpha(\mathbf{r} - \mathbf{R}_n - \mathbf{r}_{\alpha,j}) \tag{2.13}$$

where n represents the index for the primitive unit cells and $r_{\alpha,j}$ is the basis vector for atom j in unit cell n. Considering only one type of atoms, the potential can be expressed in reciprocal space as

$$V(\mathbf{r}) = \sum_G \upsilon(\mathbf{G}) S(\mathbf{G}) e^{i\mathbf{G}\mathbf{r}} \tag{2.14}$$

where

$$S(\mathbf{G}) = \frac{1}{n} \sum_j e^{-i\mathbf{G}\mathbf{r}_j} \tag{2.15}$$

where n corresponds to the number of basis atoms. $S(\mathbf{G})$ is known as the *structure factor* that is geometry-dependent. The pseudopotential $\upsilon(\mathbf{G})$ can be expressed in the reciprocal space as

$$\upsilon_\alpha(q) = \alpha_1 \frac{(q^2 - \alpha_2)}{\alpha_3 e^{\alpha_4 q^2} - 1} \tag{2.16}$$

where α_1, α_2, α_3, α_4 represent adjustable parameters that are used to fit and reproduce known experimental quantities, as mentioned above, at different k-points and along different reciprocal space directions.

SEPM is a much better method compared to EPM which sometimes results in inaccurate wavefunctions, and focuses on a specific crystal structure and lattice constant, where the crystal potential fits the single-particle excitation spectra. On the other hand, the SEPM can reproduce experimental measurements of excitation energies and it can be used for a variety of structures, lattice constants, and a large number of atoms.

2.5 Solution of the single particle problem

2.5.1 Single-particle Schrödinger equation

Once the total potential for the NC is calculated, the following step is the solution of the single-particle problem. The single-particle Schrödinger equation is given by

$$\left(-\frac{\hbar^2}{2m_0}\nabla^2 + V_{ps}^{SEPM}(\mathbf{r}) + \hat{V}_{nl}\right)\psi_i(\mathbf{r}) = e_i\psi_i(\mathbf{r}) \tag{2.17}$$

where $V_{ps}^{SEPM}(\mathbf{r})$ is the microscopic total local pseudopotential (dot and surrounding) and is calculated as shown in Eq. 2.13, and $\hat{V}_{nl}$ is the non-local potential (including the spin-orbit coupling). $V_{ps}^{SEPM}(\mathbf{r})$ is calculated from the superposition of the screened atomic potentials in Eq. 2.13.

2.5.2 Folded Spectrum Method

The conventional variational method for solving the Hamiltonian in Eq. 2.17 involves the minimization of the energy $\langle\psi \mid \hat{H} \mid \psi\rangle$ by varying the expansion coefficients of ψ. The first ψ obtained in the state with the lowest energy. The calculation of higher energy states requires their orthogonalisation to all the energy states below them. These calculations, however, demand high computational resources since they scale as N^3 (N represents the total number of atoms in the system).

The folded spectrum method was initially introduced by Wang and Zunger [99, 100] in 1983, aiming to simplify the existing approach for solving the Hamiltonian (Eq. 2.17). The FSM tackled the single-particle problem[91] as it did not require the solution of the whole matrix: By placing a reference energy (energy of interest) somewhere close to the bulk CBM or VBM and choosing the number of states to be calculated, the eigenvalues near the band edges can be obtained. The calculation, in this case, scales linearly with the system's size, thus requiring less computational effort and processing time (since we do not need to calculate the wavefunctions of all the states below that energy). This method has the same solutions as Eq. 2.17, which also satisfy

$$\left(-\frac{\hbar^2}{2m_0}\nabla^2 + V_{ps}^{SEPM}(\mathbf{r}) + \hat{V}_{nl} - E_{ref}\right)^2 \psi_i(\mathbf{r}) = (E_i - E_{ref})^2 \psi_i(\mathbf{r}) \tag{2.18}$$

where E_{ref} is an arbitrary reference energy. As shown in Fig. 2.2, by folding the spectrum E_i of $\hat{H}$ at the reference energy E_{ref} in $(E_i - E_{ref})^2$ of $(\hat{H} - E_{\text{ref}})^2$ and placing that reference energy within the bandgap, the arbitrary eigen-solution becomes the lowest one, removing the need of the orthogonalisation. If E_{ref} is closer to the CBM or VBM energy, then the resulting eigenstates will be located in CB or VB accordingly, including the band edges. Compared to other methods where the lowermost energy state in the calculation is the deepest VB state, the folding of the energy spectrum in FSM yields the VBM or the CBM as the lowermost energy states, as shown in Fig. 2.2.

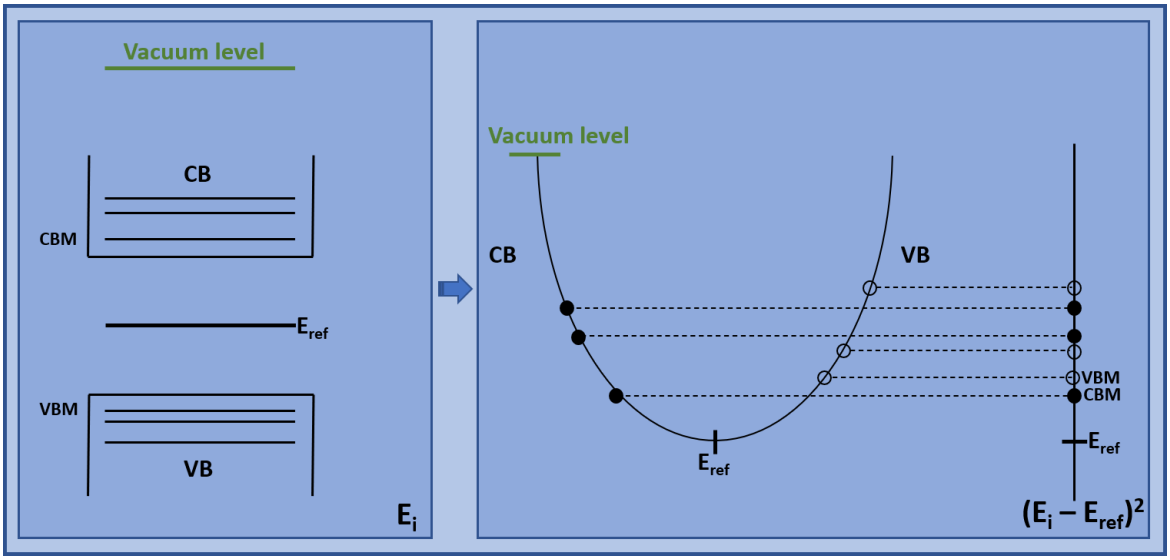

Figure 2.2: Folded Spectrum Method representation. The black-filled dots are CB states while the empty dots are VB states. The left panel shows the original energy spectrum of $\hat{H}$. The right panel represents the folded spectrum of $(\hat{H} - E_{ref})^2$ where either the CBM or the VBM would be the lowest energy state, depending on the position of the reference energy.

2.6 Many-body effects

After solving the single-particle Schrödinger equation, the *two-body* electron-hole problem is next to deal with. Once this step is completed, the excitonic structure can be calculated along with the optical properties of the NC. In such a system quantum correlations are created from the repeated interactions between particles, leading to complex wavefunctions with a huge amount of information. To be able to work with such wavefunctions, a few approximations need to be taken into consideration so to simplify the problem.

Firstly, the construction of the correlated exciton wavefunctions is achieved by using a set of single-substitution Slater determinants $\Phi_{v,c}$ obtained from the ground state Slater determinant Φ_0 by promoting an electron from an occupied valence state ψ_v to an unoccupied conduction state ψ_c. Subsequently, the exciton wavefunctions can be constructed as

$$\Phi_0(\mathbf{r}_1, \sigma_1, ..., \mathbf{r}_N, \sigma_N) = \xi[\psi_1(\mathbf{r}_1, \sigma_1)...\psi_v(\mathbf{r}_v, \sigma_v)...\psi_N(\mathbf{r}_N, \sigma_N)] \tag{2.19}$$

$$\Phi_{v,c}(\mathbf{r}_1, \sigma_1, ..., \mathbf{r}_N, \sigma_N) = \xi[\psi_1(\mathbf{r}_1, \sigma_1)...\psi_c(\mathbf{r}_v, \sigma_v)...\psi_N(\mathbf{r}_N, \sigma_N)] \tag{2.20}$$

where $\sigma = \uparrow$ or $\downarrow$ denotes the spin variables, N represents the total number of electrons and ξ is the antisymmetrizing operator. According to the Pauli exclusion principle, any multiparticle electronic wave function becomes anti-symmetric in the exchange of two electrons, lowering the total energy of the system. Two Slater determinants Φ_{v_1,c_1},Φ_{v_2,c_2} belong to the same configuration if both the single-particle valence states ψ_{v1} and ψ_{v2} as well as the single-particle conduction states ψ_{c1} and ψ_{c2} are degenerate. This leads to exciton configurations with at least a dimension of four (as each single-particle state is at least two fold degenerate, including spin). The wave function Ψ^α for the exciton is expressed in terms of the basis set as

$$\Psi^\alpha = \sum_{v=1}^{N_v} \sum_{c=1}^{N_c} C_{v,c}^\alpha \Phi_{v,c} \tag{2.21}$$

where N_v and N_c are the number of valence and conduction states respectively. Additional multi-exciton levels of higher energy would be observed if multi-substitution Slater-determinants are included in the calculations.

The matrix elements of the many-body Hamiltonian an this basis set are calculated as

$$\hat{H}_{vc,v'c'} = \langle \Phi_{v,c} | \hat{H} | \Phi_{v',c'} \rangle = (\epsilon_c - \epsilon_v)\delta_{v,v'c,c'} - J_{vc,v',c'} + K_{vc,v',c'} \tag{2.22}$$

where J and K represent the following direct and exchange integrals

$$J_{vc,v',c'} = e^2 \sum_{\sigma_1,\sigma_2} \int\int \frac{\psi^*_{v'}(\mathbf{r}_1,\sigma_1)\psi^*_c(\mathbf{r}_2\sigma_2)\psi_v(\mathbf{r}_1,\sigma_1)\psi_{c'}(\mathbf{r}_2,\sigma_2)d\mathbf{r}_1 d\mathbf{r}_2}{\bar{\epsilon}(\mathbf{r}_1,\mathbf{2}_2)|\mathbf{r}_1 - \mathbf{r}_2|} \tag{2.23}$$

$$K_{vc,v',c'} = e^2 \sum_{\sigma_1,\sigma_2} \int\int \frac{\psi^*_{v'}(\mathbf{r}_1,\sigma_1)\psi^*_c(\mathbf{r}_2\sigma_2)\psi_{c'}(\mathbf{r}_1,\sigma_1)\psi_v(\mathbf{r}_2,\sigma_2)d\mathbf{r}_1 d\mathbf{r}_2}{\bar{\epsilon}(\mathbf{r}_1,\mathbf{2}_2)|\mathbf{r}_1 - \mathbf{r}_2|} \tag{2.24}$$

One of the most important aspects of these calculations is the configuration interaction (CI) scheme. The CI is often treated at the level of triplets, quadruplets, all the way to the full CI. Neglecting the coupling of singles to higher excitations is considered a poor approximation. However, it was previously shown that the effect of higher-order excitations can be folded back to the subspace of the single excitations [101]. This approach leads to the renormalization (screening) of the Coulomb interactions shown above. For this research, a position-dependent dielectric function is used where the Coulomb and exchange interactions in the NC are screened based on the electron-hole separation [91], expressed as

$$g(\mathbf{r}_e,\mathbf{r}_h) = e^2 \int \epsilon^{-1}(\mathbf{r}_e,\mathbf{r})|\mathbf{r} - \mathbf{r}_h|^{-1} d\mathbf{r} \tag{2.25}$$

where ϵ^{-1} is the inverse dielectric function. With the assumption that $\epsilon^{-1}(\mathbf{r}_e,\mathbf{r}) \approx \epsilon^{-1}(\mathbf{r}_e - \mathbf{r})$, the Fourier transform of the screened potential becomes

$$g(\mathbf{k}) = \epsilon^{-1}(\mathbf{k})\frac{4\pi e^2}{\mathbf{k}^2} \tag{2.26}$$

where $\epsilon^{-1}(\mathbf{k})$ corresponds to the Fourier transform of $\epsilon^{-1}(\mathbf{r}_e - \mathbf{r})$. An electronic (high-frequency) ϵ_{el}^{-1} contribution and an ionic (low-frequency) contribution ϵ_{ion}^{-1} form the inverse dielectric function $\epsilon^{-1} = \epsilon_{el}^{-1} + \epsilon_{ion}^{-1}$, which we approximate using the Thomas-Fermi model by Rest and the polaronic model by Haken, respectively.

$$\epsilon_{el}^{-1}(\mathbf{k}) = \frac{\mathbf{k}^2 + \mathbf{q}^2 sin(\mathbf{k}\rho_\infty)/(\epsilon_\infty^{dot}\mathbf{k}\rho_\infty)}{\mathbf{k}^2 + \mathbf{q}^2} \tag{2.27}$$

$$\epsilon_{ion}^{-1}(\mathbf{k}) = \left(\frac{1}{\epsilon_0^{dot}} - \frac{1}{\epsilon_\infty^{dot}}\right)\left(\frac{1/2}{1+\rho_h^2\mathbf{k}^2} + \frac{1/2}{1+\rho_e^2\mathbf{k}^2}\right), \tag{2.28}$$

where $\mathbf{q}$ is the Thomas-Fermi wavevector defined as $\mathbf{q} = 2\pi^{-\frac{1}{2}}(3\pi^2 n_0)^{\frac{1}{3}}$, N_0 is the electron density, ρ_∞ is the solution of $sinh(\mathbf{q}\rho_\infty)/(\mathbf{q}\rho_\infty) = \epsilon_\infty^{dot}$, $\rho_{h,e} = (\hbar/2m_{h,e}^*\omega_{LO})^{\frac{1}{2}}$, where $m_{h,e}^*$ are the electron and hole effective masses and ω_{LO} to the frequency of the bulk LO-photon.

The low-frequency component is calculated as

$$\epsilon_0^{dot} - \epsilon_\infty^{dot} = \epsilon_0^{bulk} - \epsilon_\infty^{bulk} = \Delta\epsilon_{ion}^{bulk} \tag{2.29}$$

The high frequency component ϵ_∞^{dot} is calculated based on the Penn model as

$$\epsilon_\infty^{dot} = 1 + (\epsilon_\infty^{bulk} - 1)\frac{(\epsilon_{gap}^{bulk} + \Delta)^2}{(\epsilon_{gap}^{dot}(R) + \Delta)^2} \tag{2.30}$$

where $\Delta = \epsilon_2 - \epsilon_{gap}^{bulk}$ and ϵ_2 represents the second strongest peak from the measured bulk absorption spectrum. An advantage of our approach, compared to conventional effective mass and tight-binding methods (where the electron-hole exchange interaction was either unscreened or screened by the bulk distance-dependent dielectric constant), is that the dielectric function used here depends on the electron-hole separation and the NC size.

The exciton states in a NC are calculated by solving the secular expression

$$\sum_{v'=1}^{N_v}\sum_{c'=1}^{N_c} H_{vc,v'c'}C_{v',c'}^{(\alpha)} = E^{(\alpha)}C_{v,c}^{(\alpha)} \tag{2.31}$$

Diagonalization of the Hamiltonian (H) matrix gives the CI spectrum and therefore the dipole matrix elements for the optical inter-band absorption can be calculated as

$$M^{(\alpha)} = \sum_{v,c} C_{v,c}^{(\alpha)}\langle\psi_v|\mathbf{r}|\psi_c\rangle \tag{2.32}$$

where $C_{v,c}^{(\alpha)}$ are the exciton wave function expansion coefficients.

In Fig. 2.3, the single-particle and excitonic structures are presented. The ground state $|0h, 0e\rangle$ is assumed to be the zero point of the energy. Different materials might have different electronic structures at the single-particle (SP) level and thus different excitonic structures. For example, InP spherical NCs have a nondegenerate e_1 (CBM) SP state and a doubly-degenerate $h_{1,2}$ (VBM) SP state. This corresponds to a lowermost, eight-fold degenerate exciton ($4 \times 2 = 8$) including spin.

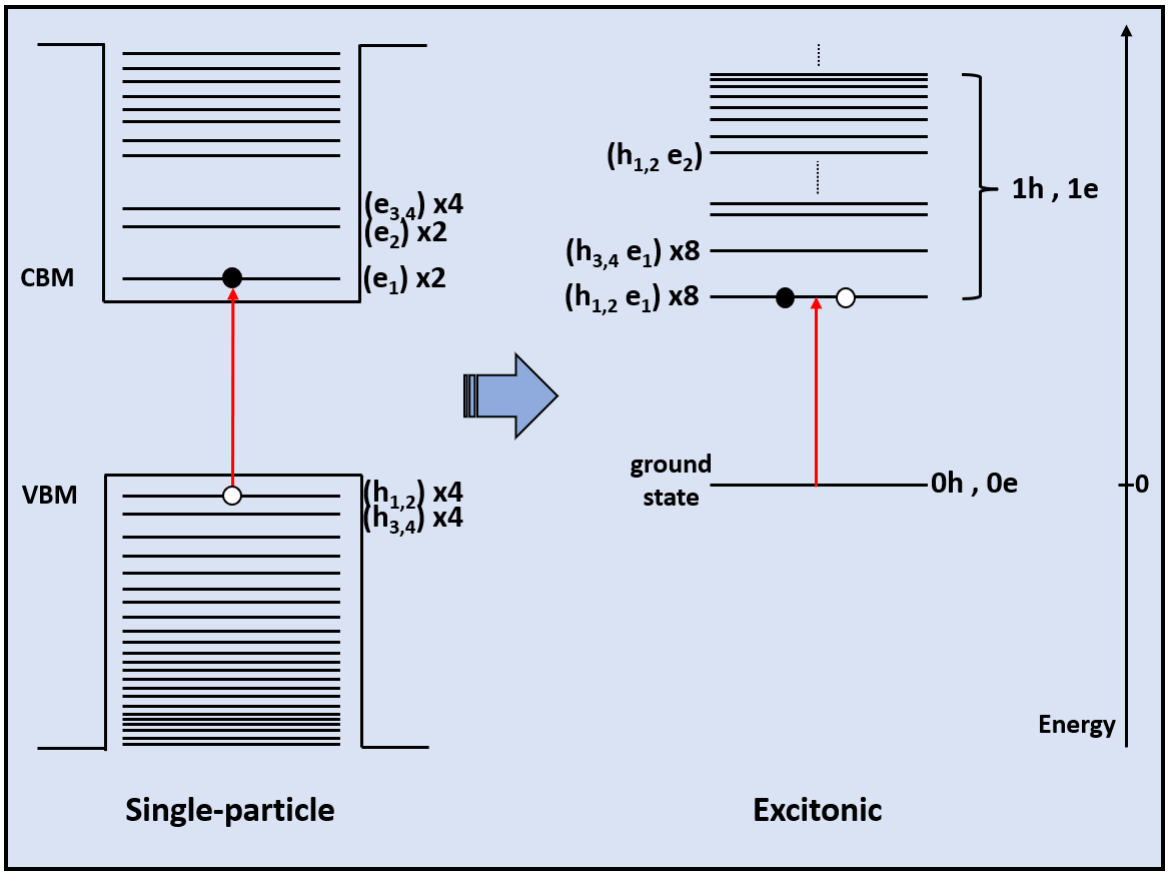

Figure 2.3: Single-particle (left) and excitonic structures (right).

2.7 Optical properties

2.7.1 Absorption and emission spectra

Once the dipole matrix elements are calculated, observables can be calculated by utilizing the post-processing tools. The absorption spectrum can then be calculated as

$$I(E) = \frac{1}{V} \sum_{\alpha} \mid M^{(\alpha)} \mid^2 e^{-\left(\frac{E-E^{(\alpha)}}{\Gamma}\right)^2} \tag{2.33}$$

where $E^{(\alpha)}$ is the excitation energy, $M^{(\alpha)}$ are the dipole matrix elements (Eq. 2.32) and Γ is the experimental line broadening. The absorption and emission spectra are calculated using the excitonic states. The single particle structure cannot be disregarded though, as it is more intuitive. Additionally, single configurations contribute to the excitonic states and thus it is important to include the SP spectra as it gives the ability to see from which SP states the excitons originate, by tracing the origin of transitions between the SP states involved in the formation of the excitons.

2.7.2 Stokes shift

Considering a photon absorption in a NC, if the absorbed photon has larger energy than the emitted photon then the difference between the two energies is known as the Stokes shift. This is presented in Fig.2.4(B), illustrating a Stokes shift (E_{abs} - E_{PL}). On the other hand, the non-resonant Stokes shift[102] refers to the case where the excitation energy is larger than the bandgap. This feature was observed in many studies regarding QDs[102, 103, 104, 105, 106, 107], where is was attributed to the size variation of NCs in experimental samples. In this research we focused on single QDs of different sizes, finding that the smaller the NC the larger the Stokes shift. This trend can be justified with the diagram of Fig. 2.4(A) where the fast (E_{fast}), high-energy, allowed state, and the slow (E_{slow}), forbidden state are illustrated. In small NCs the electron-hole exchange interaction is found to be increased, splitting the electron-hole state into lower energy, spin-forbidden state E_{slow} and a spin-allowed state E_{fast}, higher in energy.

The redshift between absorption and emission is the exchange splitting in this case. The spin-forbidden nature of E_{slow} leads to long radiative lifetimes.

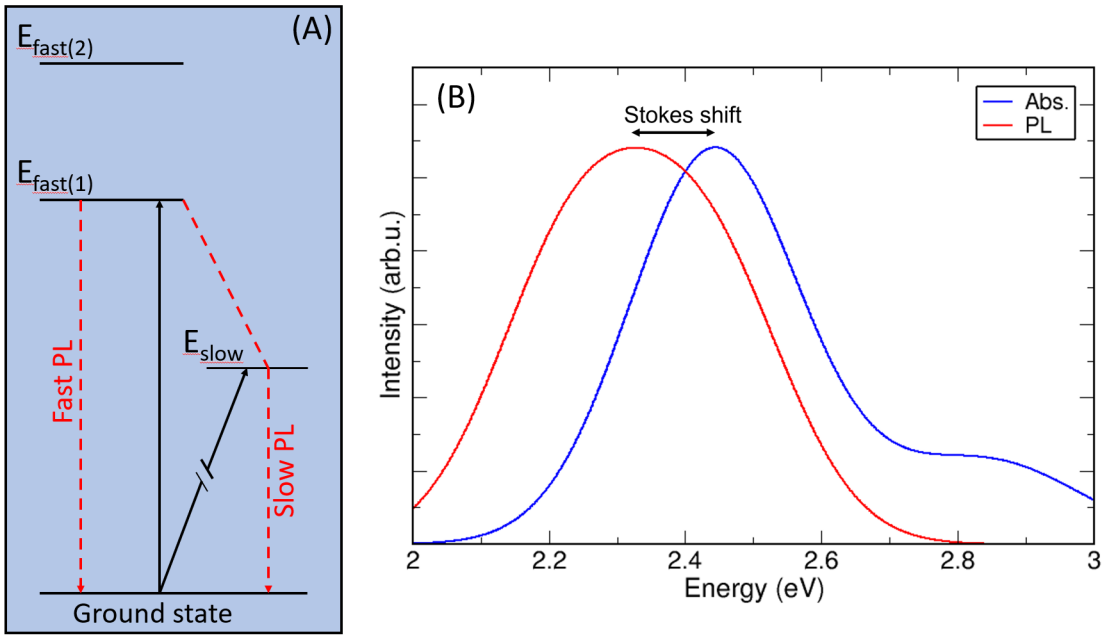

Figure 2.4: (A) Absorption (black) and emission (dashed red) representation and (B) Absorption and emission spectra for a NC. The difference between the absorption and emission peaks is known as the Stokes shift.

2.7.3 Radiative lifetimes

The thermally averaged lifetimes are calculated assuming Boltzmann occupation of higher-energy excitonic states, separated by an energy ΔE_γ, as

$$\frac{1}{\tau_R(T)} = \frac{\Sigma_\gamma (1/\tau_\gamma) e^{-\Delta E_\gamma / k_B T}}{\Sigma_\gamma e^{-\Delta E_\gamma / k_B T}} \tag{2.34}$$

where the radiative lifetime τ_γ for the transition from the excitonic state Ψ_γ to the ground state is obtained in the framework of time-dependent perturbation theory as

$$\frac{1}{\tau_\gamma} = \frac{4nF^2\alpha\omega_\gamma^3}{3c^2 \left|M_\gamma\right|^2}, \tag{2.35}$$

α is the fine structure constant, $\hbar\omega_\gamma$ is the transition energy, c is the speed of light in vacuum, $\mid M_\gamma \mid$ is the dipole matrix element of the excitonic transition, n is the refractive index of the surrounding medium, $F = 3\epsilon/(\epsilon_{dot} + 2\epsilon)$ is the screening factor, $(\epsilon = n^2)$, and ϵ_{dot} is the dielectric constant of the nanocrystal which is calculated using a modified Penn model [29].

2.7.4 Non-radiative lifetimes

Auger decay times are calculated within the standard time-dependent perturbation theory according to the formalism developed in ref.[108]

$$(\tau_{\mathrm{A}})_i^{-1} = \frac{\Gamma}{\hbar} \sum_n \frac{|\langle i|\Delta H|f_n\rangle|^2}{(E_{f_n} - E_i)^2 + (\Gamma/2)^2}. \tag{2.36}$$

where $|i\rangle$ and $|f_n\rangle$ are the initial and final states, E_i and E_{f_n} are their energies, ΔH is the screened Coulomb interaction and $\hbar/\Gamma$ is the lifetime of the final states (Γ = 10 meV was used here[109]). The regional screening introduced in the calculation of the Auger integrals in [108] was adopted in this work. Considering the importance of determining whether the main contribution to a particular Coulomb integral (and thus Auger process) comes from the interior of the NC or the NC surface, the following dielectric screening function was used:

$$\epsilon^{-1}(\mathbf{r}, \mathbf{r}') = \epsilon_{out}^{-1}(\mathbf{r}, \mathbf{r}') + \Big(\epsilon_{in}^{-1}(\mathbf{r}, \mathbf{r}') - \epsilon_{out}^{-1}(\mathbf{r}, \mathbf{r}')\Big) m(\mathbf{r}) m(\mathbf{r}'), \tag{2.37}$$

where $m(r)$ represents a mask function with a smooth change from 1, when r is inside the dot ($r < R_{dot} - d$), to 0, when r is outside ($r > R_{dot} + d$). Therefore, $\epsilon(\mathbf{r}, \mathbf{r}')$ is equal to (i) ϵ_{in} inside the dot; and (ii) ϵ_{out} when r or r' or both are outside. For this research, a value of 2.5 (representative of most capping groups and solvents) was assumed for the dielectric constant outside the dot. Typical capping agents that are used in colloidal synthesis involve heteroatom functionalized long-chain hydrocarbons. A few examples are: hexadecyl amine (HDA), oleic acid and linolenic acid, tri-n-octylphosphene (TOPO), thiols, biodegradable polymers, and enzymes[110]. Table 2.1 presents examples of capping groups and solvents with a dielectric constant close to 2.5 that are used experimentally[111].

Capping group/solvent	Dielectric Constant
TOLUENE	2.38
TRIOCTYLPHOSPHINE OXIDE (TOPO)	2.2

Table 2.1: Experimental capping groups and solvents with dielectric constant of around 2.5.

2.8 Tight-Binding Model

This specific tight-binding model was developed in collaboration with researchers from the University of Granada, Spain. Our collaboration throughout this research was fruitful since we used this model to investigate the transport properties of environmentally friendly QD films such as In-based (InAs, InP, and InSb) and Ga-based (GaSb) 2D QD films. This approach considers the collective behavior of quantum dots in an array and it could be used in systems with electrons tightly bound to the ions[112, 113]. The electronic structure, electron transport, and photon absorption can be computed for both finite and infinite systems. The resulting eigenfunctions depend critically on the distance between the QDs in the array.

2.8.1 Overview

Starting with the set of superlattice vectors R_v, the periodic potential, that has interaction with the electrons, can be generated by summing the isolated dot potentials. Thus, the Hamiltonian H_{tb} of the system is found to be

$$\begin{aligned} H_{tb} &= \frac{p^2}{2m_e} + \sum_{R_v} V(\mathbf{r} - \mathbf{R}_v) \\ &= \frac{p^2}{2m_e} + V(\mathbf{r}) + \sum_{R_v \neq 0} V(\mathbf{r} - \mathbf{R}_v) \\ &= H_{at} + \sum_{R_v \neq 0} V(\mathbf{r} - \mathbf{R}_v) \end{aligned} \tag{2.38}$$

where m_e represents the rest electron mass, $V(\mathbf{r} - \mathbf{R}_v)$ is the potential of the dot at R_v and H_{at} is the Hamiltonian of the isolated dot, as shown in Eq. 2.17

Assuming that the contribution of the neighboring QD potentials is small, the isolated QD wavefunctions, that strongly decay with distance R_v, can be used to solve the Hamiltonian, giving the solution

$$\psi_m(\mathbf{r}) = \sum_{n,\mathbf{R}_s} b_{m,n}(\mathbf{R}_s)\phi_n(\mathbf{r} - \mathbf{R}_s). \tag{2.39}$$

where m indicates the *m-th* solution to the Hamiltonian, $b_{m,n}(\mathbf{R}_s)$ are the expansion coefficients for that solution at position $\mathbf{R}_s$ and ϕ_n is the *n-th* wave function of the QD.

Then, the Hamiltonian is applied and the equation to be solved is formed

$$\left[H_{at} + \sum_{\mathbf{R}_v \neq 0} V(\mathbf{r} - \mathbf{R}_v)\right]\left[\sum_{n,\mathbf{R}_s} b_{m,n}(\mathbf{R}_s)\phi_n(\mathbf{r} - \mathbf{R}_s)\right] = E_m\left[\sum_{n,\mathbf{R}_s} b_{m,n}(\mathbf{R}_s)\phi_n(\mathbf{r} - \mathbf{R}_s)\right] \tag{2.40}$$

where E_m is the energy of the wave function ψ_m.

2.8.2 Periodic Systems

For periodic systems, the wave function must follow the Bloch theorem which states that

$$\psi_m(\mathbf{r} + \mathbf{R}_v) = \psi_m(\mathbf{r})e^{i\mathbf{q}\mathbf{R}_v} \tag{2.41}$$

which can be rearranged to

$$\psi_m(\mathbf{r}) = \frac{1}{\sqrt{N}} U_{m,\mathbf{q}}(\mathbf{r})e^{i\mathbf{q}\mathbf{r}} \tag{2.42}$$

where $\mathbf{q}$ represents a vector in the Brillouin zone of the reciprocal space, N is the number of unit cells and $U_{m,\mathbf{q}}(\mathbf{R})$ function describes the periodicity of the lattice.

This theorem can then be applied to Eq. 2.39, giving

$$\psi_m(\mathbf{r} + \mathbf{R}_m) = \sum_{n,\mathbf{R}_s} b_{m,n}(\mathbf{R}_s)\phi_n(\mathbf{r} - \mathbf{R}_s + \mathbf{R}_m) \tag{2.43}$$

and according to the definition of

$$\mathbf{R}_p = \mathbf{R}_s - \mathbf{R}_m \tag{2.44}$$

we get that

$$\begin{aligned}\psi_m(\mathbf{r}+\mathbf{R}_m) &= \sum_{n,\mathbf{R}_p} b_{m,n}(\mathbf{R}_m+\mathbf{R}_p)\phi_n(\mathbf{r}-\mathbf{R}_p) \\ &= \sum_{n,\mathbf{R}_p} b_{m,n}(\mathbf{R}_p)\phi_n(\mathbf{r}-\mathbf{R}_p)e^{i\mathbf{q}\mathbf{R}_m}\end{aligned} \tag{2.45}$$

Rewriting the expansion coefficients as a function of $\mathbf{R}_p$ at $\mathbf{R}_p = 0$, we obtain

$$b_{m,\mathbf{q},n}(\mathbf{R}_p) = b_{m,\mathbf{q},n}(0)e^{i\mathbf{q}\mathbf{R}_p} \tag{2.46}$$

The wave function depends on $\mathbf{q}$ (vector in the Brillouin zone of the reciprocal space), thus

$$\psi_m(\mathbf{r}) = \sum_{n,\mathbf{R}_s} b_{m,\mathbf{q},n}e^{i\mathbf{q}\mathbf{R}_s}\phi_n(\mathbf{r}-\mathbf{R}_s) \tag{2.47}$$

Therefore, applying the Hamiltonian we get

$$\begin{aligned}H_{tb}|\psi_{m,\mathbf{q}}(\mathbf{r})\rangle &= \sum_{n,\mathbf{q}} b_{m,\mathbf{q},n}e^{i\mathbf{q}\mathbf{R}_s}\left\{\frac{p^2}{2m_e}+\sum_{\mathbf{R}_v}V(\mathbf{r}-\mathbf{R}_v)\right\}|\phi_n(\mathbf{r}-\mathbf{R}_s)\rangle \\ &= E_{m,\mathbf{q}}\sum_{n,\mathbf{R}_s} b_{m,\mathbf{q},n}e^{i\mathbf{q}\mathbf{R}_s}\phi_t(\mathbf{r})|\phi_n(\mathbf{r}-\mathbf{R}_s)\rangle\end{aligned} \tag{2.48}$$

and

$$A_{\mathbf{q}}b_{m,\mathbf{q}} = E_{m,\mathbf{q}}B_{\mathbf{q}}b_{m,\mathbf{q}} \tag{2.49}$$

$A_{\mathbf{q}}$ and $B_{\mathbf{q}}$ are matrices of $M \times M$ dimension. At this points, a diagonalization problem occurs. For a certain value of $\mathbf{q}$, the wave functions become orthogonal after diagonalization, thus giving different eigenenergies. Sweeping the values of $\mathbf{q}$ gives the energy bands of the periodic system. Another approximation that is needed here is the use of only the nearest neighbors in the calculations so to have finite summations over $\mathbf{R}_v$ and $\mathbf{R}_s$.

Finally, the normalization is calculated with the overlap of

$$\begin{aligned}\langle\psi_{m,\mathbf{q}}(\mathbf{r})|\psi_{m,\mathbf{q}}(\mathbf{r})\rangle &= \sum_{n,\mathbf{R}_s}\sum_{n',\mathbf{R}'_s} b^*_{m,\mathbf{q},n}b_{m,\mathbf{q},n'}e^{i\mathbf{q}(\mathbf{R}_s-\mathbf{R}'_s)}\langle\phi_n(\mathbf{r}-\mathbf{R}_s)|\phi_{n'}(\mathbf{r}-\mathbf{R}'_s)\rangle \\ &= \sum_{n,\mathbf{R}_s}\sum_{n',\mathbf{R}_p} b^*_{m,\mathbf{q},n}b_{m,\mathbf{q},n'}e^{i\mathbf{q}(\mathbf{R}_p)}\langle\phi_n(\mathbf{r}-\mathbf{R}_s)|\phi_{n'}(\mathbf{r}+\mathbf{R}_p-\mathbf{R}_s)\rangle \\ &= N\sum_{n}\sum_{n',\mathbf{R}_p} b^*_{m,\mathbf{q},n}b_{m,\mathbf{q},n'}e^{i\mathbf{q}(\mathbf{R}_p)}\langle\phi_n(\mathbf{r})|\phi_{n'}(\mathbf{r}+\mathbf{R}_p)\rangle = NK_{m,\mathbf{q}} = 1\end{aligned} \tag{2.50}$$

where N is the number of unit cells $K_{m,\mathbf{q}}$ is the wave function normalization and is defined as

$$\begin{aligned} K_{m,\mathbf{q}} &\equiv \sum_{n} \sum_{n',\mathbf{R}_p} b^*_{m,\mathbf{q},n} b_{m,\mathbf{q},n'} e^{i\mathbf{q}(\mathbf{R}_p)} \langle \phi_n(\mathbf{r}) | \phi_{n'}(\mathbf{r}+\mathbf{R}_p) \rangle \\ \psi(\mathbf{r}_{m,\mathbf{q}}) &= \frac{1}{\sqrt{NK_{m,\mathbf{q}}}} \sum_{n,\mathbf{R}_s} b_{m,\mathbf{q},n} e^{i\mathbf{q}(\mathbf{R}_s)} \phi_n(\mathbf{r}-\mathbf{R}_s) \end{aligned} \tag{2.51}$$

The normalization in this case affects only the tight-binding coefficients. Consequently, $\psi_{n,\mathbf{q}}(\mathbf{r})$ is the normalized version of the wave function that was used earlier.

2.8.3 Mobility Model

This process is followed so to calculate the transport properties, such as the mobility. The mechanisms involved in carrier transport are controversial. One of the approaches is to model carrier transport by hopping, which involves the phonon interaction with electrons and how their energy is altered in order to *hop* between dots, as shown in Fig. 2.5. As a consequence, by increasing the temperature we increase the electron-phonon scattering[114, 115] and thus the mobility of electrons. The difference in energy between different sized QDs in the array is known as the activation energy E_α which is the required energy for an electron to move from one dot to another. The mobility in such systems is calculated by

$$\mu = \frac{ed^2 E_\alpha}{3\hbar kT} \tau e^{-E_\alpha/kT} \tag{2.52}$$

where e stands for the fundamental charge, d is the distance between the centers of QDs, T is the temperature, τ is the transmission coefficient in a single conductance channel and $\hbar$ is the Planck's constant. The mobility is calculated by considering a Boltzmann occupation of states, $e^{-E_\alpha/kT}$, where E_α is the energy and k is the Boltzmann's constant. The transmission coefficient here depends on the degree of coherence between initial and final hopping states (for example if the line width of the states is broader than the coupling, then the coherence is lost).

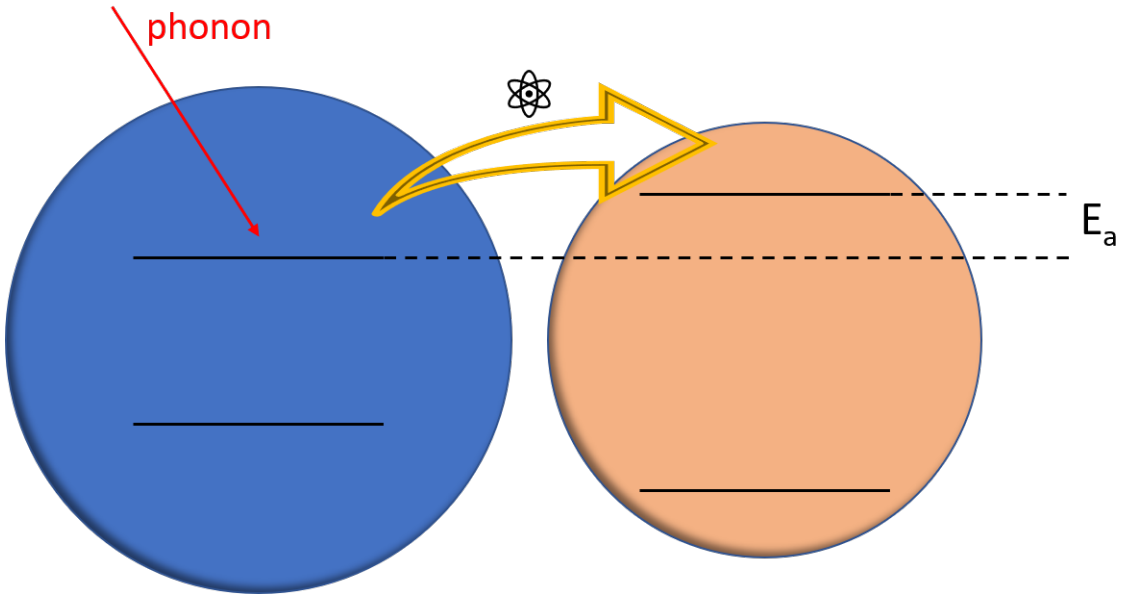

Figure 2.5: Representation of the hopping effect between quantum dots with different size.

Another approach is the band-like transport, where a two-dimensional periodic superlattice is considered in order to calculate the mobility in the miniband model. Here, a fraction of the QDs in the array have a smaller size compared to the periodic ones, known as impurity dots responsible for the scattering of electrons. The array regimentation leads to the formation of a band structure from the isolated QDs states (miniband structure due to the narrower bandwidths). By relating the electron energy E with the carrier's reciprocal vector $\mathbf{q}$, the velocity of an electron state in real-space can be expressed as

$$v(\mathbf{q}_{f\,m}) = \frac{1}{\hbar}\nabla_{\mathbf{q}} E_m(\mathbf{q})\Big|_{\mathbf{q}_f} \tag{2.53}$$

where v stands for the electron velocity, $\mathbf{q}_f$ is the reciprocal space vector after drift by the applied electric field and m is the miniband with the electron.

In band-like transport, the mobility reduces with increasing temperature. Although, this could be the case in hopping transport when a reduced temperature range is considered. However, the periodic QD regimentation along with the reduced interdot distances and reduced ligand size is closer to the experimental

trend. From that point of view, we decided to adopt the band-like transport mechanism. This model simulates the transport of electrons in the lowest conduction energy miniband, which is found to be distant from the next miniband. It is considered as the miniband with the higher occupation, thus making it the miniband of interest in transport calculations.

Such mechanisms interrupt the carrier movement prompting to start the acceleration process from the beginning. We are interested in the time between two consecutive scattering events, known as *time of flight* (TOF). The impurity dots used here have very similar energies with the periodic ones since they are only a bit smaller in size but of the same material. Their concentration was assumed to be 1% of the total number of QDs. The scattering rate can be obtained from the superlattice eigenstates $|\psi_{\mathbf{q}}(\mathbf{r})\rangle$ and the difference between the non-periodic $V_d(\mathbf{r})$ and periodic $V(\mathbf{r})$ QD potentials, $\Delta V(\mathbf{r}) = V_d(\mathbf{r}) - V(\mathbf{r})$.

We used Fermi's Golden Rule to calculate the scattering rates, and therefore the variation in the Hamiltonian is needed (ΔV):

$$\Gamma_{i,f} = \frac{2\pi}{\hbar}|\langle\psi_{c,q_f}|\Delta V|\psi_{c,q_i}\rangle|^2\rho(E_f) \tag{2.54}$$

where ρ stands for the superlattice density of states and $\Gamma_{i,f}$ is the scattering rate between the *i-th* to the *f-th* states.

In this model, for a finite discretization the continuous form of the density of states changes to a series of Dirac deltas, $(E) \rightarrow \sum_{E_f} \delta(E - E_f)$. This delta can be approximated to a window function of ΔE width, known as the *energy conservation window*, subdividing the miniband in N different energy levels with amplitude ΔE. Those levels are known as the *energetic intervals*. The scattering mechanism considered here conserves the energy.

Thus, Fermi's Golden Rule needs to rearranged accordingly by adding (i) the total number of impurity dots (N_i), (ii) the impurity concentration in the superlattice ($\nu = \frac{N_i}{N}$) and (iii) the ratio between the QDs number and the discretization space ($\frac{N}{Q_s}$), such as

$$\Gamma_{i,f} = \frac{\nu}{Q_s}\frac{2\pi}{\hbar}\frac{1}{\Delta E}\frac{1}{K_{c,q_i}K_{c,q_f}}\left|\sum_{m,s} b^*_{cmq_f} b_{csq_i}\int \psi^*_m(\mathbf{r})\Delta V(\mathbf{r})\phi_s(\mathbf{r})d\mathbf{r}\right|^2 \tag{2.55}$$

where $\Gamma_{i,f}$ is the scattering rate from the *i-th* to the *f-th* state and is obtained from the superlattice eigenstates $|\psi_{\mathbf{q}}(\mathbf{r})\rangle$, $\Delta V(\mathbf{r})$ is defined as the difference between the non-periodic QD potential $V_d(\mathbf{r})$, and the periodic one $V(\mathbf{r})$, K_{c,q_i} and K_{c,q_f} are the wave function normalization, $b^*_{cmq_f}$ and b_{csq_i} are the sets of coefficients used in the expansion and $\psi^*_m(\mathbf{r})$ is the normalized version of the wave function. The next important aspect to take into consideration is the calculation of the probability of the occupation of each state, after any number of scattering events. The scattering rates can be presented in a matrix form (of non-zero elements) as

$$\Gamma = \begin{bmatrix} \Gamma_{0,0} & \Gamma_{0,1} & \dots & \Gamma_{0,n-1} \\ \Gamma_{1,0} & \Gamma_{1,1} & \dots & \Gamma_{1,n-1} \\ \vdots & \vdots & \ddots & \vdots \\ \Gamma_{n-1,0} & \Gamma_{n-1,1} & \dots & \Gamma_{n-1,n-1} \end{bmatrix} \tag{2.56}$$

where n corresponds to the number of states for each energy interval. This is known as the probability matrix $\mathbf{P}$ (matrix Γ in Eq. 2.56). Consequently, the probability of ending the flight from state i to state f is given by

$$P_{i,f} = \frac{\Gamma_{i,f}}{\sum_{f'} \Gamma_{i,f'}} \tag{2.57}$$

Additionally, the occupation state vector is defined as

$$S = \begin{bmatrix} S_0 \\ S_1 \\ \vdots \\ S_{n-1} \end{bmatrix} \tag{2.58}$$

where S_i shows the probability that the *i-th* state is occupied by an electron.

The calculation of the probability of the occupation of each state, after any number of scattering events can be achieved by utilizing the Markov chain[116], where we multiply the probability matrix until the terms in the matrix converge. Here, there is no dependency on the initial state occupation and this can simplify the probability matrix to one dimension. The average time of flight (TOF) is calculated by

$$\langle t_i \rangle = \frac{1}{\sum_f \Gamma_{i,f}} \tag{2.59}$$

From the scattering probabilities from each *i-th* state to each *f-th* state it is possible to compute the probability matrix for a Markovian process[116]. From it, the probability of starting a flight from each particular state in the energy interval, P_i, can be obtained (see Eq. 2.57).

By applying an electric field the carriers experience changes in their crystal momentum $\mathbf{q}$, as

$$\mathbf{q}_f(t) = \mathbf{q}_i - \frac{e}{\hbar} E \langle t_i \rangle \tag{2.60}$$

where e stands for the elementary charge and E is the applied electric field. We used an electric field of 1×10^3, as we found it to be low enough to compute ohmic mobility and high enough to avoid numerical instabilities.

The average velocity for each energy interval can be calculated by

$$\begin{aligned} \langle v \rangle_j &= \frac{\langle \Delta R \rangle}{\langle t \rangle} = \frac{\sum_n v_n t_n}{\sum_n t_n} \\ &= \frac{\sum_i F \hat{P}_i v_i \langle t_i \rangle}{\sum_i F \hat{P}_i \langle t_i \rangle} = \frac{\sum_i \hat{P}_i v_i \langle t_i \rangle}{\sum_i \hat{P}_i \langle t_i \rangle} \end{aligned} \tag{2.61}$$

where j represents the energy interval, n is a counter for all flights within the electron scattering time and i is a counter for of the initial states in the considered energy interval. According to Markov chain, the number of times the electron starts a flight from state i is equal to the total flights F times the probability for the electron to start a flight at state i. $\langle \Delta R \rangle$ corresponds to the total displacement in the average velocity calculation.

The velocity can be used to compute the electric mobility, which is considered as a tensor quantity. Thus, the relationship is formed as

$$\begin{bmatrix} v1 \\ v2 \end{bmatrix}_i = \begin{bmatrix} \mu 11 & \mu 12 \\ \mu 21 & \mu 22 \end{bmatrix}_i \begin{bmatrix} E1 \\ E2 \end{bmatrix} \tag{2.62}$$

where the indices 1 and 2 indicate the direction of the lattice vectors, i corresponds to the i_{th} energy interval, $v_{1,2}$ are the velocities, $\mu_{l,m}$ represents the tensor matrix elements for the mobility and $E_{1,2}$ stands for the electric field. Therefore, the mobility can be written in terms of temperature, by using the previously introduced Fermi-Dirac distribution:

$$\hat{\mu}(T, E_F) = \frac{\sum_i F(E_i, E_F, T) n_i \hat{\mu}_i}{\sum_i F(E_i, E_F, T) n_i} \tag{2.63}$$

where $F(E_i, E_F, T)$ indicates the Fermi-Dirac distribution at energy E_i for a given Fermi energy level E_F and temperature T. The number of reciprocal space vectors in the *i-th* energy interval is shown by n_i and it is proportional to the density of states.

2.9 Conclusions

The basic theoretical framework behind this research was described in detail in this chapter, starting from the SEPM that, compared to *ab initio* and other atomistic approaches, has many advantages. It uses the geometry of the structures as input to the calculations. Additionally, it is an empirical approach, meaning that experimental data are considered and the results are closer to what is observed experimentally. Then, the procedure for the generation of the NCs was described along with the approach to properly passivate these structures with the use of Gaussian potentials. The creation of the atomic pseudopotentials was then described which would then lead to the calculation of the total crystal potential and thus the solution of the single-particle Schrödinger equation and the calculation of the eigenstates. This calculation is based on the FSM, which gives the ability to calculate states around the desired energy, without calculating the whole energy spectrum. Then, the solution to the many-body effects problem was discussed along with how the optical properties of NCs are computed. Properties such as absorption and emission spectra, Stokes shifts, radiative and non-radiative lifetimes were considered. Finally, the tight-binding model that was used for the calculation of the transport properties of QD films was analyzed. In the following chapters, we apply the various approaches discussed here to spherical GaSb NCs (Chapter 3,) spherical InP NCs (Chapter 4), QD films (Chapter 5), and spherical GaP NCs (Chapter 6).

Chapter 3

Spherical GaSb NCs

In this chapter, the characterization of a new, unsynthesized nanomaterial is presented. By using the atomistic pseudopotential method, an investigation of the electronic and optical properties for spherical GaSb NCs is presented, under the strong effects of quantum confinement. With not many studies on colloidal GaSb QDs, we were the first to provide an extensive analysis of the electronic structure, the Brillouin zone decomposition in reciprocal space and the charge density visualization in real space, as well as the identification of the corresponding optical properties for a wide range of QD sizes. Starting from the single-particle stage, the excitonic structure was then calculated. The passivation parameters were also optimized, to properly confine the charge density in the inner part of the NCs. GaSb is an indirect bandgap material with a large exciton Bohr radius and high hole mobility in the bulk and an important semiconductor material for technological applications. Here we present a theoretical investigation into the evolution of some of its most fundamental characteristics at the nanoscale. GaSb emerges as a widely tunable, potentially disruptive new colloidal material with huge potential for application in a wide range of fields.

3.1 Why GaSb: Where it is used, the colloidal form and the contribution of this research

In the past three decades there has been growing interest in GaSb as both substrate and active device material, owing to its peculiar structural, electronic and thermal properties [117]. GaSb-based structures have been proposed for a wide range of applications from high-speed optoelectronics [118, 119, 120, 121, 122, 123, 124] to high-efficiency solar energy conversion [125, 126] from gas sensing and environmental monitoring [117], to biomedical imaging and health care [127].

Epitaxial structures of reduced dimensionality, such as GaSb/AlGaSb quantum wells, are characterized by optical transitions in the wavelength region of technological importance for optical communication systems. They have found application in infrared optics as lasers, photodetectors[128, 129] and gas sensors [130], whereas GaSb nanowires, owing to the high hole mobility in GaSb, are being exploited in III-V p-channel metal-oxide-semiconductor field-effect transistors (MOSFETs) [131, 132]. GaSb/GaAs quantum dots (QDs), thanks to the quasi-type II band alignment at the heterointerface which confines the hole to the QD and leaves the electron in the matrix loosely bound by the Coulomb interaction with the hole, are ideally suited for a variety of fast, low power electronic devices and infrared light sources, [133, 134] as well as for light-emitting devices in the spectral range 1-1.5 μm, with applications in biomedical imaging in ophthalmology, neurology, and endoscopy [135]. GaSb 0D systems are also attractive materials for quantum dot infrared photodetectors (QDIPs) and quantum dot field-effect transistors (QD-FET), with possible applications in quantum communications and night vision. Another interesting application for GaSb/GaAs QDs is in charge-based memories [136, 137, 138, 139]. In a QD-memory (QDM), the charge is captured (and stored) in a potential well, which may be created by either the valence or the conduction band offset between dot and matrix material. The peculiar band alignment in GaSb/GaAs QDs is such that the difference in bandgap between the two materials is taken up entirely by the valence band, yielding confinement energies for the hole of the order of 600 meV [138]. The latter is directly linked to the maximum charge-storage time t_s achievable in the system, which has been shown to increase by one order of magnitude for each

50 meV of additional well depth (confinement energy)[138]. Considering that hole confinement of 600 meV was estimated to yield a room-temperature charge-storage time of the order of 0.2 ms [138], and that the target charge-storage time for a non-volatile memory is more than a decade, confinements over 1.1 eV will be needed to achieve it. Whilst such a depth for the hole potential well is difficult (if not impossible) to achieve in an *epitaxial* dot, this is the order of magnitude of charge confinement commonly exhibited by *colloidal* quantum dots (CQDs) [140].

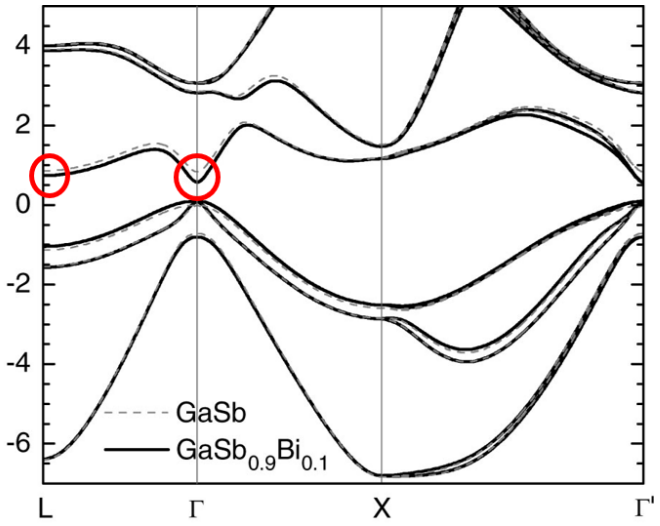

Figure 3.1: Bulk band structure for GaSb. The red circles indicate the L high-symmetry point (left) and the Γ high-symmetry point (right) of the bulk CBM, with separation in energy of 80 meV.

Here a theoretical characterization study on precisely these nanostructures is presented, which, based on the properties exhibited by their epitaxial counterparts, are expected to be promising candidates for a variety of device applications. We consider GaSb nanocrystals (NCs) with radii ranging from 11 to 45 Å, containing from 175 to over 13000 atoms. Given the large bulk Bohr radius of GaSb (20.46 nm) and its peculiar band structure, exhibiting closely spaced minima in the conduction band (CB) where the minimum at Γ and the slightly higher minima at the L-points are only about 80 meV apart (see Fig. 3.1), whereas the ratio of their respective effective masses is larger than 2 [141], it is expected that confinement should induce a Γ-to-L transition in the character of the conduction

band minimum, similarly to what was predicted to occur in GaAs [142], where the Γ-L and Γ-X separations are much larger (300 meV and 460 meV, respectively), and the bulk Bohr radius is nearly one-half (11.6 nm) than in GaSb. The valence band of GaSb, instead, has the structure common to all zincblende semiconductors, hence its Γ character is not expected to change with confinement. As a consequence, a confinement-induced direct-to-indirect bandgap transition is expected in this material, which should lead to long exciton storage times in GaSb NQDs of suitably small sizes. This, coupled with the high hole mobility in the bulk, could make GaSb nanocrystals ideal building blocks for a wide range of optoelectronic applications.

Even though GaSb is a promising, environmentally friendly nanomaterial, it has been left on the sidelines as it involves a very complex synthesis. As a result, this nanomaterial has not been synthesized yet in colloidal form. Additionally, there is no experimental evidence that such NCs are chemically and optically stable nor whether they are oxidized easily or not. On the other hand, their currently used toxic counterparts are well-studied materials that satisfy these requirements. Having reached a stage in technological development where the commercialization of devices is limited due to the toxicity of the currently used materials, there is a growing need for non-toxic alternatives, capable of replacing the toxic ones. In this research we show that GaSb NCs could be promising candidates for many technological applications, hoping to motivate experimental groups to achieve the synthesis of stable colloidal GaSb NCs.

3.2 Results

3.2.1 Electronic structure

Although bulk GaSb emits in the infrared [143], due to its large exciton Bohr radius NCs made of this material exhibit strong confinement even for large sizes and their photoluminescence (PL) can therefore be tuned nearly all the way up to the blue. The calculated position of the band edges (relative to vacuum) as a function of size is presented in 3.2, showing clearly that well depths of over 1.1 eV are easily achievable in these systems.

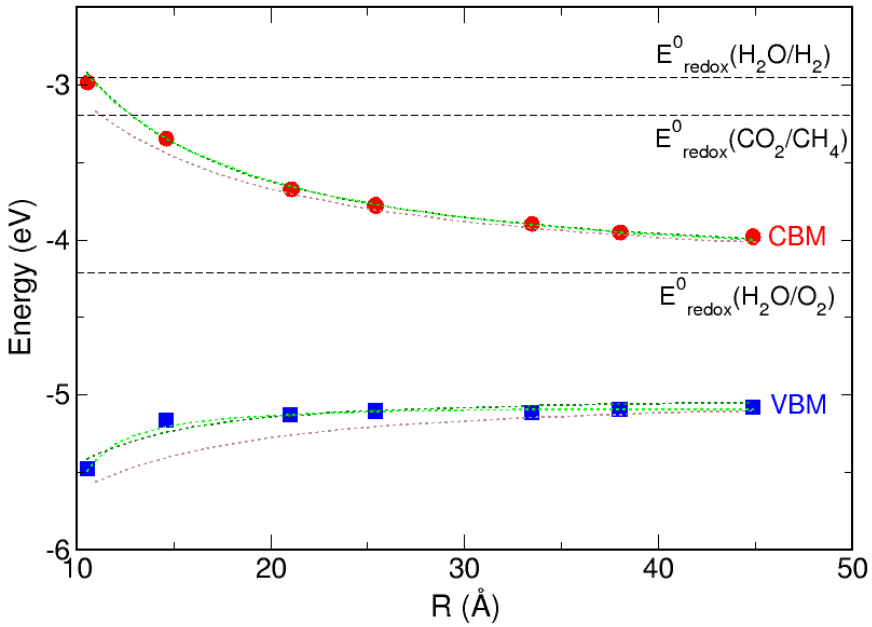

Figure 3.2: Valence (blue squares) and conduction (red circles) band edge energies, calculated with respect to vacuum, as a function of NC size. The dotted lines are fits to Eq. (3.2) (light green) and Eq. (3.1) (dark green). The brown dotted lines are obtained from Eq. (3.2) using the parameters provided by Allan et al. [144] for GaSb. The dashed lines mark the position of the redox potentials for the reduction of H_2O to H_2 (top line), the reduction of CO_2 to CH_4 (middle line), and the oxidation of H_2O to O_2 (bottom line), at pH=7. Their position relative to vacuum was obtained by shifting the values reported in Ref.[145] (Figure 2) using as a reference level our calculated position of the VBM of bulk CdSe (-5.310 eV, also confirmed experimentally [140]).

Following Williamson and Zunger [146] we fitted our data according to:

$$\begin{aligned} E_{vbm}^{dot} &= E_{vbm}^{bulk} + \frac{a}{R^{n_v}}, \\ E_{cbm}^{dot} &= E_{cbm}^{bulk} + \frac{b}{R^{n_c}} \end{aligned} \tag{3.1}$$

where $E_{vbm/cbm}^{dot}$ refer to the energy positions of the band edges in the dot, $E_{vbm}^{bulk} = -5.022$ eV, $E_{cbm}^{bulk} = -4.209$ eV, R is the NC radius, and a, b, n_v and n_c are the fitting parameters. We found $n_c = 1.19$, similar to the pseudopotential value found for InAs NCs ($n_c = 0.95$) [146], and $n_v = 1.96$, close to the effective mass (EMA) prediction ($n_v = 2$), although the fit for the size dependence of our VBM

energies is not as good as that for the CBM (our fitted values for a and b are -43.21 and 20.34 respectively). Allan *et al.* [144] used a different parametrisation to fit the band edges of NCs made of different III-V materials calculated with the atomistic tight-binding approach:

$$\begin{aligned} E_{vbm}^{dot} &= E_{vbm}^{bulk} - \frac{1}{a_v D^2 + b_v D + c_v}, \\ E_{cbm}^{dot} &= E_{cbm}^{bulk} + \frac{1}{a_c D^2 + b_c D + c_c} \end{aligned} \tag{3.2}$$

where $D = 2R$ (in nm), and a_i, b_i and c_i $(i = v, c)$ are the fitting parameters.

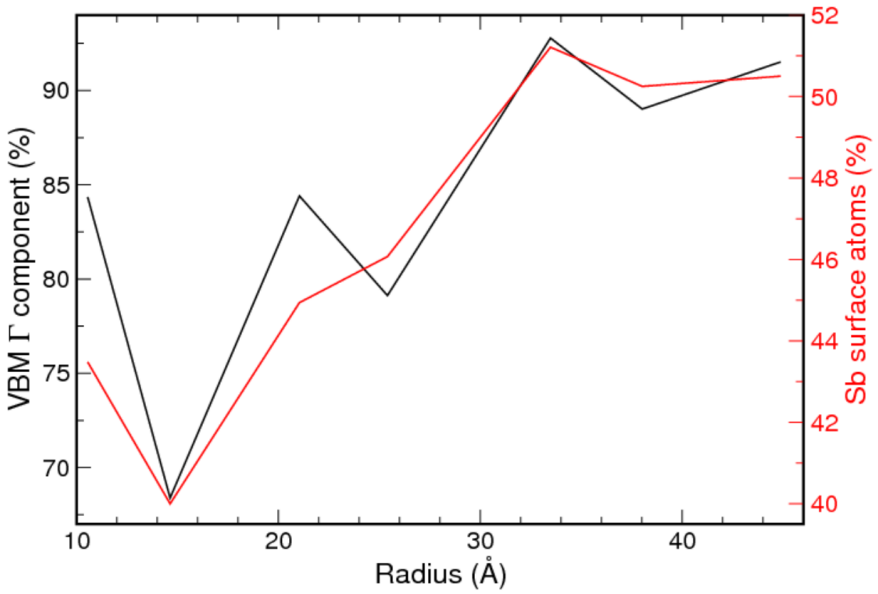

Figure 3.3: Γ component of the VBM (black line, left-hand y axis) and percentage of Sb surface atoms - defined as $N(Sb)_{surf}/\left[N(Sb)_{surf} + N(Ga)_{surf}\right]$ - (red line, right-hand y axis) as a function of NC size.

Our fitted cbm values ($a_c = 0.02183$, $b_c = 0.33855$ and $c_c = 0.00604$) are close to their fitted cbm parameters ($a_c = 0.02650$, $b_c = 0.33745$ and $c_c = 0.09540$) for the case of GaSb, whereas our vbm parameters ($a_v = -0.51288$, $b_v = 7.28085$ and $c_v = -10.8934$) are very different (even in sign) from theirs ($a_v = 0.08017$, $b_v = 0.63268$ and $c_v = 0.07146$). Unfortunately, they do not present the detailed size-dependent band edges curves for this material but only their parametrisation

(brown dotted lines in Fig. 3.2). We can, therefore, only comment on the quality of agreement with the latter. As was the case with Williamson and Zunger's parametrisation, the fit of our calculated CBM is much better than that of the VBM.

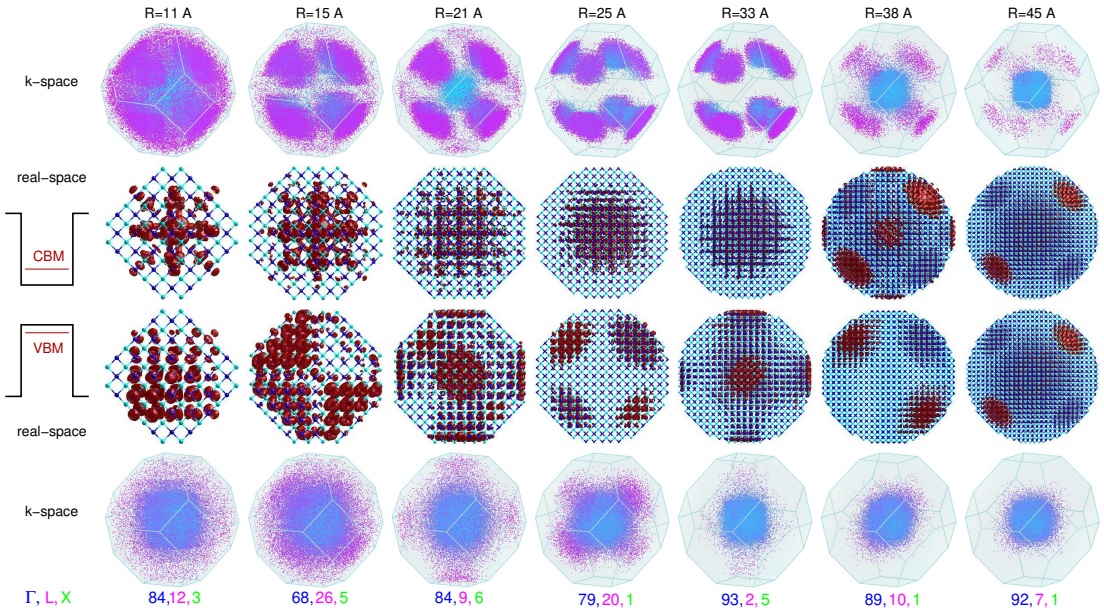

Figure 3.4: Calculated 3D charge densities in real space (2nd and 3rd rows) and k-space composition visualized in a 3D Brillouin zone (top and bottom rows: points close to the L points are displayed in magenta, points close to Γ are colored in blue) for the valence (3rd and 4th rows) and conduction (1st and 2nd rows) band edges, for all sizes considered. The components indicating the percentage of the contribution originating from each one of the three high symmetry points Γ (blue), L (magenta), and X (green) in the Brillouin zone for the VBM are reported in the last row.

Part of the reason for this poor-fitting could be due to the different stoichiometry (Sb-rich both in total and also, more importantly, on the surface, as opposed to the Ga-rich composition, both in total and on the surface, which is prevalent among all other sizes) of the NCs with $R \geq 33$ Å whose VBM energies are slightly lower than expected according to Eq. (3.1). We find this to be a general trend in NCs, their VBM being determined by the anion: The VBM in NCs with anion-rich surfaces is always found at lower energy than that in NCs with cation-rich surfaces. We also find (Fig. 3.3) that a Sb-rich surface correlates with

a large Γ component of the VBM and vice versa: indeed the $R = 15$ Å NC has the largest percentage of Ga surface atoms, the lowest VBM Γ component and its VBM is much higher than predicted by Eq. (3.1). Based on these considerations, we can speculate that the poor agreement obtained with the curves by Allan et al. [144] (brown dotted lines in Fig. 3.2) could originate from the fact that the structures they studied might have been cation-centered, hence exhibited Sb-rich surfaces for small sizes, leading to lower values for the VBM than our Ga-rich NCs.

It is worth mentioning that the level of accuracy required to capture such detail is not achievable with continuum methods like the popular **k·p** - which cannot distinguish between the properties of Ga-rich and Sb-rich CQDs - but is only available to atomistic methods. Most importantly, however, the **k·p** method misses the contributions from both X and L high symmetry points (at least up to the 8-band version), which, as shown in Fig. 3.4, Fig. 3.5, and Fig. 3.6, are vital to understand the properties of GaSb at the nanoscale.

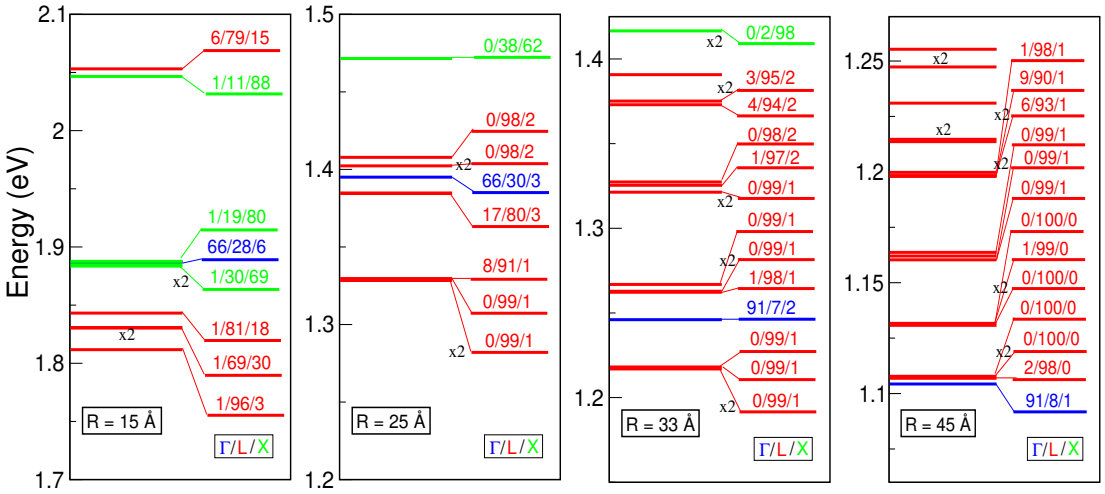

Figure 3.5: CB electronic structure for selected GaSb NC sizes ($R = 15$, 25, 33, 45 Å). Each panel displays energy levels relative to the top of the valence band (left-hand side) and k-vector decomposition (right-hand side) for a different dot size. The different states are coloured according to their main character (Γ, blue; L, red; and X, green) resulting from such a decomposition. "×N" indicates the state degeneracy.

The most interesting feature of the electronic structure of these NCs is the composition of the conduction band states (Fig. 3.5), and more specifically of the CBM (Fig. 3.4 and Fig. 3.6), in terms of their k-vector components. We find that already NCs with radii as large as 36 Å experience sufficient confinement to exhibit a Γ to L transition in the CBM character, whereas the VBM has prevalent Γ character for all sizes (Fig. 3.4). As a consequence a direct-to-indirect bandgap transition takes place at around $R = 36$ Å. We investigated the effect of 6 ligand sets with different electronegativity (see [147]) and found that such transition takes place at similar or larger sizes in all cases except for very electronegative ligands (type A in Ref.[147]), where such transition is suppressed, even for very small NCs (down to $R = 8$ Å). Fig. 3.5 shows that with decreasing size (increasing confinement) also, the X-derived states decrease in energy sufficiently to appear among the lowermost 10 conduction states, whereas, at the same time, the energy of the Γ-derived ones increases steadily.

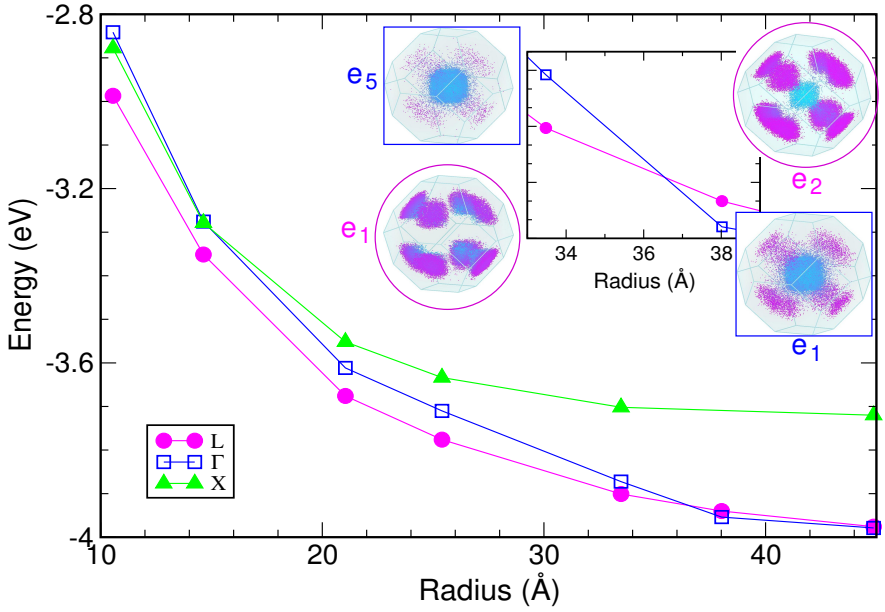

Figure 3.6: Lowest confined conduction band states derived from Γ (blue squares and line), L (magenta circles and line), and X (green triangles and line). The inset shows a detail of the crossing between Γ and L and the calculated k-vector decomposition of the four states represented.

3.2.2 Optical properties

Owing to the strong confinement experienced by these nanostructures, the emission of GaSb CQDs can be tuned from the IR, nearly all the way to the blue (for $R < 10$ Å), as can be seen from Fig. 3.7, where we plot the calculated positions of both PL and absorption edges as a function of the nanocrystal radius. We fitted the band edge absorption according to

$$E_g^{dot} = E_g^{bulk} + \frac{A}{D^n} \tag{3.3}$$

and found $A = 38.02$ and $n = 1.07$ - red dashed line in Fig. 3.7 - with a size dependence in stark contrast with the prediction ($n = 2$) of simple effective mass approaches [148], but nearly identical to that found for InP ($n = 1.09$) [149, 150], and similar to that found for InAs ($n = 0.9$) [146], and Si ($n = 1.18$) [151].

Large separations between emission and band edge absorption (referred to as "global Stokes shifts") suppress photoluminescence self-absorption and are therefore beneficial to all applications exploiting light emitted from the dot (LEDs, biological imaging[152], lasers, solar energy harvesting[153, 154], etc.). Inset (b) of Fig. 3.7 shows that the Stokes shifts achievable in these NCs range from 0 up to 160 meV, depending on the size. These shifts are also accompanied by long radiative times (inset (a) of Fig. 3.7) on the microsecond scale (except for the smallest NC considered), due to the indirect nature of the bandgap transition, discussed above.

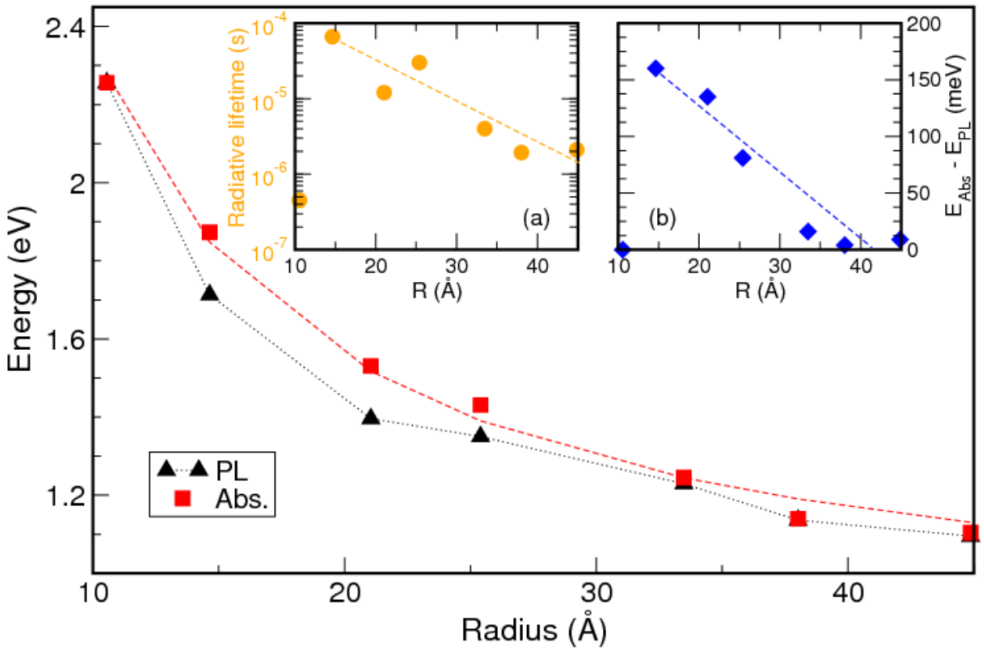

Figure 3.7: Optical properties as a function of size. Main panel: energy dependence on NC radius (R) of the band edge absorption (Abs., red squares - the red dashed line is a fit to the theoretical data according to Eq. (3.3)), and emission (PL, black triangles - the dotted line is a guide to the eye). Left inset: room temperature radiative lifetime (orange symbols) as a function of radius. Right inset: Stokes shift (energy difference between red and black symbols in the main panel) vs radius. The dashed lines are a guide to the eye.

Both radiative lifetimes and Stokes' shifts show a decreasing trend with increasing NC radius (dashed lines in insets (a) and (b) of Fig. 3.7), except for the smallest structure considered which exhibits the fastest recombination time which is also accompanied by the smallest Stokes' shift calculated. Similar behavior to our Stokes' shift was also found for the dark-bright energy splitting in GaAs NCs by Luo *et al.* [155]. The decrease of the radiative recombination times with increasing size is instead consistent with experiment in CdS [156] and CdSe [157, 158] nanocrystals, and in contrast with the trend observed in InAs [159] and CdTe dots [158].

3.2.3 Excitonic fine structure

In order to better understand the nature of the different transitions, we calculated the symmetry of the single-particle states involved and the resulting total symmetry of the excitons contributing to the optical transitions [160].

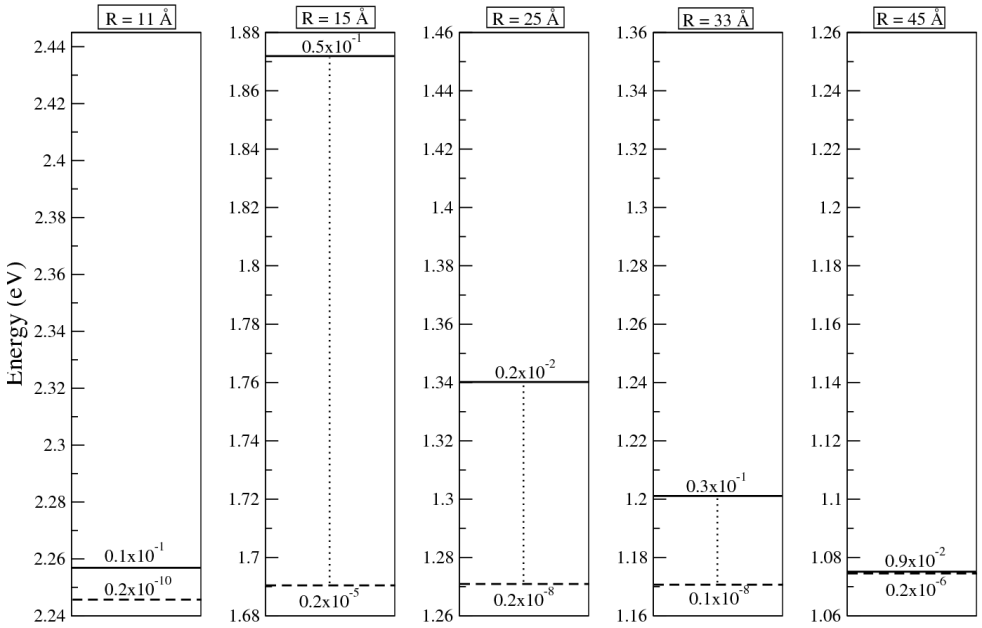

Figure 3.8: Ground (dark, dashed lines) and first optically allowed (bright, solid lines) exciton state for different nanocrystal sizes. The calculated value of the CI dipole matrix element (Eq. 2, main text) for the transition $|1e;1h\rangle \rightarrow |0e;0h\rangle$ is also reported for each state. For each size, we define as 'dark' all excitons with a transition dipole matrix element less than 100 times smaller than that calculated for the strongest optical transition for that size. In the case of $R = 11$ Å the ground exciton is dark and 2-fold degenerate, followed by another 3-fold degenerate dark state 0.32 meV above it and then by the 3-fold degenerate bright exciton. For $R = 45$ Å, there are no other states between the dark, 3-fold degenerate ground state and the 3-fold degenerate bright exciton. In both cases, this results in fast radiative recombination times and small Stokes' shifts. The presence of intermediate states between dark and lowermost bright exciton, found for all other sizes, is marked by vertical dotted lines.

We find the CBM envelope function symmetry to be prevalently s-like for all sizes except for radii 25 and 33.5 Å, when it is prevalently p-like (we find that

the symmetry of a state is never pure s- or pure p-like, but it always displays some degree of mixing; hence when, in what follows, we refer to l-like symmetry we always intend *prevalent* l-like symmetry), whereas the symmetry of the VBM is s-like only for the two smallest sizes ($R = 11$ and 15 Å) and p-like for all the others. As a consequence, in the smallest NC the exciton ground state is split into a lower fivefold-degenerate forbidden $\mathbb{E} + \mathbb{T}_1$ multiplet and a higher allowed threefold-degenerate $\mathbb{T}_2$, separated by only 10 meV, as illustrated in Fig. 3.8.

As the width of our optical peaks is 5 times larger than this separation, the resulting Stokes shift is 0. Furthermore, this size's CBM has the largest Γ component of all dots (12.4%), leading to the fastest radiative time of them all. The CBM of the 15 Å NC has nearly 0 Γ character (see Fig. 3.5), resulting in the longest lifetime calculated here. The lifetimes then decrease with increasing size until, for $R = 38$ Å, the band edge transition becomes direct. It is therefore clear that in the case of GaSb, unlike for other III-V materials, the allowed (bright) and forbidden (dark) character of the different excitonic states (see Fig. 3.8), hence the behavior of their radiative lifetimes, is the result of a complex interplay between k-space composition and symmetry of the single-particle states that contribute to each exciton state.

The Stokes shifts follow the trend of the lifetimes, as a result of the progressive shift to lower energies of the fully allowed optical transitions, due to the increase in the density of single-particle states with increasing size.

3.3 Applications of GaSb spherical NCs

The combination of visible light absorption and long recombination lifetimes ($> 0.5 \times 10^{-6}$ s) is ideal for many solar energy conversion applications. Additionally, the large Stoke shifts suppress self-absorption which could be beneficial for applications that take advantage of emitted light such as LEDs, biological imaging, lasers, solar energy harvesting, etc.

Here we will focus in particular on photocatalytic CO_2 reduction with water. This reaction involves three main steps: (1) photogeneration of an electron-hole pair; (2) electron and hole separation and migration to the nanocrystal surface (where a co-catalyst may be present); (3) reduction of CO_2 by the electron and

oxidation of H_2O by the hole. The reduction and oxidation reactions considered for this specific application are presented in detail in Table 3.1.

Table 3.1: Possible reactions involved in photocatalytic conversion of CO_2 with H_2O [161]

Reaction								
CO_2	+	$2\ H^+$	+	$2e^-$	$\longrightarrow$	$HCOOH$		
CO_2	+	$2\ H^+$	+	$2e^-$	$\longrightarrow$	CO	+	H_2O
CO_2	+	$4\ H^+$	+	$4e^-$	$\longrightarrow$	$HCHO$	+	H_2O
CO_2	+	$6\ H^+$	+	$6e^-$	$\longrightarrow$	CH_3OH	+	H_2O
CO_2	+	$8\ H^+$	+	$8e^-$	$\longrightarrow$	CH_4	+	$2\ H_2O$
$2H^+$	+	$2e^-$			$\longrightarrow$	H_2		
H_2O	+	$2h^+$			$\longrightarrow$	$1/2\ O_2$	+	$2\ H^+$

Apart from the general improvements in efficiency due to nanostructuring (such as shortened carrier collection pathways, improved light distribution, quantum-size-confinement-induced increase in interfacial charge transfer rates, pH-tunability of interfacial charge transfer and surface-area-enhanced charge transfer)[162], the use of GaSb dots as catalysts would lead to specific major advantages in each of the above steps: (1) unlike most of the semiconductor materials used for this reaction (mainly TiO_2[145], but also WO_3[163] and CeO_2[164]), whose bulk band gap is large (2.6-3.6 eV) the absorption of GaSb NCs can be tuned to span the whole visible spectrum, optimising light harvesting efficiency; (2) their radiative recombination lifetimes ($> 0.5 \times 10^{-6}$ s) are longer than (or comparable to) the typical redox reaction times ($> 10^{-8}$ s) [145] - which are usually too slow to compete with the radiative lifetimes exhibited by common semiconductor nanocrystals ($\sim 10^{-9}$ s) - hence the charge carriers in GaSb NCs would have sufficient time to reach the surface and react with CO_2 and H_2O before recombining (The efficiency of the photocatalytic reaction depends critically on the competition between these two processes, as well as on the light absorption efficiency). A recent study [147] suggests that a further over-one-order-of-magnitude increase in radiative times

could be obtained by exchanging the capping group with a more electropositive ligand (throughout In this work, we have used passivants with intermediate electronegativity - corresponding to set D in Ref.[147]); (3) their bandstructure - an important aspect of the reaction is the position of the catalyst's band edges relative to the redox potential for CO_2 reduction (RP1) and H_2O oxidation to O_2 (RP2): in order for a semiconductor to be able to catalyze the reduction of CO_2 with H_2O (i) its CBM should be higher (more negative) than RP1 while (ii) the VBM should be lower (more positive) than RP2. Although all sizes considered here satisfy (ii) (see bottom dashed line in Fig. 3.2), we estimate that only small GaSb nanocrystals ($R \lesssim 13$ Å) would satisfy (i) in the case of the formation of CH_4 (see middle dashed line in Fig. 3.2), which, having the least negative redox potential (-0.24 V at pH=7) [145], is the thermodynamically more favourable reduction process. In addition to these properties, the selectivity towards CO_2 reduction is a determining factor, in the presence of H_2O, as the reduction of H_2O to H_2 strongly competes with the reduction of CO_2. The former, being a two-electron reaction compared to the eight electrons needed for the formation of CH_4, is, in fact, kinetically more favourable. We find that the CBM of GaSb NCs with $R > 10$ Å, is lower than the redox potential for the reduction of H_2O to H_2 (see top dashed line in Fig. 3.2). Water reduction is therefore expected to be suppressed in GaSb NCs simply due to their specific band structure, as shown in Fig. 3.9. This represents a huge advantage compared to other semiconductor nanostructures, where some degree of surface manipulation is required to enhance the photocatalytic reduction of CO_2 in the presence of H_2O. As a consequence, unlike with TiO_2 [165] or other semiconductors, in the case of GaSb, the use of both solid-liquid or solid-vapour reaction modes should be possible and should yield similar rates of CH_4 formation, adding further flexibility to the design of the reactor.

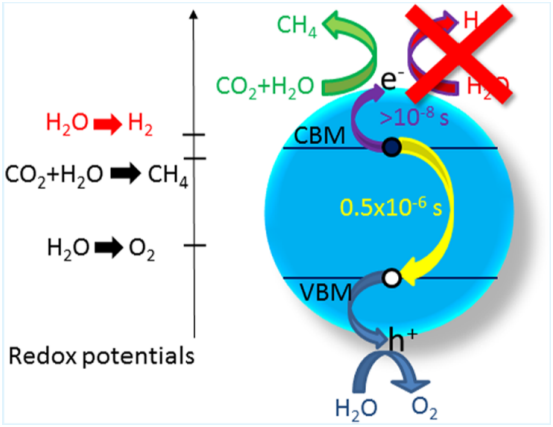

Figure 3.9: Photocatalytic reduction of CO_2 with water. Water reduction can be suppressed by using NCs ($R > 10$ Å) with CBM lying between the CO_2 and the H_2O redox potentials.

A further increase in the internal quantum efficiency of CO_2 reduction could be achieved with the introduction of additional smaller GaSb NCs, which would act as 'sensitiser' NCs (i.e., absorb light at a slightly higher energy) and funnel the excitons, through a Förster energy transfer mechanism, to 'catalyst' NCs, which, in turn, deliver the electrons to their surface for the reduction reaction. A sensitiser-to-catalyst ratio of 8:1 would provide all 8 electrons needed for the reduction of CO_2 to CH_4. A similar strategy recently led [166] to an increase of over one order of magnitude of the internal quantum efficiency of the photocatalytic reduction of H^+ to H_2 using CdSe-based NCs. The latter result proves the feasibility for our catalyst NC to accumulate multiple redox equivalents at a single catalytic site. This is made possible by the neutrality of the funnelled exciton, which can be transferred from sensitiser NC to catalyst NC without any accompanying nuclear reorganisation of either chromophores or solvent[166]. The above discussion is clearly oversimplified, as it neglects some aspects of surface modification that may be needed to achieve efficient adsorption, activation, and transformation of CO_2. Nevertheless, it provides a list of desirable properties that make GaSb NCs appealing candidates for photocatalytic applications.

3.4 Conclusions

One of the main achievements of this research was the publication of our results regarding the characterization of colloidal GaSb NCs and their possible applications[71]. GaSb constitutes a new, environmentally friendly material that, due to its complex synthesis procedures, has not been synthesized before in colloidal form. We have presented a comprehensive theoretical characterization of colloidal GaSb nanocrystals with radii ranging from 11 Å, to 45 Å, containing from 175 to over 13000 atoms. We have investigated the size dependence of conduction and valence band edge energies, k-space composition and symmetry of their respective wave functions, the evolution of Γ-, L- and X-derived states in the conduction band, absorption and emission spectra, radiative lifetimes, and Stokes' shifts. We found GaSb nanocrystals to have a size-dependent emission tunable throughout the visible spectrum, large Stokes's shifts, and, due to a confinement-induced direct-to-indirect bandgap transition occurring at very large sizes, long radiative lifetimes ($>0.5\times\ 10^{-6}$). Such properties make them promising building blocks for a wide range of applications, including solar energy conversion, memory storage and, in particular, photocatalytic CO_2 reduction, where GaSb NCs may represent a viable and more versatile alternative to the semiconductor nanostructures commonly used as catalysts. We believe that the properties highlighted in this study will stimulate renewed efforts to synthesize this new colloidal nanomaterial.

Chapter 4

Spherical InP NCs

In the present chapter, we discuss our investigation and findings on the electronic and optical properties and the effect of surface stoichiometry in spherical InP NCs. The procedure of optimizing the surface passivation parameters for our calculations and our methodology is also presented. In general, InP has been studied for over 20 years now, however, the explanation of the origins of the broad emission and low quantum yield remain unsatisfactory. Like in the case of CdS, this is commonly attributed to their poor surface quality and difficult passivation, which give rise to trap states and negatively affect emission. Hence the strategies adopted to improve their quantum yield have focused on the growth of shells, to improve passivation and get rid of the surface states. Here, after optimizing the passivation set so far known and employing the state-of-the-art atomistic semiempirical pseudopotential modelling to isolate the effect of surface stoichiometry from features due to the presence of surface trap states, we show that, even with an atomistically perfect surface and ideal passivation, InP nanostructures may still exhibit very long radiative lifetimes, of the order of tens of microseconds, broad, weak emission, and large Stokes' shifts. Furthermore, we find that all these quantities can be varied by orders of magnitude, by simply manipulating the surface composition, and, in particular, the number of surface P atoms. As a consequence, it should be possible to substantially increase the quantum yield in these nanostructures by controlling their surface stoichiometry.

4.1 Why InP and the contribution of this research

Semiconductor Colloidal Quantum Dots (CQDs) have drawn great attention due to their unique size-dependent electronic and optical properties which make these nanocrystals (NCs) ideally suited for a wide range of applications [167, 168] such as lighting, photovoltaics, catalysis, optoelectronics, and bio-imaging. In particular InP has emerged as a promising environmentally-friendly material [169, 170] that could replace cadmium-based semiconductors, such as CdSe, CdTe, and CdS, whose toxicity will limit the commercialisation in many countries[171]. In addition to that, recent studies showed that InP NCs could yield enhanced surface stability[172], thermal stability[173], and optical stability[174], matching the stability of toxic nanomaterials mentioned above. InP is a direct bandgap semiconductor with a larger dielectric constant, lower effective electron and hole mass, weaker phonon coupling, and lower toxicity than chalcogenide-based semiconductors. It has a similar bandgap to CdSe, with which also shares a size-tunable emission in the visible region of the spectrum[170].

Although the electronic and optical properties of nanoscale InP were first investigated experimentally by Micic *et al.* [175], and theoretically by Fu and Zunger [97], over 20 years ago, the interest in this material is still high, with applications of InP NCs ranging from optoelectronics[176] to photovoltaics[177], and from bio-imaging[178] to memory storage [179] and lighting[180]. Nevertheless, the measured photoluminescence (PL) quantum yield (QY) is still low especially in small (< 3 nm) QDs [181, 182, 180, 183, 184], and the presence of deep-trap emission is still reported even in core/shell systems [185, 186, 187, 188]. Only very recently Jang's group [188, 189] and Peng's group [176] were able to achieve nearly 100% PL QY in InP/ZnSe/ZnS QDLEDs. The record QY was attributed to an improved surface passivation achieved by means of the multilayer shell structure, where the ZnSe interlayer served as strain reliever between InP and ZnS, resulting in the elimination of most surface defects. In general, however, InP-based QLEDs exhibit low efficiency, due to the low QY which results from decreased radiative recombination rates. These are generally ascribed to the presence of surface traps, due to imperfect passivation [169, 190, 191, 178]. It is however still unclear what kind of traps (electron or hole) are present on the

surface [192, 193, 190] and what are the origins of the broad, red-shifted emission (Stokes' shift) observed in many samples.

In this chapter, we present a detailed theoretical characterization of InP CQDs, focusing in particular on the effects of surface stoichiometry on the optical properties and excited state relaxation. We show that, even in the presence of a full coverage of ideal passivants, i.e., in the absence of surface traps, the radiative recombination times in InP NCs can be as long as tens of microseconds, and depend on the surface composition, i.e., on whether there is a prevalence of In or P atoms on the surface. Strikingly, we find that the addition of only a few P atoms on an otherwise In-rich surface can reduce (i) the radiative lifetime (by about two orders of magnitude), (ii) the Stokes' shift and (iii) the PL linewidth, in small NCs, where the surface atoms represent a substantial fraction of the total number of atoms. In larger structures, the effect of surface stoichiometry becomes less important and is balanced by the increase of the volume.

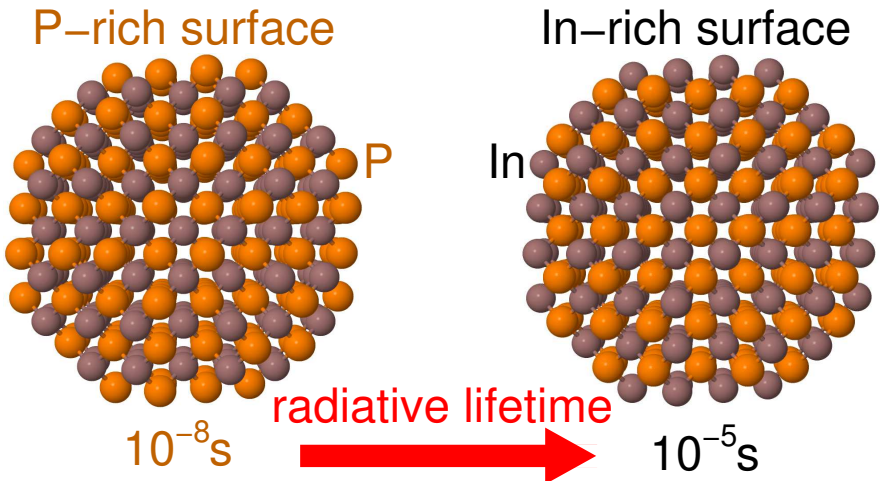

Figure 4.1: Tuning the radiative recombination lifetimes by engineering the surface of InP NCs.

4.2 Surface Passivation Optimization

One of the main challenges with InP NCs was their surface passivation. We had to make sure that our NCs were properly passivated, meaning that we wanted

Passivation	cation						anion					
	1 dangling bond			2 dangling bonds			1 dangling bond			2 dangling bonds		
	a	b	c	a	b	c	a	b	c	a	b	c
This work	1.18	0.40	0.55	1.40	0.55	0.65	-1.20	0.40	0.25	-0.78	0.75	0.25
Fu & Zunger [97]	1.18	0.45	0.25	1.90	0.70	0.50	-0.93	0.50	0.25	-0.78	0.75	0.25
Graf *et al.*[95]	1.68	0.80	0.35	1.68	0.64	0.25	-1.68	0.33	0.25	-1.05	0.80	0.25

Table 4.1: Passivation parameters used to passivate surface In and P atoms in this work compared with the parameters used by Fu and Zunger [97] and Graf *et al.* [95].

to model trap-free systems, with charge densities localized in the core region of the NCs. Our structures were passivated by using Gaussian potentials and by following the procedure described in Chapter 2. A visual representation for a QD with $R = 12$ Å is illustrated in Fig. 4.2 before and after the passivation. As mentioned in the previous chapters, the surface ligands present in realistic colloidal systems include hexadecyl amine (HDA), acids, thiols, polymers, and enzymes.

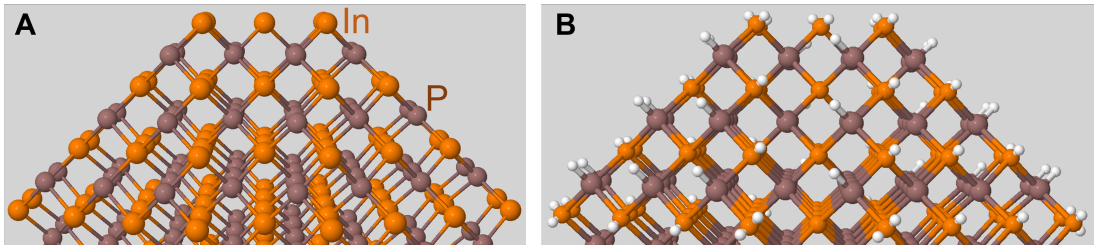

Figure 4.2: Unpassivated (left) and passivated (right) InP QD. The white spheres at the NC surface represent the Gaussian potentials used to passivate the surface of InP NCs.

Fu and Zunger [97] and Graf et al.[95] have also applied the atomistic semiempirical pseudopotential method decades ago, using different passivation sets for this material, as shown in Table 4.1. In their studies, they reported a trap-free system which did not yield good confinement when using their passivation sets. Thus, by following the procedure described by [95] we adjusted the parameters aiming to improve the confinement and push the charge densities to the core

region of the QDs. It should be underlined that surface atoms with 3 dangling bonds were removed as they are unstable for dissociation.

As shown in Fig. 4.3 and Fig. 4.4, the previously used parameters led to insufficiently confined VB for most of the sizes. The charge density visualization in real space for the CBM and VBM for all QD sizes considered here is presented in Fig. 4.3, illustrating the three passivation sets from (a) previous theoretical studies (blue and orange) and (b) this research (green).

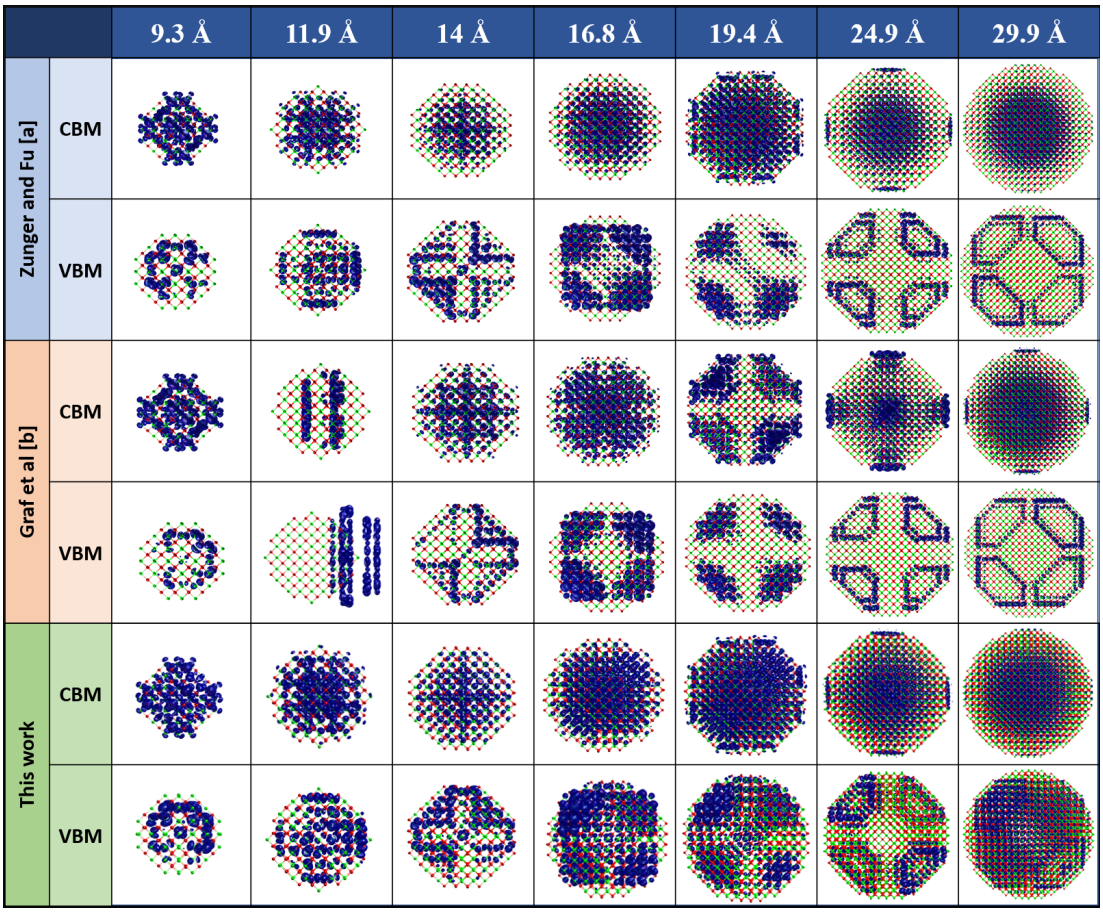

Figure 4.3: 3D charge density visualization for CBM and VBM states, when using the passivation settings derived by a: [97] and b: [95]. The exact same dots were modeled in this study, but with different surface passivation.

We find that the optimized passivation paramaters that were used in this work resulted in much higher VBM core charge density localization for all QD sizes,

compared to the other two studies. Clearly, the parameters of [97] yield a much better output compared to [95], however, the VBM energy for some of the dots exceeds the boundaries of the bulk VBM energy, which indicates the presence of states in the gap as shown in Fig. 4.4.

This work aimed to properly confine the energy of the VB states and thus achieve higher concentrations of charge density in the core region of the quantum dots. Considering that there are three parameters (a, b, and c) for each type of unpassivated atom (with one or two dangling bonds) at the surface and having the passivation set of [97] as a reference point, we started by changing each one of the parameters while keeping the rest of them constant.

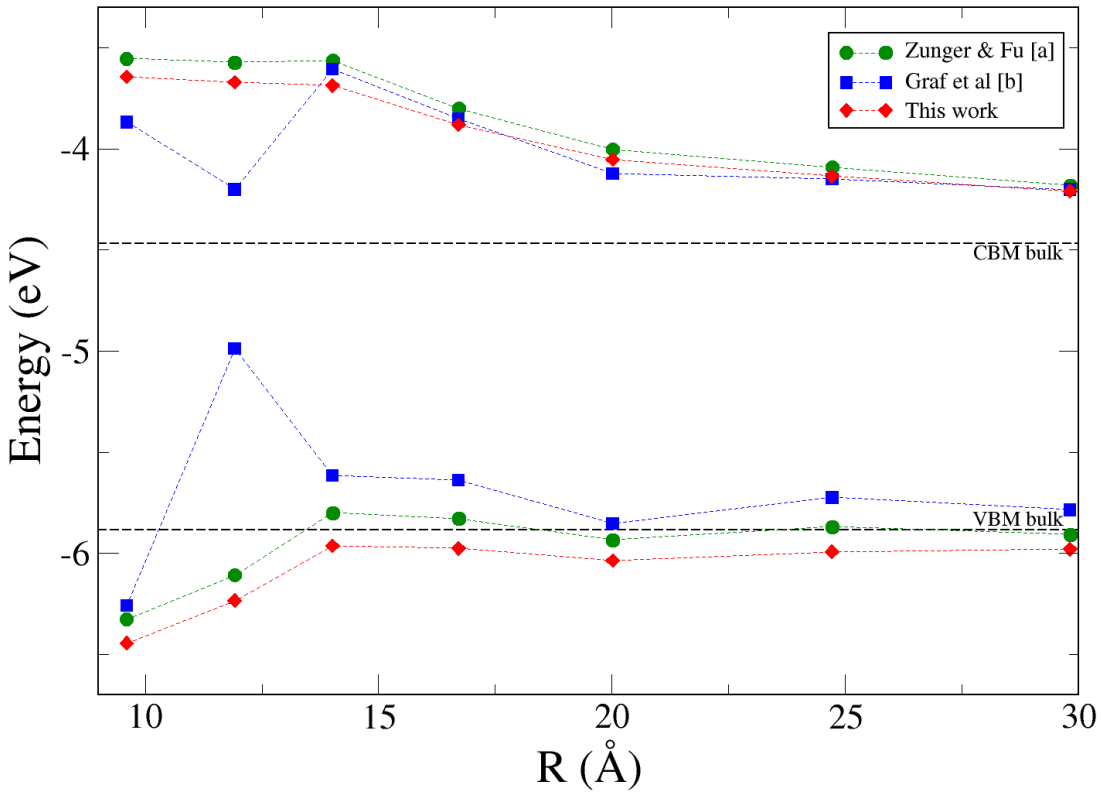

Figure 4.4: Band edges for CBM and VBM states for passivation sets a: [97] and b: [95] compared to our settings. Both a and b yield surface states as, for several NCs, the VBM states lie in the gap between the bulk values.

The new set could be classified as optimized by making sure that (i) the

resulted CBM and VBM energies were above and below the bulk CBM and VBM energies respectively (trap-free NCs) and (ii) the charge density core localization for the VBM was improved compared to the values of the reference set. The optimization procedure was implemented on two different dots with $R = 12$ Å and $R = 14$ Å. We chose smaller dots, where the effect of the surface chemistry is stronger compared to larger dots. By repeating the procedure for each type of passivant and each parameter, with more than 250 iterations, we reached a satisfactory outcome as presented in Fig. 4.4.

This is also confirmed by the three-dimensional visualization of the charge density (Fig. 4.3 and Fig. 4.4), clearly exhibiting no localisation on the surface, hence indicating the absence of surface states. The charge density distribution of both CBM and VBM within[98] the different nanostructures, was determined by integrating the square of the respective wave functions within spheres (concentric with the NC) with increasing radii up to the NC radius R.

	$R = 9.3$ Å P-rich		$R = 11.9$ Å In-rich		$R = 14$ Å In-rich		$R = 16.8$ Å In-rich		$R = 19.4$ Å P-rich		$R = 24.9$ Å In-rich		$R = 29.9$ Å P-rich	
R_{int}	CBM	VBM	CBM	VBM	CBM	VBM	CBM	VBM	CBM	VBM	CBM	VBM	CBM	VBM
This work														
90	60.3	87.8	81.4	87.3	86.1	87.1	84.9	77.4	76.8	71.1	87.7	70.8	90.2	86.7
80	39.6	58.1	67.1	61.3	71.8	51.8	67.5	36.9	60.8	41.6	74.7	25.4	77.9	67.8
Fu and Zunger [97]														
90	64.2	87.9	85.2	87.4	89	85	88.1	72.6	79.1	60.3	89.3	63.5	91.6	55.3
80	43.9	59.5	72.5	57.1	76.7	47.4	73	25.4	64	23.8	77.6	14.9	80.8	16
Graf et al.[95]														
90	62.4	89.3	94.1	25	88.7	79.6	86.8	75.3	49.7	57.7	77	59.2	88.9	46.3
80	39.3	57.1	83.4	12.6	75	38.2	68.6	24.4	26.7	17.1	62.1	10.4	76.7	0.09

Table 4.2: CBM and VBM charge densities (%) calculated, in all the CQDs investigated, as integrals of the square of the respective wave functions within spheres (concentric with the NC) with radii R_{int} 90% and 80% of the NC radius R. The surface character (whether cation- or anion-rich) is also shown for each NC. As an example, in an InP NC with radius 14 Å (with an In-rich surface) 42% of the CBM and only 7.9% of the VBM are localised within a sphere with a radius of 8.4 Å (i.e., 60% R). We, therefore, conclude that most of the VBM charge density in this dot is contained outside it, i.e., in a spherical shell with inner radius = 8.4 Å and outer radius = R. The table indicates the results for the three different passivation sets: Fu and Zunger [97], Graf et al.[95] and this work.

4.3 Electronic Structure

We consider spherical NCs with radii ranging from 10 Å to 30 Å. The calculated position of their band edges as a function of size is presented in Fig. 4.5, from which we can conclude that our nanostructures are free from (trap) states in the gap, since our calculated band edges do not cross with the bulk band edges.

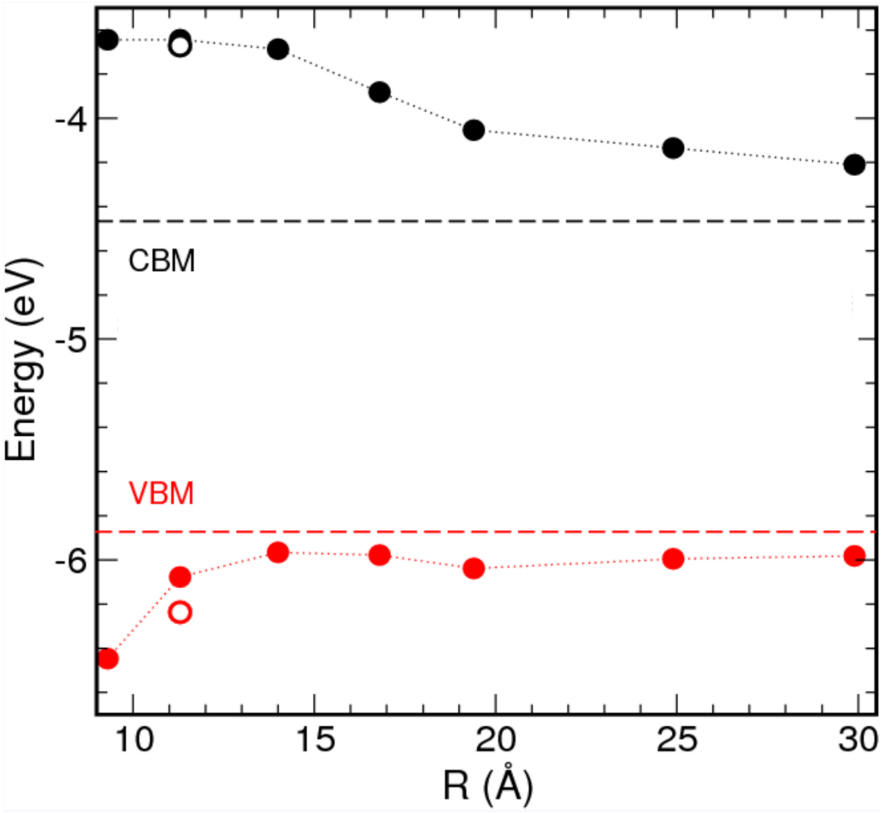

Figure 4.5: Calculated band edge energies as a function of NC size. The dashed lines represent the position of CBM (black) and VBM (red) in bulk InP. The empty circles mark the band edges' position in a NC with $R = 12$ Å, after adding 6 P atoms on the NC surface (see text).

Aiming to provide a better insight on the amount of core-localized charge densities, we performed a quantitative investigation finding much lower values for the charge density of the VBM compared to the CBM within 80% of R for all sizes except the smallest NC (see Table 4.3).

	$R = 9.3$ Å		$R = 14$ Å		$R = 16.8$ Å		$R = 19.4$ Å		$R = 24.9$ Å		$R = 29.9$ Å	
	P-rich		In-rich		In-rich		P-rich		In-rich		P-rich	
R_{int}	CBM	VBM	CBM	VBM	CBM	VBM	CBM	VBM	CBM	VBM	CBM	VBM
90	60.3	87.8	86.1	87.1	84.9	77.4	76.8	71.1	87.7	70.8	90.2	86.7
80	39.6	58.1	71.8	51.8	67.5	36.9	60.8	41.6	74.7	25.4	77.9	67.8
70	21.6	32.5	56.0	19.3	53.1	19.8	47.1	23.8	58.7	7.7	62.6	48.2
60	11.9	17.9	42.0	7.9	39.1	8.2	33.8	21.0	42.5	1.9	46.2	30.5
50	6.6	7.7	28.6	2.5	25.9	3.4	21.6	6.2	27.5	0.4	30.7	16.2

Table 4.3: CBM and VBM charge densities (%) calculated, in all the CQDs investigated, as integrals of the square of the respective wave functions within spheres (concentric with the NC) with radii R_{int} ranging from 50% to 90% of the NC radius R.

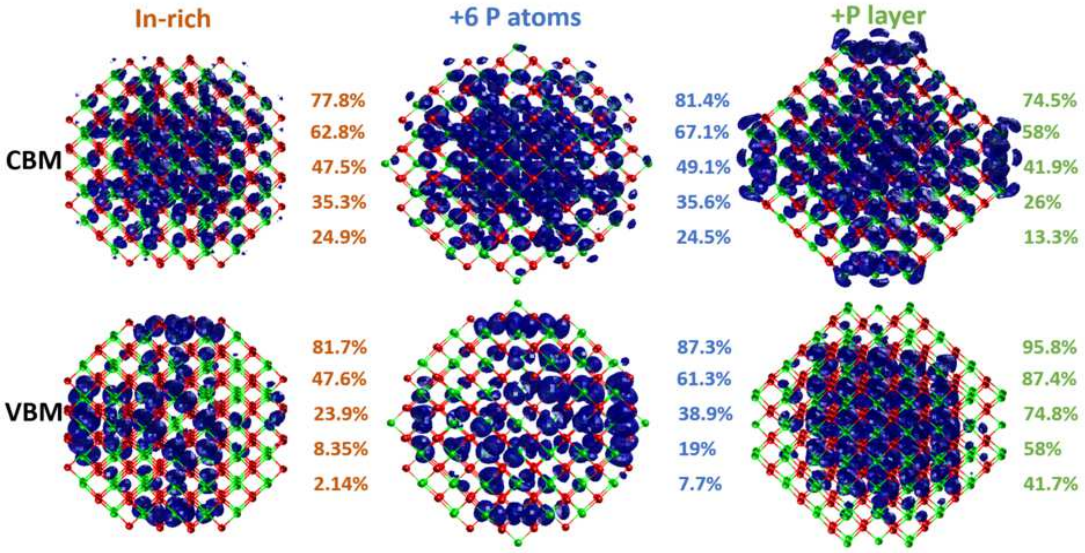

Figure 4.6: Evolution of the calculated CBM and VBM charge densities (blue) in an InP CQD with $R = 11.3$ Å with increasing P surface coverage, from an In-rich surface to a full P layer coverage (green dots represent P atoms and red dots In atoms): the numbers next to each charge density plot quantify the charge density (as a percentage of the total charge density) calculated within spheres, concentric with the NC, with radii equal to 90%, 80%, 70%, 60% and 50% of the dot radius R, similarly to the results presented in table 4.3.

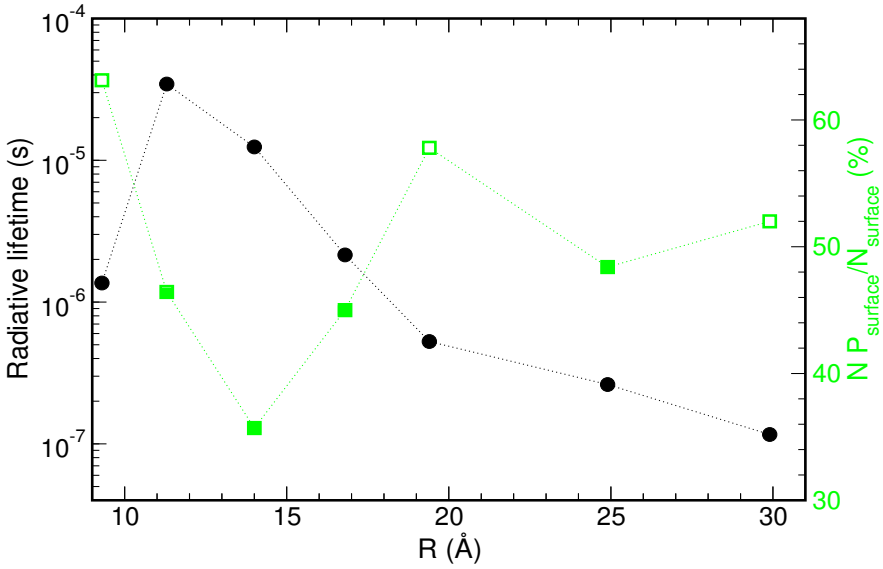

Figure 4.7: Room temperature radiative lifetimes (black circles, left y axis) calculated as a function of QD radius. The fraction of P surface atoms as a percentage of the total surface atoms (green squares, right y-axis) is also displayed. Full squares represent P fractions below 50% (i.e., In-rich surfaces), whereas empty squares indicate P fractions above 50% (i.e., P-rich surfaces).

Indeed, despite the ideal passivation we used to confine both electron and hole to the core region of the dot, we find that the presence of P atoms creates a strong repulsive potential for the hole, pushing its charge density towards the surface, in the case of prevalently In-terminated NCs. For P-rich surfaces, instead, the opposite occurs, and the hole localises more in the dot core. The electron charge density, for which P acts as an attractive potential, is instead always mostly confined to the core, but exhibits some additional surface localisation in the presence of P-rich surfaces. These effects can be clearly observed qualitatively in the charge density distributions presented in Fig. 4.5 (where green dots represent P atoms and red dots In atoms).

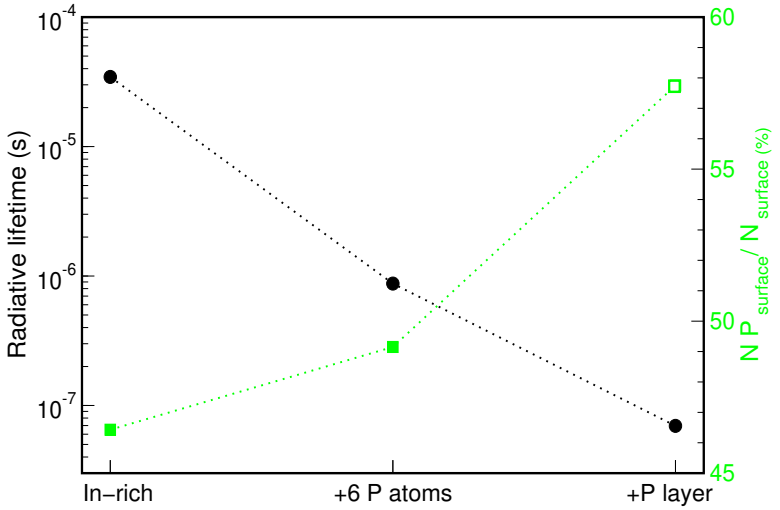

Figure 4.8: Evolution of the calculated radiative lifetime of an InP CQD with $R = 11.3$ Å with increasing P surface coverage, from an In-rich surface to a full P layer coverage. The calculated charge densities of both CBM and VBM relative to the 3 different cases considered are displayed in Fig. 4.6.

A more quantitative comparison is presented in Table 4.3, where the larger difference exhibited between the spatial distribution of the charge densities of VBM and CBM in NCs with In-rich surfaces, compared with P-terminated dots, is especially evident in the inner core (for $R_{\text{int}} \leq 70\%$R), i.e, within spherical volumes with radii $\leq 70\%$R. This difference is also confirmed by the shifts predicted in the band edges positions (see empty circles in Fig. 4.5) following the addition of a single P atom on every equivalent (100) In-terminated facet, for a total of 6 surface P atoms [194]: while the VBM moves away from the bulk VBM to more negative energies, indicating an increase in confinement, the CBM moves closer to the bulk CBM, as a consequence of decreased confinement. The effect of the surface stoichiometry on the band edges' wave functions is summarised in Fig. 4.6, which shows the charge density evolution with increasing surface P coverage from In-rich surfaces to P-rich surfaces: in the former case (left panel) the CBM is well confined to the dot core and the VBM exhibit regions of large charge density close to the surface, whereas in the P-rich case (right panel) the opposite is true.

Element	Electronic Configuration
P	$3s^2 3p^3$
As	$3d^{10} 4s^2 4p^3$
Sb	$4d^{10} 5s^2 5p^3$
S	$3s^2 3p^4$
Se	$3d^{10} 4s^2 4p^4$
Te	$4d^{10} 5s^2 5p^4$

Table 4.4: Electronic configuration of the outer shell of the anions most commonly found in semiconductor NCs

The origin of this effect is the peculiar nature of P, when compared to other widely used group V anions (e.g., As, Sb, etc.). Its electronic configuration is $1s^2 2s^2 2p^6 3s^2 3p^3$: i.e., like all the other anions (see Table 4.4), it has a p-like outer shell, however, unlike other anions, P (like S) has no d-like orbitals. From this point of view comparing In-based pnictogen NCs and Cd-based chalcogen NCs, InP CQDs are more similar to CdS NCs[195] than to CdSe dots. Therefore, it is perhaps not a coincidence that both InP and CdS are plagued by trap states [192, 193, 185, 186, 187, 190, 196, 197, 198], which have proven difficult to eliminate experimentally despite the best efforts at passivating their surface. In addition In and P have large differences in the electronic properties (the outermost electronic configuration of In is $4d^{10} 5s^2 5p^1$, which also contains d-like orbitals) atomic size, and in the electron affinity and ionization potential. In this light, recent density functional theory (DFT) calculations[199] predicted a difference in crystal potential between In- and P-terminated InP dots in the presence of oxidised surfaces.

We expanded our investigation of this effect on analyzing states deeper in the VB, apart from the band edges. This analysis could be particularly interesting when it comes to identifying which states contribute to the optical transitions and yield the best wavefunction overlap with the CBM. Even though we performed the analysis for up to ten states in the VB, here we include the results for up to VB4 (a state that is involved in the optical transitions). The effect of the addition of P atoms at the surface is shown for states that contribute to the optical transition.

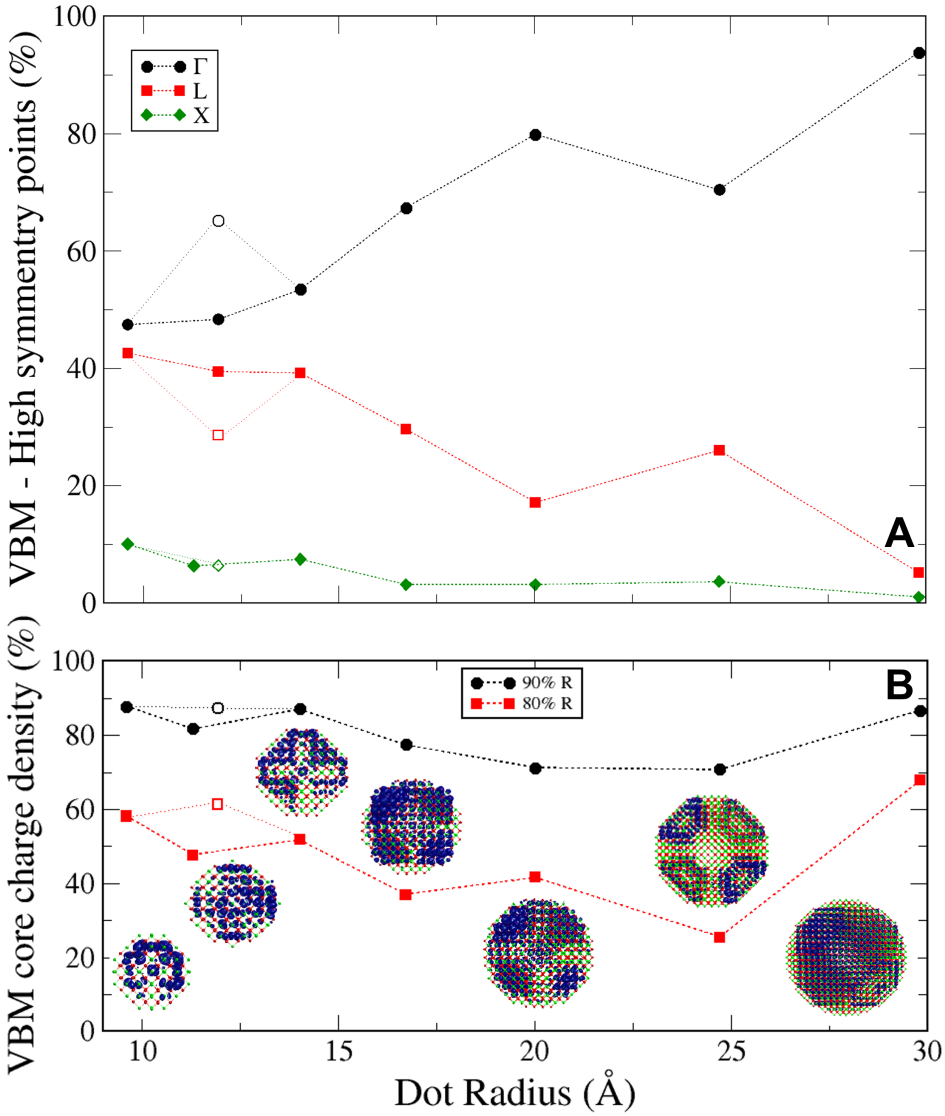

Figure 4.9: Core charge density (top figure) and character (bottom figure) for VBM. Five different settings were used for the charge density calculation, with a radius contraction for 90% and 80% of the dot radius. The unfilled shapes indicate the new values after adding 6 P atoms at the NC surface.

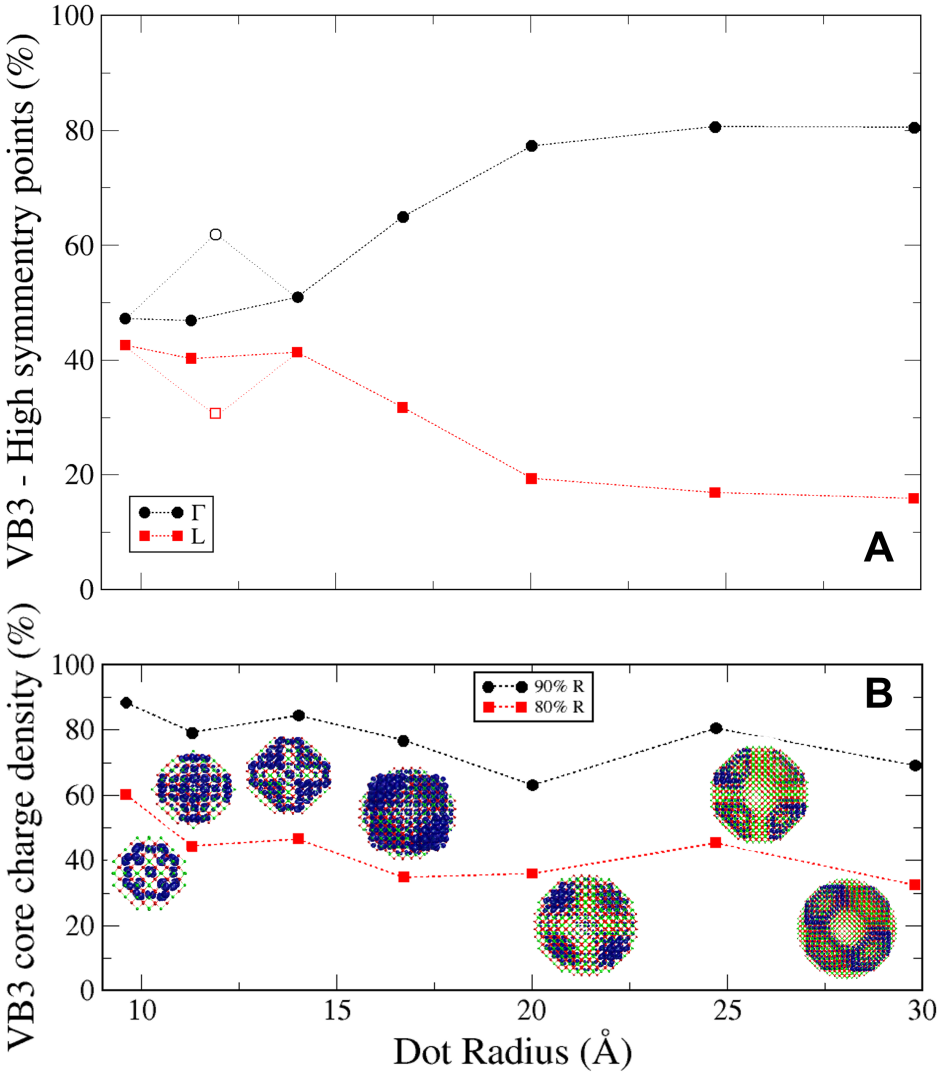

Figure 4.10: Core charge density (top figure) and character (bottom figure) for VB3. Five different settings were used for the charge density calculation, with a radius contraction for 90% and 80% of the dot radius. The unfilled shapes indicate the new values after adding 6 P atoms at the NC surface.

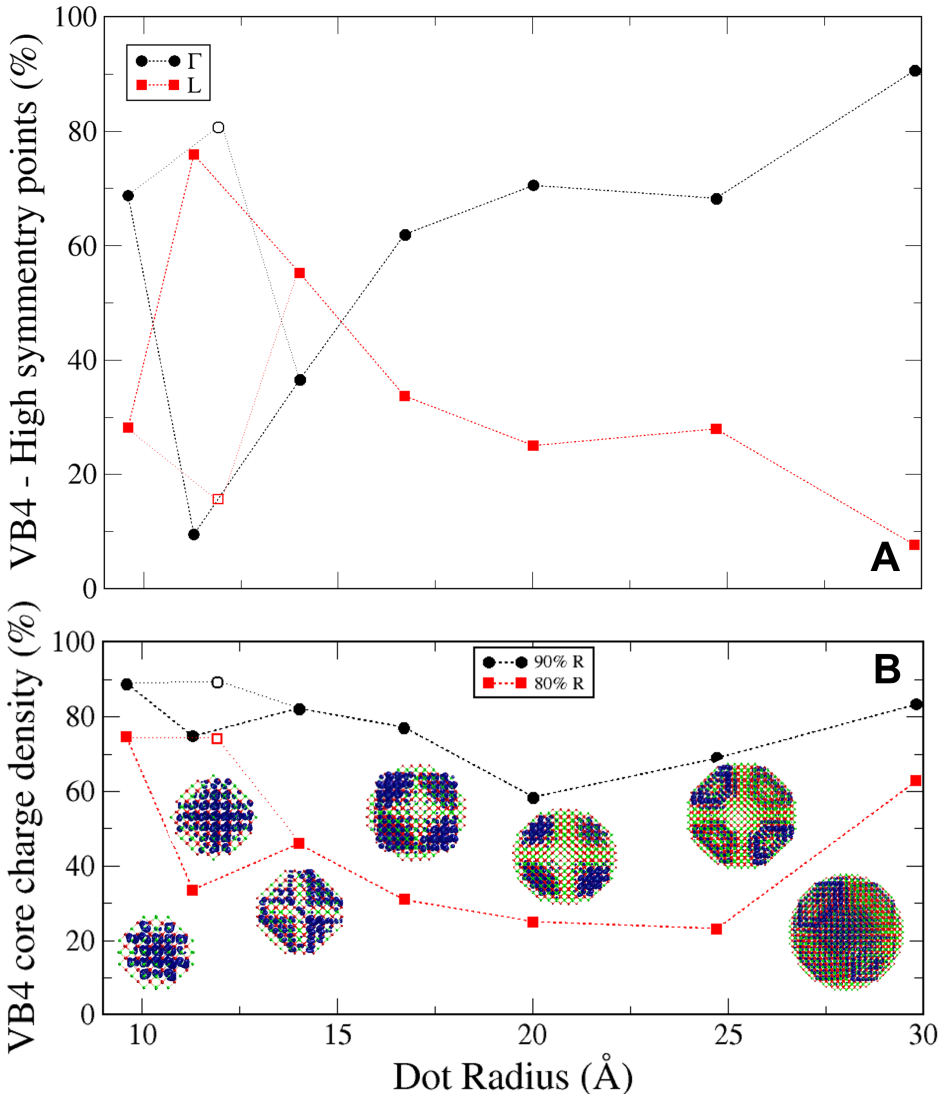

Figure 4.11: Core charge density (top figure) and character (bottom figure) for VB4. Five different settings were used for the charge density calculation, with a radius contraction for 90% and 80% of the dot radius. The unfilled shapes indicate the new values after adding 6 P atoms at the NC surface.

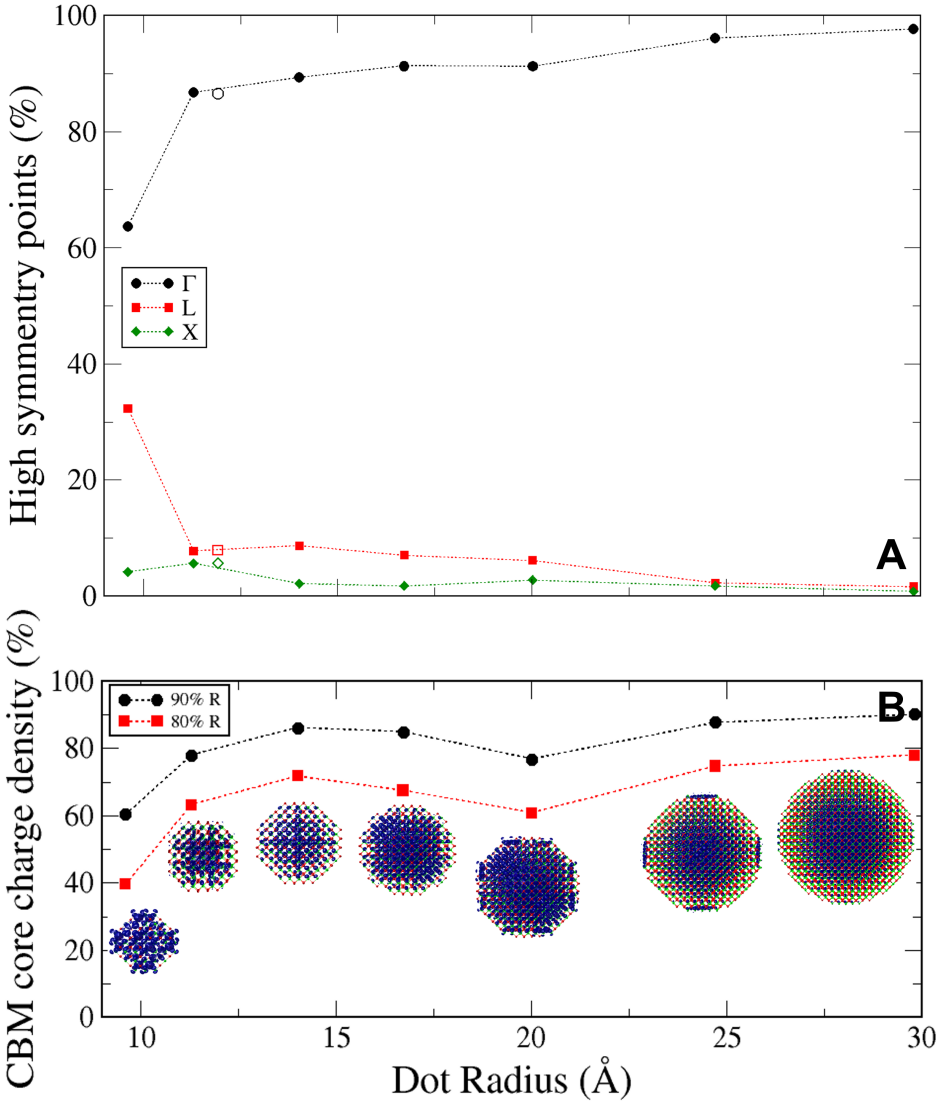

Figure 4.12: Core charge density (top figure) and character (bottom figure) for CBM. Five different settings were used for the charge density calculation, with a radius contraction ranging for 90% and 80% of the dot radius. The unfilled shapes indicate the new values after adding 6 P atoms at the NC surface.

For the case of this NC with an In-terminated surface, we show that the state with the higher Γ component and thus overall core charge density localization is the doubly degenerate VB8 and VB9 states, deep in the VB, while VB4 is completely a L-like state. As a result, the bright state (large dipole matrix

element) is at higher energy and thus the NC exhibits a large Stoke shift, weak emission and slow radiative lifetimes. However, with the addition of the 6 P atoms at the surface this NC has totally different properties: the transition of VB8 and VB9 from a Γ-like to L-like states along with the transition of VB4 from a single L-like state to a Γ-like doubly degenerate state (with VB5), constitute VB4 and VB5 as the dominant states with the highest Γ component and thus the highest core charge density. Consequently, a better wavefunction overlap with the CBM leads to a bright state at a lower energy in the VB, yielding a much smaller Stoke shift, stronger emission, and faster radiative lifetimes. For the In-terminated NCs the difference between the VBM and VB8, VB9 is $\sim$ 192 meV. The difference in energy between VBM and VB4, VB5 for the new NC is $\sim$ 92 meV, 100 meV lower.

Apart from calculating the relevant charge density for each state, their character was determined by calculating the contributions from the high-symmetry points of the Brillouin zone and showed how this is affected when adding 6 P atoms at the surface of a NC with R = 12Å (see Fig. 4.9 - 4.11). In general, we'd expect the charge density to have a better core localization in the case of a higher contribution from the Γ point[200]. Starting from the VBM, which is doubly degenerate, we find that the Γ component increases by $\sim$ 20% when adding the 6 P atoms at the surface. This leads to a corresponding increase of the core charge density, as shown before in Fig. 4.6, and thus a better overlap between the CBM and VBM wavefunctions. VB3 experiences the same effect, being very close in energy to VBM with a difference of only 2.7 meV. For the following three states the addition of the surface atoms results in changing the degeneracy between them. The initial NC had a single VB4 and double degenerate VB5 while the new one yielded a single VB6 and a doubly degenerate VB4. Interestingly for VB4, a huge increase of the Γ component resulted in a complete transition from a L-like to a Γ-like state. VB6 and VB7 maintained a L-like state with insignificant changes. The effect on VB8 and VB9 was a transition from a Γ-like to L-like states, while VB10 maintained its Γ character. For the CBM, the changes are negligible as shown in Fig. 4.12.

4.4 Optical Properties

As a consequence of the relative displacement between the charge densities of VBM and CBM, where the former is more localised on the core outer shell and the latter more in the core centre (as shown in Fig. 4.5), the overlap between their wave functions is strongly reduced, leading in extreme cases (i.e., for small NC sizes with In-terminated surfaces) to (i) a completely dark[201] ground state exciton manifold (i.e., the 8 exciton states derived from $(e_1, h_{1,2})$ - where e_1 is the CBM and $h_{1,2}$ is the doubly degenerate VBM - are all optically forbidden), and (ii) tens-of-microseconds-long radiative lifetimes (Fig. 4.7). We note that these features are not an artefact of our specific choice of passivants, as they also emerge using the passivation set from Graf *et al.* [95]. Interestingly we find that both these effects are correlated to the fraction of P surface atoms, at least for small NC sizes, where to larger fractions correspond brighter excitons and faster radiative recombinations. The confining effect of surface P on the VBM wave function is so strong that, in the case of $R = 12$ Å where the surface is In-rich, the simple addition of a single P atom on every equivalent (100) In-terminated facet [194] (for a total of 6 added P atoms) leads to a reduction in the radiative recombination time by over one order of magnitude, from tens of microseconds to hundreds of nanoseconds. A further increase of P surface coverage leads to even faster recombination, of the order of tens of nanoseconds (Fig. 4.8) and to a full recovery of a bright exciton in the ground state manifold. This effect is stronger for smaller sizes, where the surface atoms represent a substantial fraction of the total number of atoms. In larger structures the effect of surface stoichiometry becomes less important and the radiative lifetime is the result of a combination of surface effects and volume increase (a comparison between radiative lifetimes calculated in NCs with P-rich and In-rich surfaces is presented in Fig. 4.13). Indeed we find that, as it is the case for other materials (such as CdSe [202] and GaSb [71]), τ_{rad} decreases with increasing dot size.

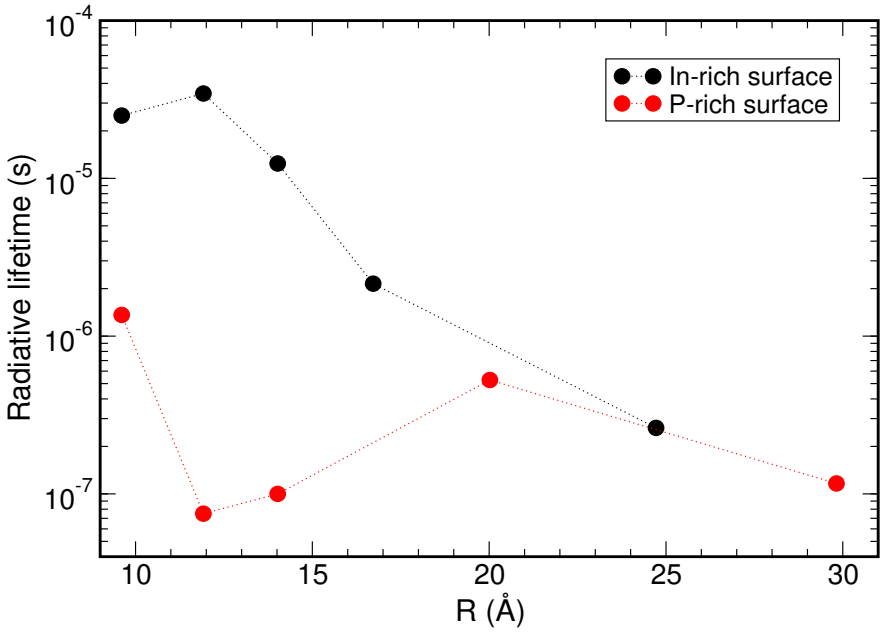

Figure 4.13: Comparison between radiative lifetimes calculated in NCs with P-rich (red circles) and In-rich (black circles) surfaces.

These findings seem to find support from (and, at the same time, may be able to provide additional insight into) recent measurements of lower PL QYs in In-rich (compared with stoichiometry-controlled) InP/ZnSe core/shell and InP/ZnSe/ZnS core/shell/shell NCs [176]. The difference between the QYs in the two systems was shown to be due to the gradual In incorporation in the epitaxially grown ZnSe and ZnS shells that occurred in NCs synthesised using the conventional route, but not in those obtained using a stoichiometry-controlled synthesis. The presence of In atoms (known electronic dopants for II-VI materials) in the shell(s) was assumed to generate intra-gap states, leading to non-radiative recombination, hence to QY degradation. Our results discussed above suggest the presence of a possible additional component to the QY reduction in In-rich samples, especially considering the small size of the InP core ($R = 1.4$ nm) in those experiments.

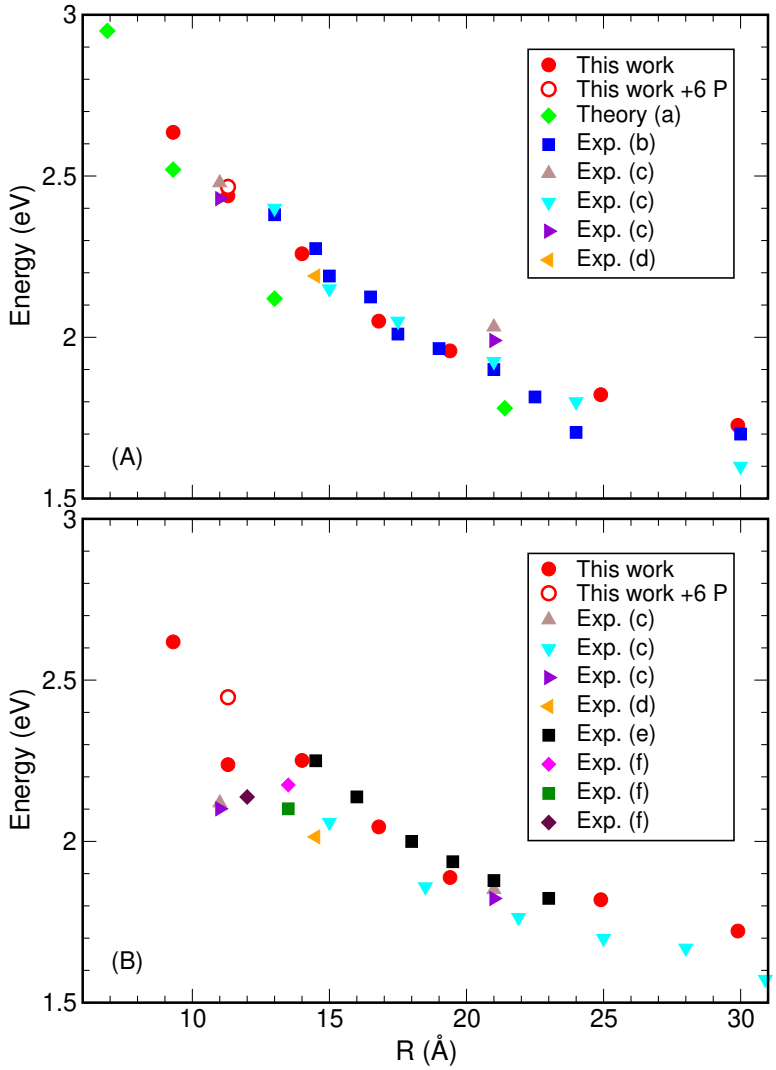

Figure 4.14: Absorption (A) and emission (B) spectra: comparison of our results (red circles) with experimental (coloured symbols) and theoretical (green diamonds) studies. (a): [97]; (b): [175]; (c): [203]; (d): [185]; (e): [204]; (f): [205].

The NC surface stoichiometry does not affect appreciably the position of the absorption edge (as shown in Fig. 4.14A, where the red circles indicate our results - the empty red circle represents the calculated bandgap after the addition of 6 P atoms on the surface), as the bright transitions it corresponds to have similar energies for all surface terminations. These transitions, however, are not to the same states. Indeed, for smaller, In-terminated dots, the first optically allowed

transition occurs to an exciton state (different for the different sizes) that is contributed to by either highly excited hole states and the CBM ($|h_j; e_{\mathrm{cbm}}\rangle$), or by the VBM and excited electron states ($|h_{\mathrm{vbm}}; e_k\rangle$), precisely owing to the aforementioned relative displacement between the charge densities of VBM and CBM, which yields a small overlap between them. This leads to large Stokes' shifts and weak PL intensities for these nanostructures, as the emission always originates from the dark[201] ground state manifold which is located at a much lower energy (see Fig. 4.15a, where we show both absorption - blue lines - and emission - red lines - spectra calculated for a $R = 11.3$ Å NC with an In-rich surface). In NCs with P-rich surfaces, instead, an optically allowed exciton state exists within the ground state manifold, leading to small Stokes' shifts, and stronger and faster emission (see Fig. 4.15b - same NC as in Fig. 4.15a, but with inverted stoichiometry).

In one of the seminal papers by Nozik's group [206], InP NCs were prepared using both excess In and excess P in their synthesis, however, in that study, it had been impossible to separate the effects of surface stoichiometry from those of the presence of trap states, on the optical properties. Indeed, as the capping agent used (TOPO) coordinates mainly with In^{3+} surface ions, the presence of excess P was associated by Micic *et al.* [206] with incomplete surface passivation, which leads, *inter alia*, to a broad size distribution, hence to a broad PL spectrum. On the other hand, in NCs prepared with excess In^{3+}, the presence of an additional broad PL feature at low energies was attributed to radiative surface states produced by phosphorus vacancies [206, 193]. Nevertheless, they were still able to conclude that the Stokes' shifts they observed between the emission peak and the first absorption peak were related to core effects, and did not depend on the presence of any surface trap, as their magnitude did not change after treatment with HF or other etchants.

In general, due to the presence in experimental samples of a mixture of In- and P-terminated NCs, and of a distribution of sizes, the emission is often broad and the observed Stokes' shift consequently small.

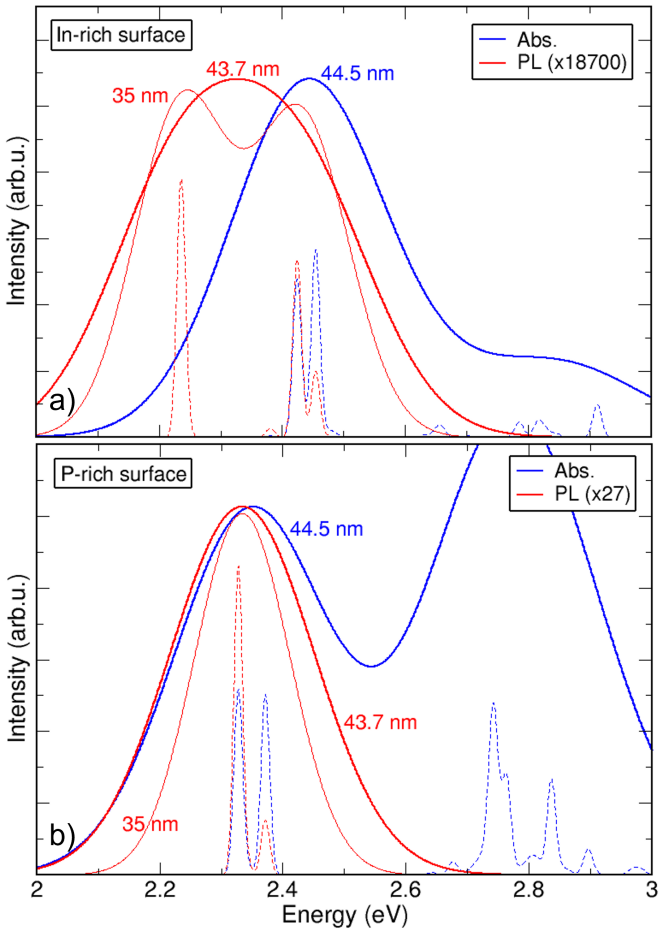

Figure 4.15: Room temperature absorption (blue lines) and emission (red lines) spectra for an InP NC with $R = 11.3$ Å with an In-rich (top panel) and a P-rich (bottom panel) surface. The top structure is anion-centred, the bottom one has an inverted stoichiometry (i.e., anions and cations are interchanged), and is cation-centred. The spectra are calculated for different experimental linewidths (44.5 nm [208], thick blue lines; 43.7 nm [208], thick red lines; and 35 nm [207], thin red lines), and also using a much smaller - and, so far, experimentally unachievable - linewidth (17 meV, dashed lines), in order to show how the relative positions of optical transitions and spectral peaks may vary, depending on the value of the linewidth. The peaks were broadened using a Gaussian function, as described in Eq. 2.33. The experimental broadening corresponds to the non-homogeneous broadening due to size dispersion in experimental samples. The PL amplitude has been normalised to that of the first absorption peak by multiplying it by a factor of 1.87×10^4 (top panel) or 27 (bottom panel), i.e., the PL amplitude in the NC with an In-rich surface is about 3 orders of magnitude smaller than that in the NC with a P-rich surface. The ratio between the first absorption peak intensity for the two NCs is almost unity (1.05), meaning that the absorption has similar intensity despite the change in NC surface.

In Fig. 4.15 we show how, for the case of an InP NC with $R = 11.3$ Å, the relative positions of optical transitions and corresponding spectral peaks depend crucially on the value of the experimental linewidth: large linewidths mask the actual position of the optical transitions, resulting in a blue-shift of the PL peak and in a consequent reduction of the observed Stokes' shift. Smaller linewidths, still within experimental capabilities [206, 207], allow to recover the *real* position of the optical transitions providing a more accurate PL energy. This could explain why the position of the PL measured by different groups (or in different samples by the same group) in dots with the same nominal size exhibits a wide range of variation, as shown in Fig. 4.14B, compared with that of the absorption edge (Fig. 4.14A).

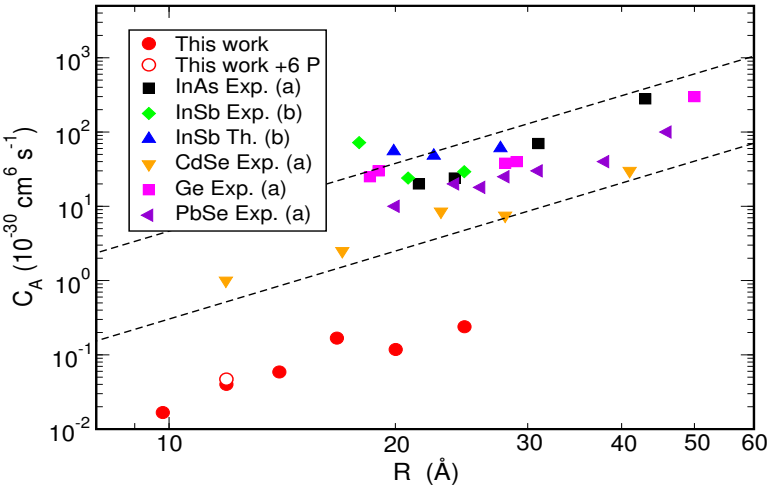

Figure 4.16: Auger Constant as a function of QD radius: comparison with experiment. (a): [212]; (b): [209]. The dashed lines indicate the universal scaling boundaries from Robel *et al.* [212].

In general, Auger processes (Auger Recombination, AR, and Auger electron Cooling, AC) are very efficient in CQDs: in CdSe NCs, observed AR times range from a few to a few hundreds of picoseconds (they are even faster in NCs made of other semiconductor materials [210, 209]), whereas AC times are of the order of hundreds of femtoseconds [211, 108], and they all increase with NC size.

In contrast with these expectations, and consistently with our findings relative to the radiative lifetimes, we find longer Auger lifetimes than usual for both

processes: our calculated Auger recombination times range from about 120 ps for $R = 9.3$ Å, to 2080 ps for $R = 24.9$ Å, and although they follow the observed trend with NC size highlighted by Klimov's group [212], they are about at least one order of magnitude slower, if compared with what is observed in CdSe NCs [211], and two to three orders of magnitude larger than the AR lifetimes in InSb [210, 209]. This is shown in Fig. 4.16, where, following Robel *et al.* [212], we plot the Auger constant C_{A}, defined as

$$C_{\mathrm{A}} = \frac{V_0^2}{(8\tau_{AR})} \tag{4.1}$$

(where V_0 is the NC volume and τ_{AR} is the AR lifetime), as a function of dot size.

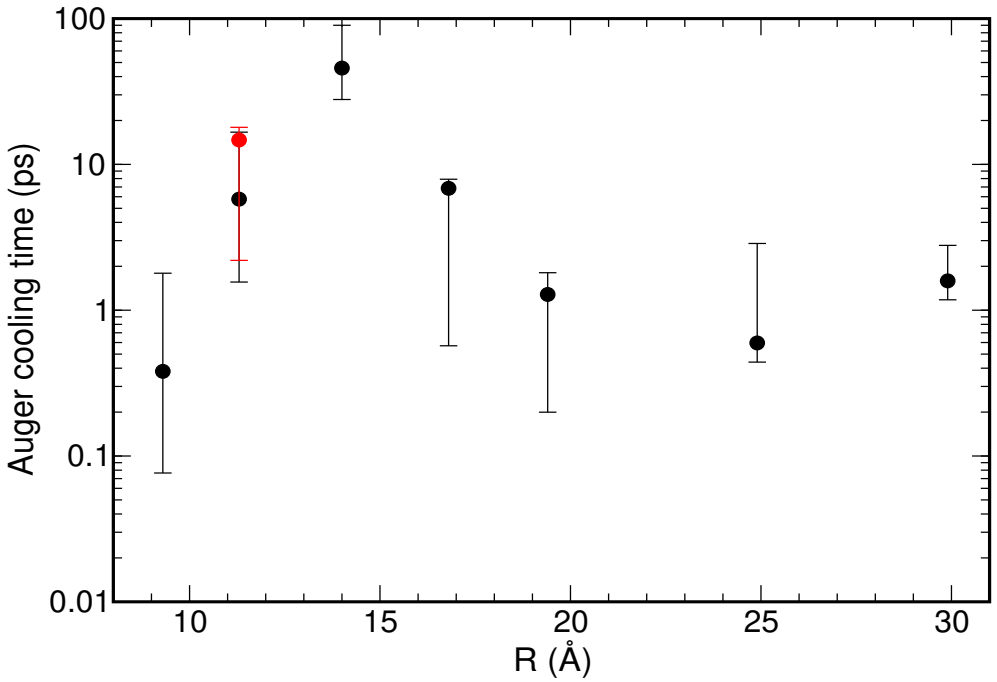

Figure 4.17: Auger Cooling lifetimes as a function of QD radius. The red circle represents the result obtained after the addition of 6 P atoms, one on each of the equivalent (100) facets of the NC. The error bars are obtained using a procedure similar to that followed in ref. [209], by varying the s-p splitting in the conduction band over a range of energies corresponding to a 10% size distribution.

Unfortunately, this strong suppression of AR is accompanied, as discussed

above, by a similar suppression of radiative recombination, resulting in an overall faster AR channel.

Similarly, our predicted AC lifetimes are about one order of magnitude longer than in CdSe [211, 108], ranging from a few hundreds of femtoseconds to a few picoseconds (see Fig. 4.17). The only exception is represented by $R = 14$ Å, in which the first electron excited state has an s-like character and is nondegenerate, in contrast to the (nearly) 3-fold degenerate p-like states that are found in all other sizes, resulting in a much longer lifetime than in all other dots considered in this study. We find that the details of the surface stoichiometry have a weaker effect on all Auger processes than they have on the emission properties (compare empty and solid red circles in Fig. 4.16 and Fig. 4.17), as the former involve both band edge and excited states, whose charge densities normally exhibit a relative displacement.

4.5 Conclusions

In conclusion, we have shown that small InP NCs with an ideally passivated P-rich surface exhibit faster radiative recombination, stronger emission, and smaller Stokes' shifts compared to NCs whose surface has a prevalence of In atoms. The latter show long lifetimes and weak emission despite the presence of a full passivant coverage, i.e., in the absence of any trap states, owing to the existence of a relative displacement between the charge densities of CBM and VBM (hence a reduced coupling between them), that gives rise to a completely dark ground state exciton manifold extending over a considerable energy window. Our results, therefore, suggest that, in such NCs, commonly adopted strategies to improve emission QY by removing surface traps may fail if they do not, at the same time, provide additional confinement for the hole. Indeed, recent InP/ZnSe/ZnS core/multiple-shell structures exhibiting near-unity QYs, successfully address both issues: they minimise the number of defects by preventing oxidation and strain formation at the heterojunctions, on the one hand, and, on the other hand, by exploiting the large valence band offset (of the order of 1 eV [213]), between core and shell material, they provide strong additional confinement for the hole. HF treatment on its own, however, only addresses the first

issue, as it removes undercoordinated surface P atoms, responsible for the formation of gap states. Although this may lead to a relative improvement in the PL efficiency [214], HF etching results in In-rich surfaces [214], and we have shown here that, even in ideally passivated NCs, such as surface stoichiometry, adversely affects hole confinement, thereby compromising the emission.

We propose that this effect is particularly strong in InP NCs due to the peculiar electronic structure of P atoms which, like that of S, lacks d orbitals.

Chapter 5

Transport Properties of Environmentally Friendly NCs

Two-dimensional quantum dot arrays are considered as promising candidates for a wide range of applications that heavily rely on their transport properties. Existing QD films, however, are mainly made of either toxic or heavy-metal-based materials, limiting their applications and the commercialization of devices. In this theoretical study, we provide a detailed analysis of the transport properties of environmentally friendly colloidal QD films (In-based and Ga-based), identifying possible alternatives to their currently used toxic counterparts. We show how changing the composition stoichiometry and the distance between the QDs in the array affects the resulting carrier mobility, for different operating temperatures. We find that InAs QD films exhibit high carrier mobilities, even higher compared to previously modelled CdSe (zinc blende) QD films. We also provide the first insights into the transport properties of properly-passivated InP and GaSb QD films and envisage how realistic systems could benefit from those properties. Ideally passivated InP QD films can exhibit mobilities an order of magnitude larger compared to what is presently achievable experimentally, which show the smallest variation with (i) increasing temperature when the QDs in the array are very close and (ii) increasing interdot distance at low operating temperatures (70 K), among the materials considered here, making InP a potentially ideal replacement for PbS. Finally, we show that by engineering the QD stoichiometry

it is possible to enhance the film's transport properties, paving the way for the synthesis of higher performance devices.

5.1 Band-like transport and CQD films

The unique size-tunable optical properties of semiconductor quantum dots (QDs) make these systems ideal candidates for a wide range of applications [215, 216]. In addition, the combination of strong interdot coupling along with the assembly of QDs in arrays can create novel materials which take advantage of such properties and the high carrier mobilities of the bulk [217]. However, the mechanisms involved in carrier transport in these materials are still debated. One of the approaches is to model carrier transport by hopping, where the electron "hops" from a localized quantum dot state to another in the array [218]. Another approach is to model carrier transport by band-like mechanisms: the array regimentation leads to the rise of a band structure from the isolated QD states (miniband structure due to the narrower bandwidths) [219, 69]. In general, it is accepted that the signature of band-like transport is the decrease of carrier mobility with temperature, although this behaviour could also be reproduced in hopping transport in a reduced temperature range [69]. However, the experimental trend is towards achieving periodic QD regimentation and reducing the interdot distances by reducing the size of the ligands. In this regime the eigenstates of the individual quantum dots are expected to exhibit strong coupling, leading to band formation. Aiming to model transport in such systems, we will then apply a band-like approach.

A particular case of QD array is the colloidal QD film, a two-dimensional array that, also thanks to its cheap synthesis[220], finds applications in many fields such as photovoltaics, optoelectronics, LEDs, transistors[221, 222, 223, 70]. In this work, we will focus our attention on non-toxic QD films, which may represent a suitable alternative to replace the currently used toxic lead- or cadmium-based ones, allowing an expansion of their commercialization[224].

We study carrier transport in QD films consisting of same-sized QDs two-dimensionally periodically distributed. In our calculations, we assume that the electrons are scattered by fluctuations in the dot size [225], due to the presence

of dots with a smaller diameter compared to the periodic ones with radius R-δR acting as scattering centers (impurity dots). To investigate the effect of different anions we considered In-based materials (InP, InAs and InSb), we then studied the effect of changing the cation from InSb to GaSb. Our periodic dots have a total of 275 atoms while the impurities have 199 atoms and the radius of the QDs differs for each material due to the different lattice constants. The exact same dots were used for all materials considered here, but changing the atomic types accordingly.

Our individual QDs were generated by starting from a central atom and adding atomic layers up to a specific cut-off radius. The QD surfaces were terminated using ideal passivants (eliminating any surface states) [95], as described in Chapter 2. The interdot separation considered in this study could be achievable experimentally using extremely short ligands (e.g. oleic acid, oxalic acid) or inorganic capping (e.g. atomic halide anions). The single-particle energies and wave functions of the isolated dots were obtained by solving the Schrödinger equation (including spin−orbit coupling), using the state-of-the-art semiempirical pseudopotential method [98]. A periodic array is modelled by placing quantum dots in a square lattice. The quantum dots were separated by the interdot distance (d), defined as the distance between the surface atoms of neighboring QDs in the array, measured in bond lengths (b.l.). In our calculation we assume 1 b.l. as the minimum distance between two QDs. Two different stoichiometries were considered in each case (cation-centred and anion-centered leading to anion-rich and cation-rich surfaces respectively). A 1% density of impurities was assumed as a realistic value in accordance to experimental samples [226].

We solved the Schrödinger equation of the QD film by means of the tight-binding model (see Chapter 2) using a basis consisting of seven or eight conduction band eigenstates of the QD depending on the material. This yields the electronic structure of the system, i.e. the QD film miniband structure, as shown in Fig. 5.1.

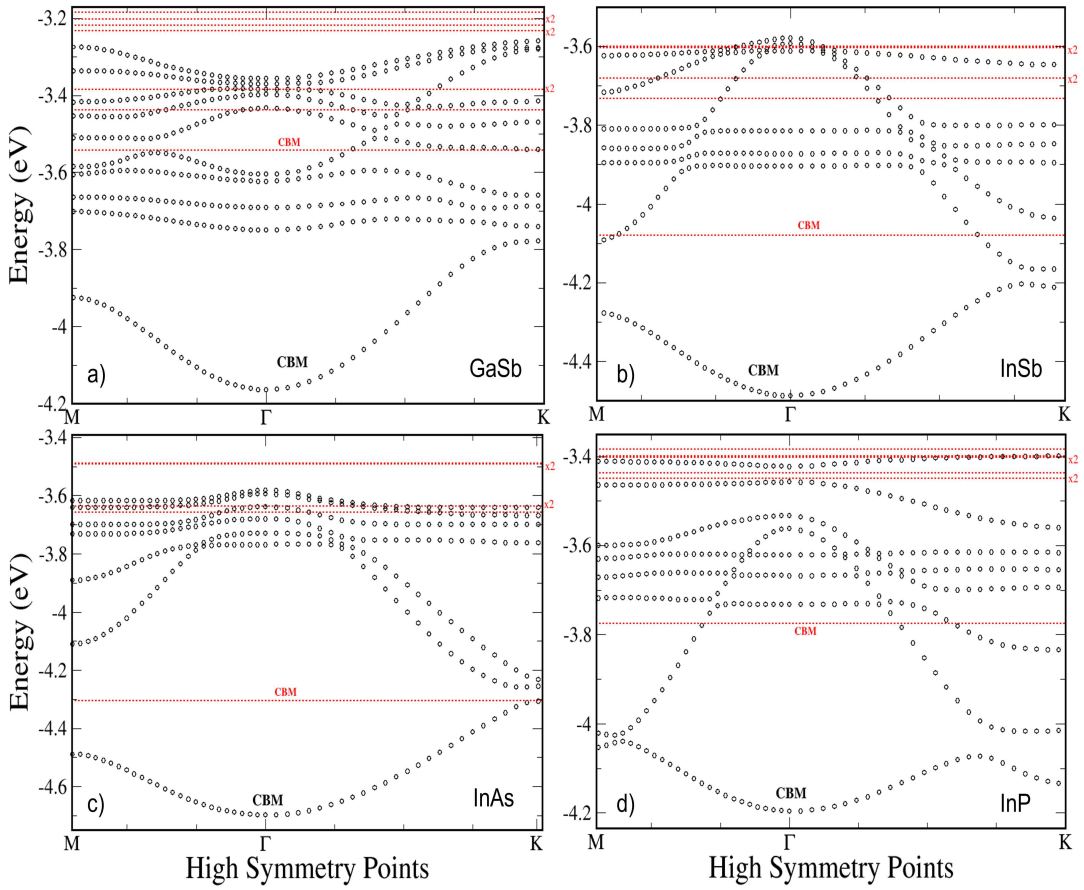

Figure 5.1: Conduction miniband structure (black dots) for (a) GaSb, (b) InSb, (c) InAs and (*d*) InP QD films in the reciprocal space and respective single-particle energy states (red dashed lines). The calculated energies are relative to vacuum.

In the figure the single quantum dot eigenenergies are indicated too. In accordance to the tight-binding formalism, as described in [227], we can expect the lowest energy miniband to exhibit a redshift with respect to the energy of the CBM of the isolated dot proportional to the integral $\int \phi^*_{\mathrm{CBM}}(\vec{r}) \sum \vec{R}_n V(\vec{r}-\vec{R}_n)\phi_{\mathrm{CBM}}(\vec{r})d\vec{r}$, where $\phi_{\mathrm{CBM}}(\vec{r})$ is the CBM wave function and $V(\vec{r}-\vec{R}_n)$ is the potential of the neighbouring quantum dot. The summation is carried out over the four nearest neighbours in the periodic lattice. The larger the integral, the larger the miniband shift relative to the single quantum dot eigenenergy. In our case, we find that GaSb QD films yield the larger integral (-91 meV per neighbour) and thus

the shift is the largest. InAs and InSb have the lowest integrals (-46 meV and -48.7 meV per neighbour, respectively), while the integral for InP QD films is found to be -62 meV per neighbour. These values are in agreement with the shift of the minibands as shown in Fig. 5.1.

In the next step, the transport model described in [69] is implemented (see Chapter 2). Fermi's Golden Rule is used to compute the electron scattering rates. The scattering mechanism is elastic, and therefore the initial and final states have the same energy. The scattering rate for an electron in the lowest energy miniband to scatter from state i to state f is obtained as:

$$\Gamma_{i,f} = \frac{2\pi\nu}{Q_s \hbar \Delta E} \left| \langle f | \, \Delta V \, | i \rangle \right|^2 \tag{5.1}$$

where ν is the impurity ratio in the sample, Q_s is the number of states sampled in the reciprocal space, $\hbar$ is the reduced Planck constant, ΔE is the energy interval in which scattering is considered elastic (due to numerical implementation, transitions between states with energies within the energy interval are considered to conserve energy), f and i stand for the final and initial eigenstate wavefunctions and ΔV is the perturbation to the periodic potential of the array i.e. the difference between the potentials of the periodic and the impurity dot. This difference is mainly observed close to the QD surface because the impurities are obtained by removing atoms from the surface of the periodic dot. As a consequence the difference between periodic and impurity QD potentials, together with the behaviour of the wave functions of the initial and final states, are crucial to determine the flight times between scatterings. The average flight time has been calculated by averaging the flight times of a sampling of 51 $\times$ 51 initial states in the Brillouin zone. The error corresponds to the flight time's standard deviation.

Once the $\Gamma_{i,f}$ are obtained for each pair of states in the miniband conserving energy, mobility is obtained using the formalism presented in [69]. For a given electric field, the average electron velocity depends on the direction of application because of the anisotropy of the QD film. Two eigenvalues of the mobility tensor are presented throughout this study for each QD film, corresponding to two perpendicular directions in the 2D plane of the film (more information is available in

Chapter 2). The Fermi energy (E_F) was placed at the bottom of the lowermost conduction miniband. This can be achieved by either a moderate photodoping in the system or impurity doping in the neighbouring regions. An electric field of 1×10^3 V/m was used, low enough to be in the ohmic regime and high enough to guarantee the numerical stability in the calculation. The mobility values we calculate are in agreement with other QD films of other materials (of the same order of magnitude), meaning that the QD material does not crucially modify the mobility values. However, we focused on In-based and Ga-based materials due their environmentally friendly character. Specifically, comparing our findings with previously modelled QD films based on CdSe, PbS and PbSe QDs with similar QD sizes as the ones considered here, we investigate how the composition of the QD affects the transport properties of the film. Therefore, we propose potential alternatives for these toxic materials.

5.2 In-based QD films

Isolated In-based QDs have been proposed as promising candidates for replacing their toxic counterparts (e.g. CdSe, PbSe, PbS etc.). This work aims to investigate whether this replacement is also viable in the case of 2D arrays.

The mobility of films of InAs CQDs is calculated for temperatures ranging between 50 K and 350 K (corresponding to a realistic range for device operation), and our results are compared with available experiment. Fig. 5.2 illustrates the mobility dependence on temperature for four different interdot separations for this material. The specific values for d are related to the sampling of the bulk crystal unit cell in grid points. The values of d correspond to increments in the QD separations of two grid points. The carrier mobility is reduced with increasing temperature. This decay rate becomes larger with increasing d: for $d = 1$ b.l. the decay is $\sim$ linear while for larger d it becomes more exponential. Additionally, as d is increased the mobility value for a given temperature is reduced due to the weaker wave function overlap between neighbouring QDs. In Fig. 5.3, we investigate the variation of mobility with increasing separation for two different temperatures (one for device operation at low temperatures and one for operation at higher temperatures). The mobility for an interdot separation of 1 bond length

is not affected much by the change in temperature, however, placing the QDs in the array even further causes the mobility to drop with much faster rates. We find that this decay is nearly exponential. The origins of this behaviour can be attributed to the exponential dependence on d of the wave function overlap between neighbour quantum dots which determines the miniband width (defined as the difference between the lowermost energy point and the highest energy point of the miniband): the larger the overlap, the wider the miniband. Wide minibands lead to smaller effective masses and, therefore, higher mobilities in general. Therefore, increasing the interdot distance would result in an exponential increase of the effective mass and therefore an exponential decrease in mobilities (as shown later on). For higher temperatures this decay rate is slightly faster compared to lower temperatures.

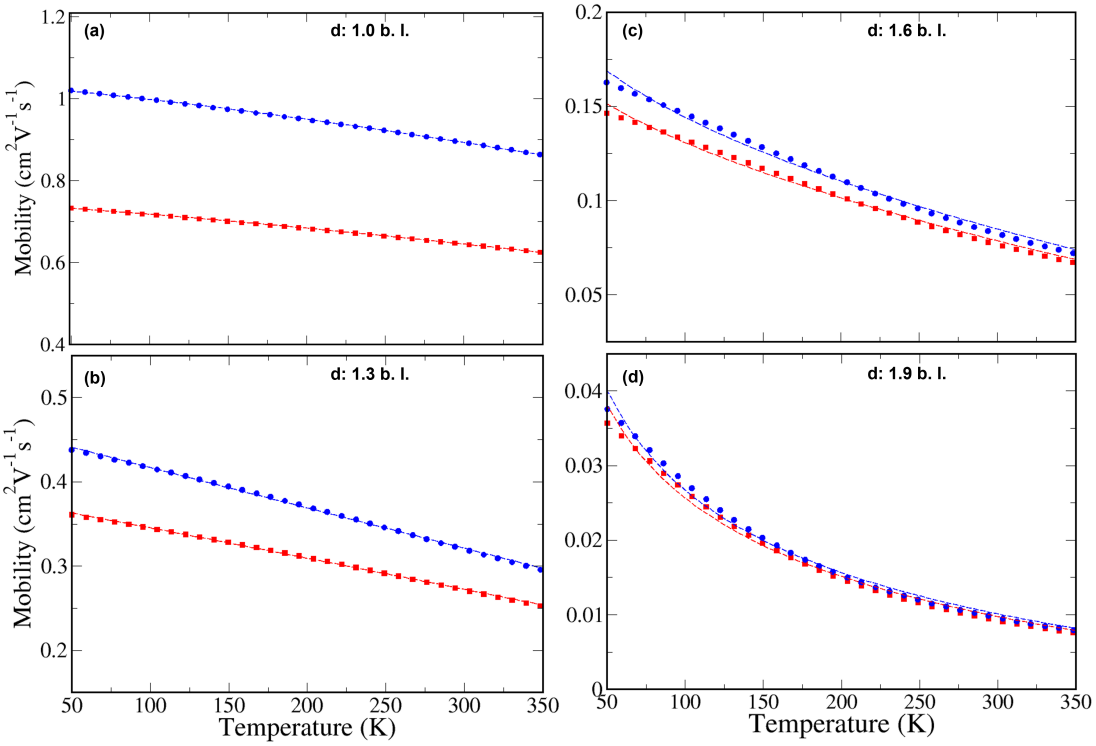

Figure 5.2: Electron mobility as a function of temperature for InAs QDs, where the QDs are separated by (a) 1, (b) 1.3, (c) 1.6 and (d) 1.9 b.l. The blue and red lines represent the two eigenvalues of the mobility tensor.

It was previously shown experimentally [228] that by using InAs QDs capped with molecular metal chalcogenide ligands the electron mobility is nearly 1 order of magnitude larger than what we find here. This is attributed to the fact that those ligands act as a 'bridging' mechanism for the QDs in the array. The same study emphasizes the importance of the surface termination of QDs when it comes to the determination of their transport properties: different capping agents can yield different inter-dot coupling.

Their experimental trend of mobility vs temperature is in qualitative agreement with our results as can be seen in Fig. 5.4A, where the range of the y-axis for the two cases is different (The right-hand y-axis is obtained by multiplying the y-axis axis on the left by a factor of 20). A similar decay rate for the mobility decrease with temperature was also observed in InAs films [229] (i.e. in 2D InAs, as opposed to 2D arrays of InAs QDs), where band-like transport is expected. Mobilities with similar values (1.1 $cm^2V^{-1}s^{-1}$) to those we find in InAs QD films were recently measured in $MAPbI_3$ thin films by Sanehira et al. [230]. In addition, they synthesized $CsPbI_3$, $FAI - CsPbI_3$, PbS and PbSe QD films with mobilities of 0.2 $cm^2V^{-1}s^{-1}$, 0.5 $cm^2V^{-1}s^{-1}$, 0.04 $cm^2V^{-1}s^{-1}$ and 0.08 $cm^2V^{-1}s^{-1}$ respectively at room temperature, which are all lower compared to our InAs QD films. These results suggest that: (i) InAs QD films could be good candidates to replace Pb-based QD films, at least from the point of view of their mobility; (ii) as our transport results reproduce observed trends, the carrier dynamics in real samples could be close to that modelled in our approach.

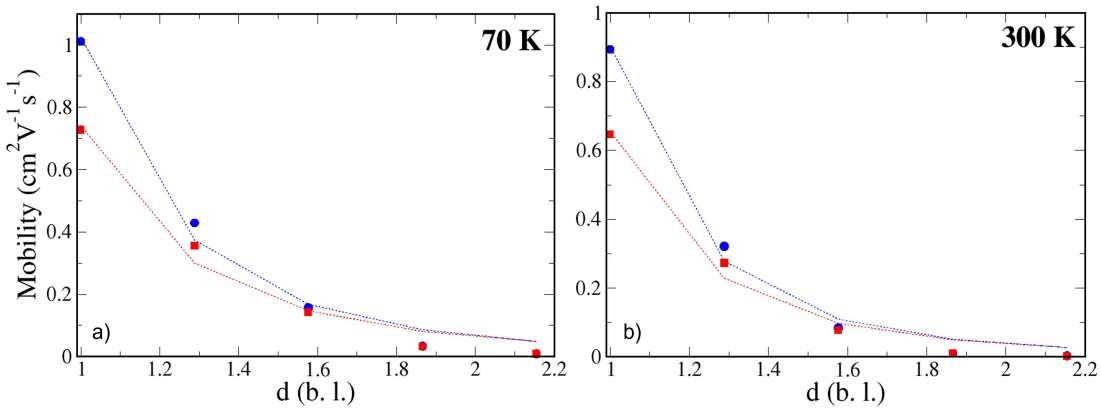

Figure 5.3: Mobility as a function of increasing inderdot separation for (a) 70 K and (b) 300 K for InAs QD films. The blue circles and red squares represent the mobility tensor eigenvalues. The dashed lines represent a theoretical fitting to our findings.

From the point of view of their mobility, InAs QD films can also be considered as potential replacements for Cd-based QD films. Indeed, the mobility for zinc blend CdSe (zinc blende) QD films of identical size to the QDs considered here, was predicted [231] to be 1 $cm^2V^{-1}s^{-1}$ at room temperature and with an interdot separation of 1 bond length, which is similar to the mobility of InAs QD films in this work, and it is in agreement with experiment [217, 232]. The 2D lattice that is considered in this study refers to a square lattice where the two mobility eigenvalues (that form the mobility tensor) correspond to two perpendicular directions in the 2D plane of the film (see Chapter 2).

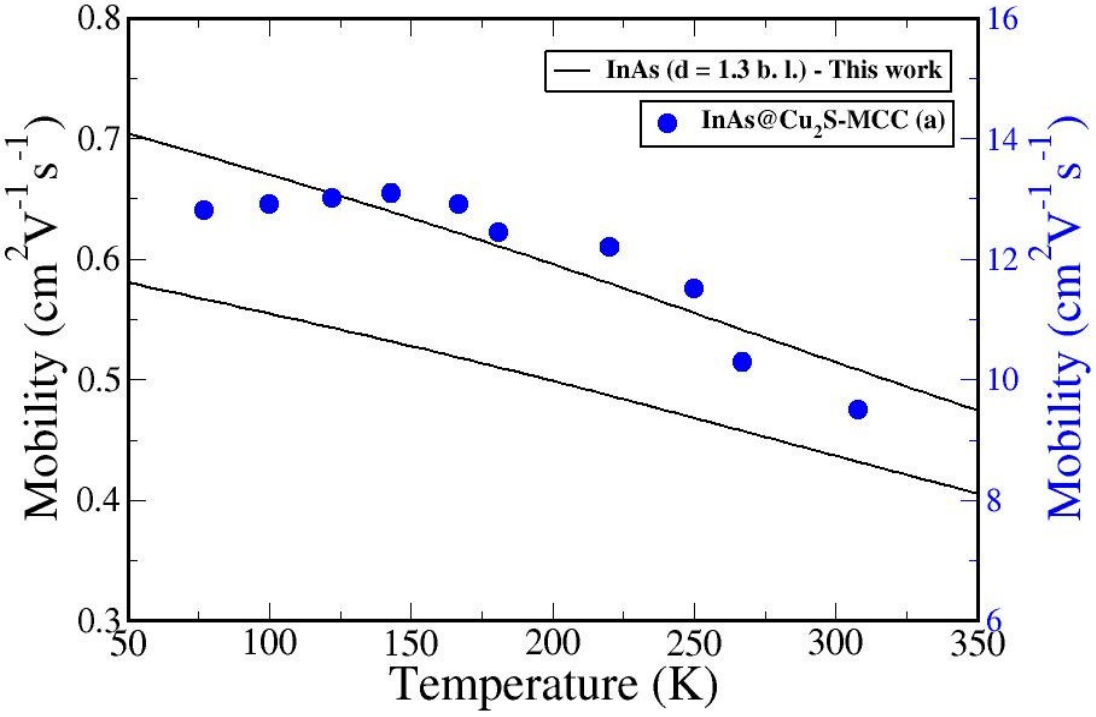

Figure 5.4: Mobility as a function of temperature: comparison with experiment: (a) ref [228]. Our mobility eigenvalues are shown as black lines while the experimental data are presented with blue dots.

Keeping the cation the same and replacing As with P, we find that the value of the mobility for all interdot separations and all temperatures is reduced, as shown in Fig. 5.5. The decay rate with increasing d is similar to InAs and is illustrated in Fig. 5.6. The mobility reduces gradually from ~ 0.65 cm^{2}V^{-1}s^{-1} to ~ 0.01 cm^{2}V^{-1}s^{-1} for d increasing from 1 to 2.2 b.l., at room temperature.

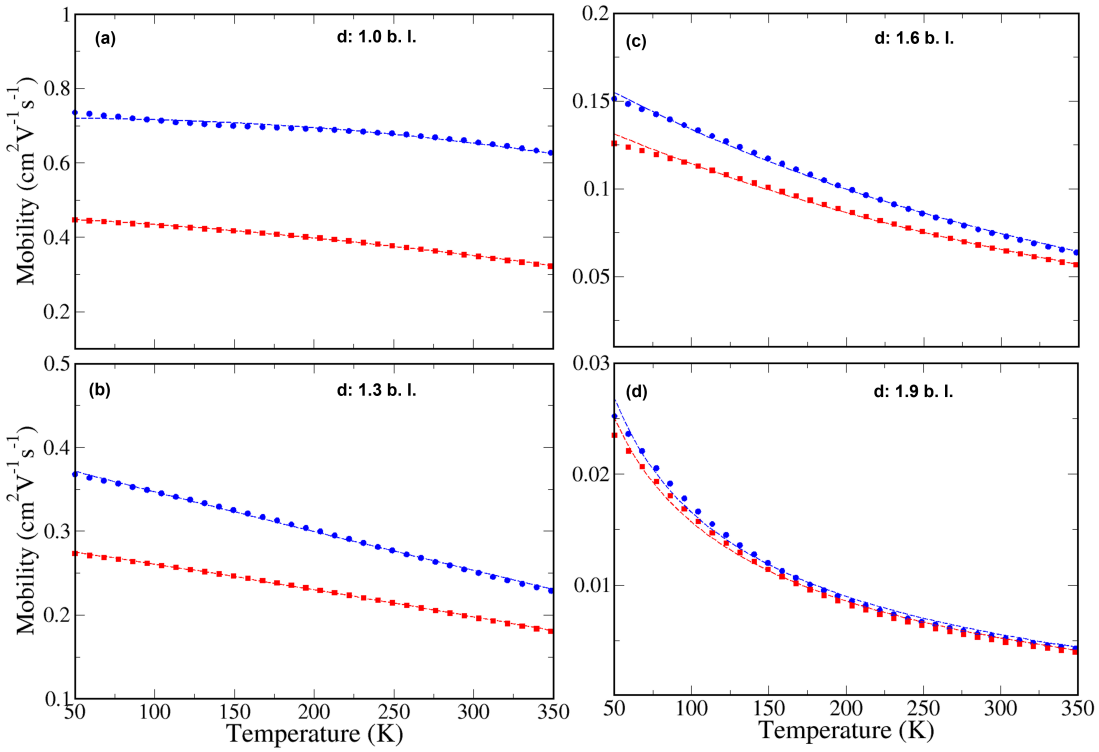

Figure 5.5: Electron mobility as a function of temperature for InP QD films where the QDs are separated by (a) 1, (b) 1.3, (c) 1.6 and (d) 1.9 b.l. The blue circles and red squares represent the two eigenvalues of the mobility tensor. The blue and red dashed lines are the respective fittings.

In general, InP QDs commonly synthesized in the lab suffer from poor surface quality and surface passivation problems, similarly to CdS QDs [233]. Experimental results on InP QD films were recently reported [234] showing that films based on InP QDs exhibit surface traps problems, leading to weak emission and reduced electron mobility (0.035 cm^{2}V^{-1}s^{-1}). It was found that the addition of Zn during the synthesis process leads to the elimination of those traps, forming InZnP QD films with even lower mobility (as the Zn:In ratio is increased, the mobility is reduced). The observed mobility for InP QD films is lower compared to PbSe[235] ($\sim$ 0.1-1 cm^{2}V^{-1}s^{-1}) and it is similar to PbS [236] ($\sim$ 10^{-3}-10^{-2} cm^{2}V^{-1}s^{-1}) QD films, but an order of magnitude lower compared to CdSe [237] QD films with similar treatments.

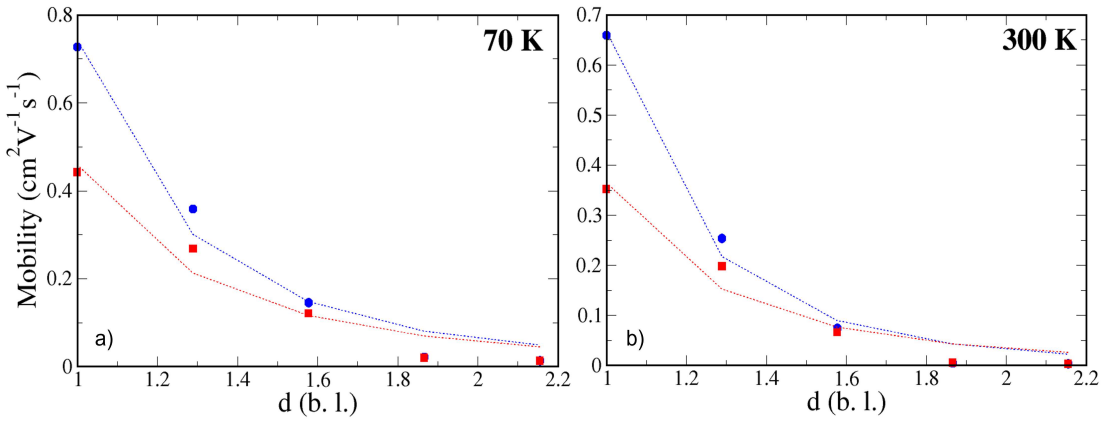

Figure 5.6: Mobility as a function of dot separation for (a) 70 K and (b) 300 K for InP QD films. The blue circles and red squares represent the mobility tensor eigenvalues. The blue and red dashed lines are the respective fittings.

Our findings show that InP QD films, when passivated properly[238], can exhibit carrier mobilities of the order of 0.5-0.7 $cm^2V^{-1}s^{-1}$ at room temperature. Recently, Crisp et al. [239] synthesized InP QD films deposited with crystalline ZnO films, yielding carrier mobilities of $\sim$ 4 $cm^2V^{-1}s^{-1}$ and charge separation between QDs and ZnO. Their films were, however, infilled and overcoated by ZnO films, which, acting as an electron extraction layer, greatly improved both the carrier mobility and their lifetime. In another experiment [228] a $\sim$ 96% decrease in mobility (from 1.9 $cm^2V^{-1}s^{-1}$ to 0.07 $cm^2V^{-1}s^{-1}$), attributed to surface traps and non-ideal passivation was observed when replacing As with P. We show that a $\sim$ 60% decrease is expected even in the case of ideally passivated QDs. The sizes of their samples were 4.8 nm $\pm$ 0.5 nm for InAs and 3.8 nm $\pm$ 0.4 nm for InP QDs, about three times larger compared to our QDs. QDs with larger size in the array lead to lower mobility values.

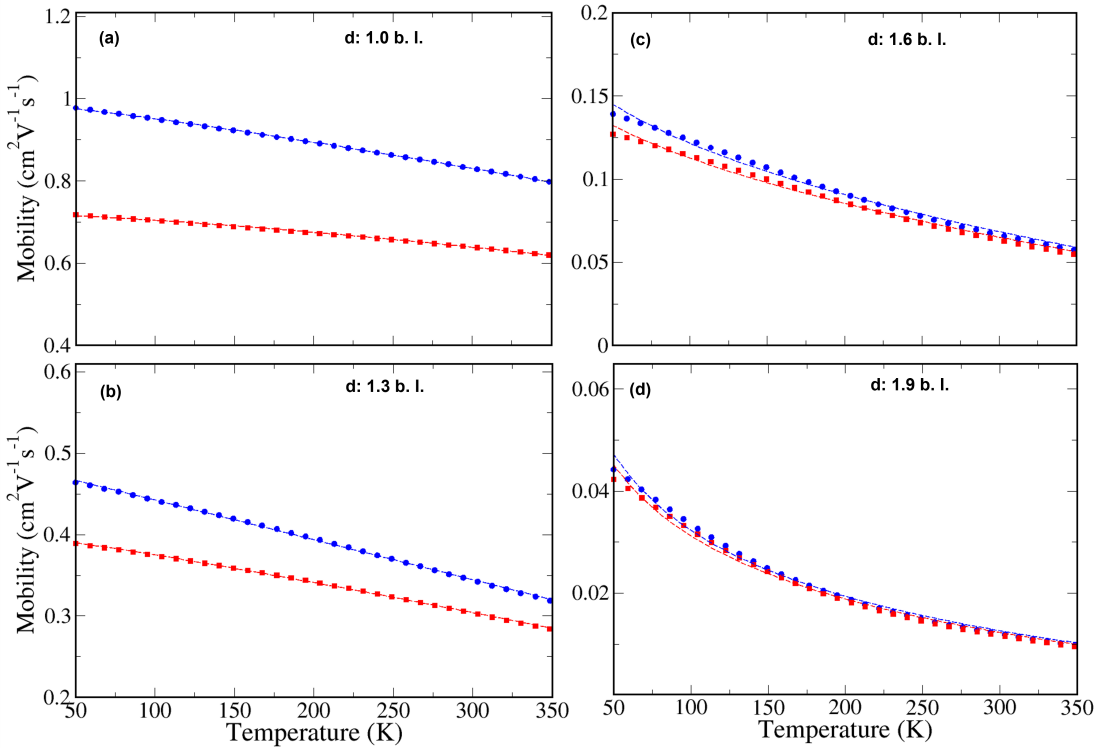

Figure 5.7: Electron mobility as a function of temperature for InSb QD films where the QDs are separated by (a) 1, (b) 1.3, (c) 1.6 and (d) 1.9 b.l. The blue circles and red squares represent the two eigenvalues of the mobility tensor. The blue and red dashed lines are the respective fittings.

InSb has the highest carrier mobility in the bulk among the rest of the In-based materials considered here [240], however, the electron mobility at the nanoscale is similar to the mobility found in InAs QDs. The variation of the mobility with increasing temperature and interdot separation for InSb films is presented in Fig. 5.7 and 5.8. Specifically, we calculate a mobility of ~ 0.82 cm^{2}V^{-1}s^{-1} at T = 300 K. We see that InSb lies between InAs and InP in the hierarchy of higher-to-lower mobility. The behavior of InSb QD films is very similar to the corresponding InAs films described above. Unfortunately, as, to the best of our knowledge, there are no existing experimental or theoretical studies on the transport properties of InSb QD films we could find no benchmark with which to compare our results.

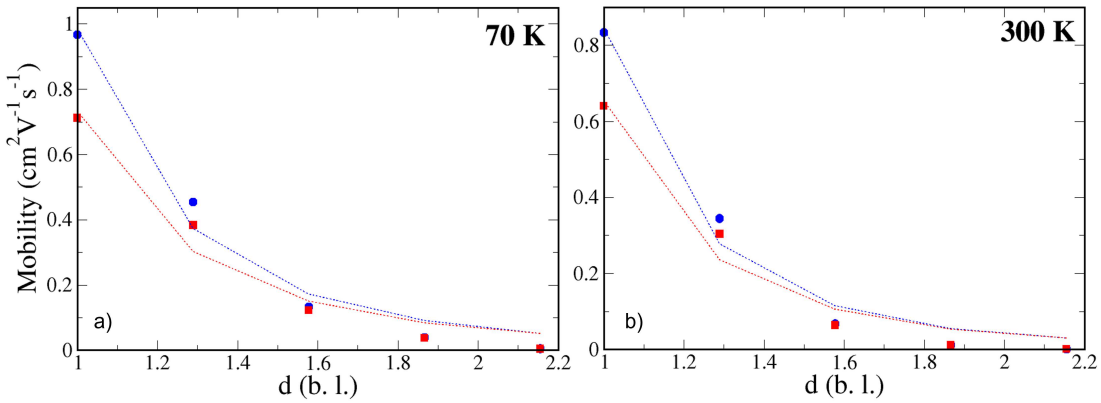

Figure 5.8: Mobility as a function of dot separation for (a) 70 K and (b) 300 K for InSb QD films. The blue circles and red squares represent the mobility tensor eigenvalues. The blue and red dashed lines are the respective fittings.

5.3 Ga-based QD films

Having considered In-based QD films with different anions, we then proceeded to replace the cation, obtaining GaSb, a non-toxic nanomaterial studied before [71]. Interestingly, we find that the mobility becomes about three times smaller compared to InSb. Specifically, the mobility drops from ~ 0.84 cm^{2}V^{-1}s^{-1} to ~ 0.28 cm^{2}V^{-1}s^{-1} for $d = 1$ b.l. at T = 300 K, as shown in Fig. 5.9.

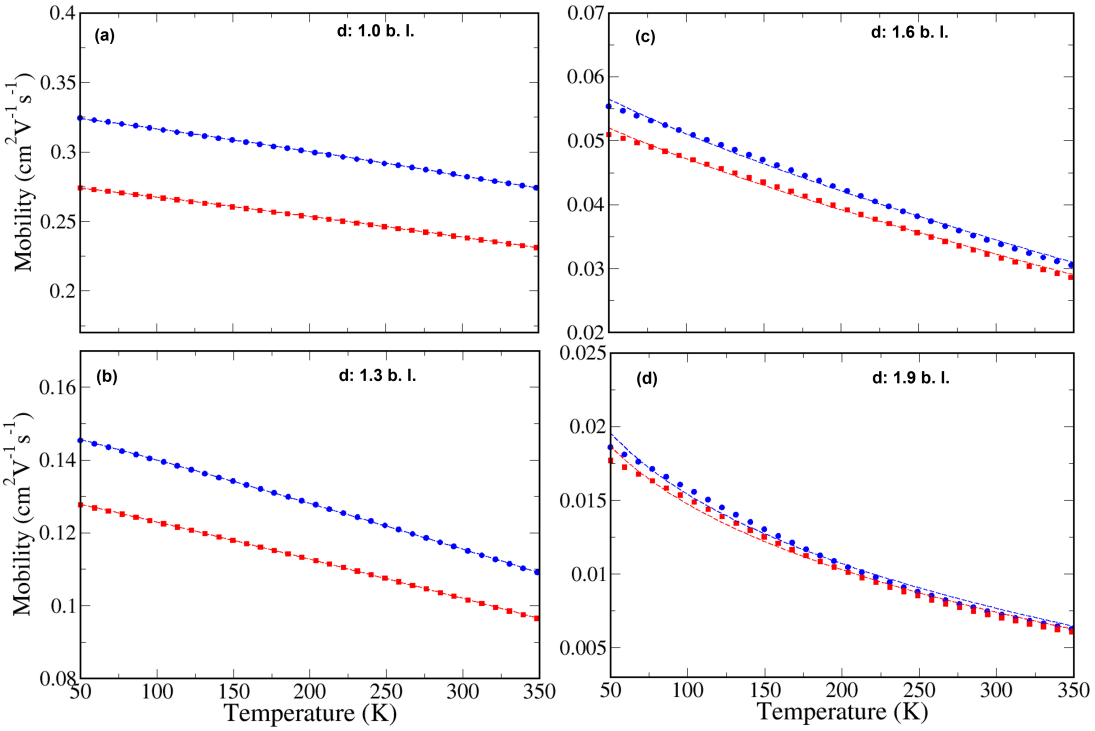

Figure 5.9: Electron mobility as a function of temperature for GaSb QD films where the QDs are separated by (a) 1, (b) 1.3, (c) 1.6 and (d) 1.9 b.l. The blue circles and red squares represent the two eigenvalues of the mobility tensor. The blue and red dashed lines are the respective fittings.

We also find that the two eigenvalues for the calculated mobility for the smallest separation considered here are closer, compared to the other materials. This is shown in Fig. 5.10 and it is attributed to the isotropic nature of its lowermost miniband structure around Γ, as illustrated in the 2D miniband representation of Fig. 5.1 (a) for $d = 1$ b.l. and in a top-view miniband representation of Fig. 5.11. The latter shows clearly that the lowermost miniband of GaSb QD films for $d = 1$ b.l. has an almost perfect circular shape around the miniband minimum while InP miniband is the most anisotropic.

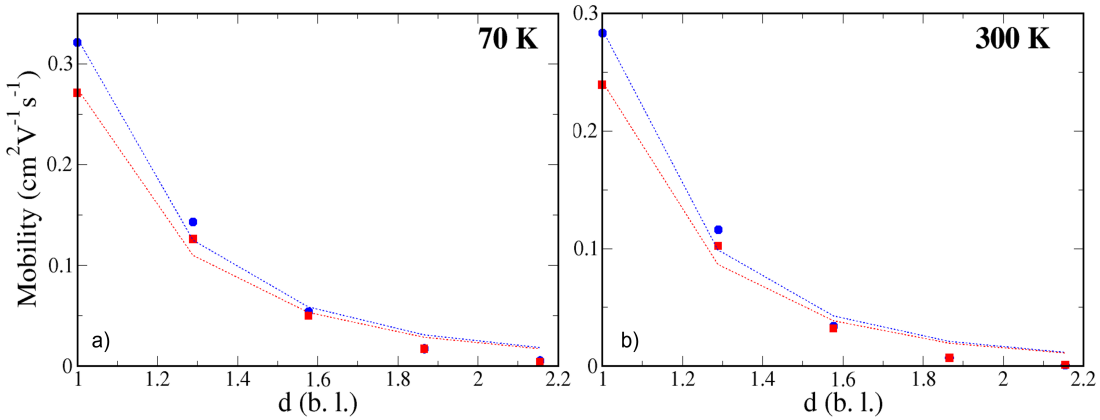

Figure 5.10: Mobility as a function of dot separation for (a) 70 K and (b) 300 K for GaSb QD films. The blue circles and red squares represent the mobility tensor eigenvalues. The blue and red dashed lines are the respective fittings.

The miniband curvature around the minimum, where most of the carriers are found, influences the mobility eigenvalues. We find that the change in the cation atom implies a smaller wave function overlap between neighbouring QDs compared to the In-based materials, yielding the lowest average flight times of $(5.14\pm2.06)\times10^{-16}$ s as shown in Table 5.1. These flight times are lower than flight times originating from phonon scattering in bulk semiconductors, in correspondence with the different mobilities calculated here. Nevertheless, flight times in the order of the ones found in this study have been recently reported in other studies [241].

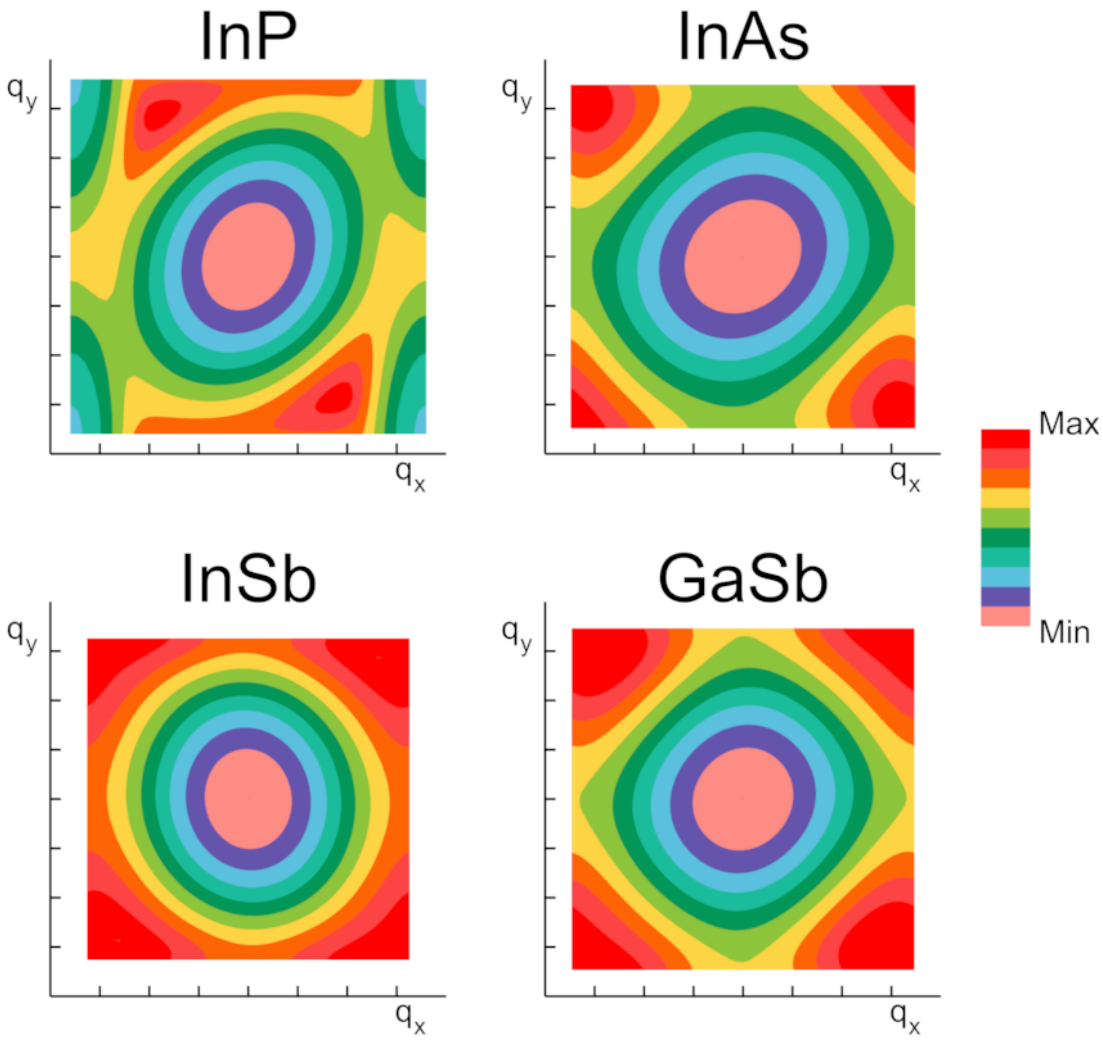

Figure 5.11: Top-view representation in reciprocal space for the lowermost conduction miniband for all materials considered in this study. The different colours show the energy of each miniband starting from the lowest (pink) to the highest (red) energy.

Comparing the miniband representations for each material it is evident that In-based QD films have a different behavior compared to GaSb. To fully understand the origins of this difference we analyzed the perturbation ΔV of the QD potential due to impurities in the film (see Eq. 5.1). We found the perturbation in GaSb has different features than In-based materials, resulting in different typical values of Γ (in Eq. 5.1), the transition rate between the initial (i) and final (f) state after scattering.

Material	Average Flight Time (s)
InAs	$(2.24\pm0.56)\times10^{-15}$
InP	$(2.33\pm1.66)\times10^{-15}$
InSb	$(1.90\pm0.79)\times10^{-15}$
GaSb	$(5.14\pm2.06)\times10^{-16}$
InAs (inv)	$(3.63\pm0.86)\times10^{-15}$

Table 5.1: Average flight times for all materials considered here (error intervals included). The error interval corresponds to the flight time's standard deviation.

The calculation of the mobility includes contributions from both the lowermost miniband width (that is linked to the effective mass) and the flight time of the carriers during their scattering (that is linked to the typical values of Γ in Eq. 5.1). We find that GaSb QD films, even though they have the highest miniband width for nearly all the separations considered here, exhibit the lowest average flight times (see Fig. 5.12). In order to achieve high carrier mobilities a combination of both large miniband widths and high flight times is required. For In-based QD films, the flight times are similar, therefore it is the miniband width that determines the mobility: films of InAs QDs have the largest miniband width among the In-based materials, thus the highest mobility followed by InSb and InP, reflecting the order of decreasing miniband width. On the other hand, GaSb QD films have a miniband width comparable with InAs QD films and larger than InSb QD films at $d = 1$ b.l., however the flight times for this material are $\sim$ 4 times lower compared to InSb QD films, yielding the smallest mobility of all (around three times smaller compared to InSb QD films).

As an interdot separation of 1 b.l. may be difficult to achieve in some experimental films, we calculated the variation in the miniband width with increasing d, shown in Fig. 5.17 (in the Conclusions section). The miniband width decreases with increasing d due to the weaker wave function overlap between the QDs. The same is true for the flight times. Consequently, mobilities calculated here for $d = 1$ b.l. represent an upper limit for real, lab-synthesized QD films. Since to the best of our knowledge, there are not any experimental characterizations of the transport properties of GaSb QD films, with this theoretical study we provide the first insights into the transport properties of this material.

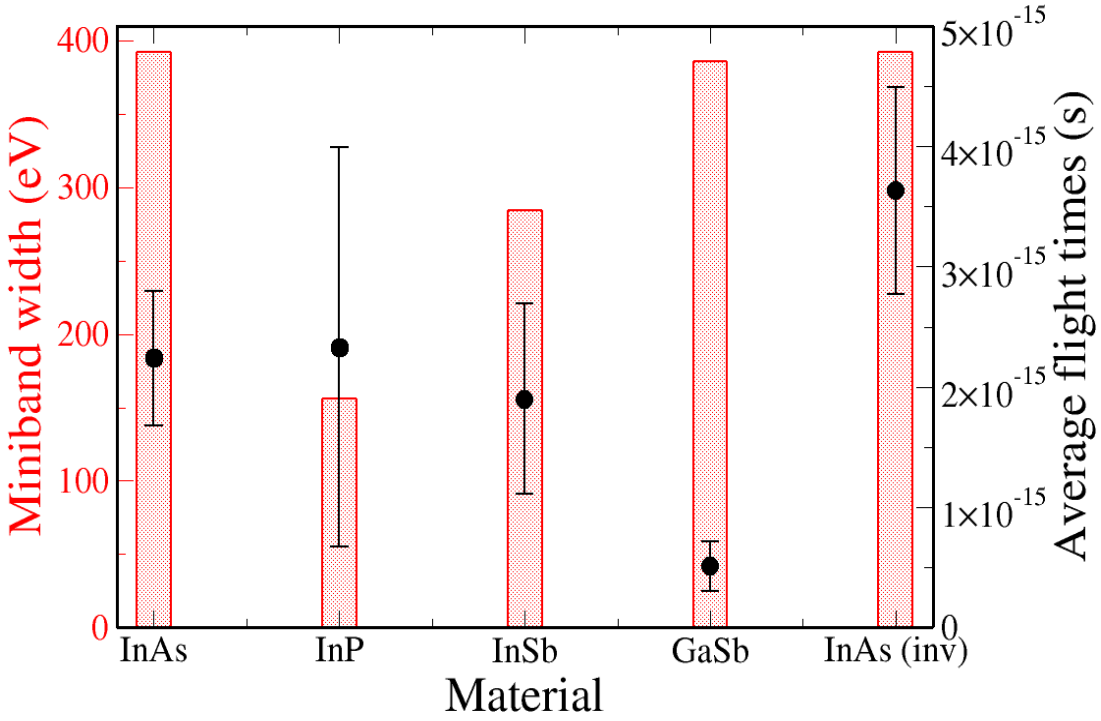

Figure 5.12: Lowermost miniband width and corresponding average flight times for $d = 1$ b.l., for each material. The average flight time has been calculated by averaging the flight times of a sampling of 51 × 51 initial states in the Brillouin zone. The error interval corresponds to the flight time's standard deviation.

5.4 Stoichiometry effect

Together with the material, the stoichiometry of the QDs is also a vital parameter to take into consideration. We calculated the transport properties of InAs QD films (we chose the material with the highest mobility), using impurity dots with the same number of atoms but with inverted stoichiometry (and thus an anion-rich surface like the periodic dots). In this case we find that the resulting mobility at room temperature is increased from ~ 0.85 cm^{2}V^{-1}s^{-1} to ~ 1.42 cm^{2}V^{-1}s^{-1} for a separation of 1 b.l., as shown in Fig. 5.13 and Fig. 5.14.

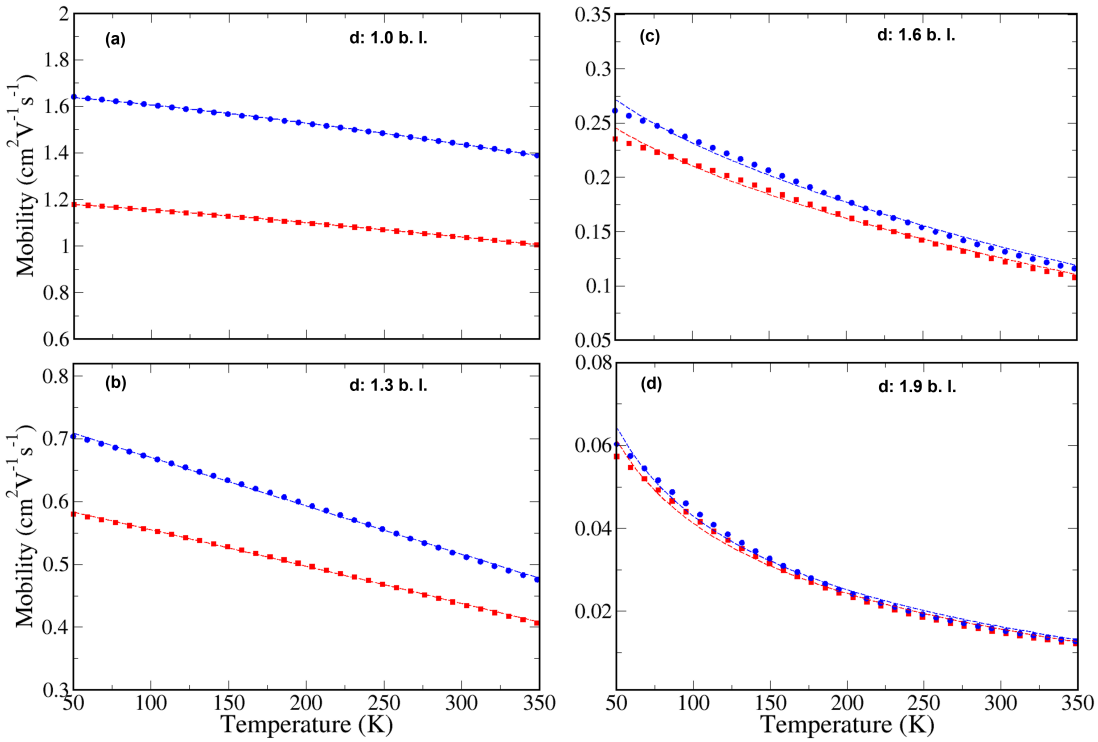

Figure 5.13: Electron mobility as a function of temperature for InAs QD films with stoichiometry-inverted impurity dot where the QDs are separated by (a) 1, (b) 1.3, (c) 1.6 and (d) 1.9 b.l. The blue circles and red squares represent the two eigenvalues of the mobility tensor. The blue and red dashed lines are the respective fittings.

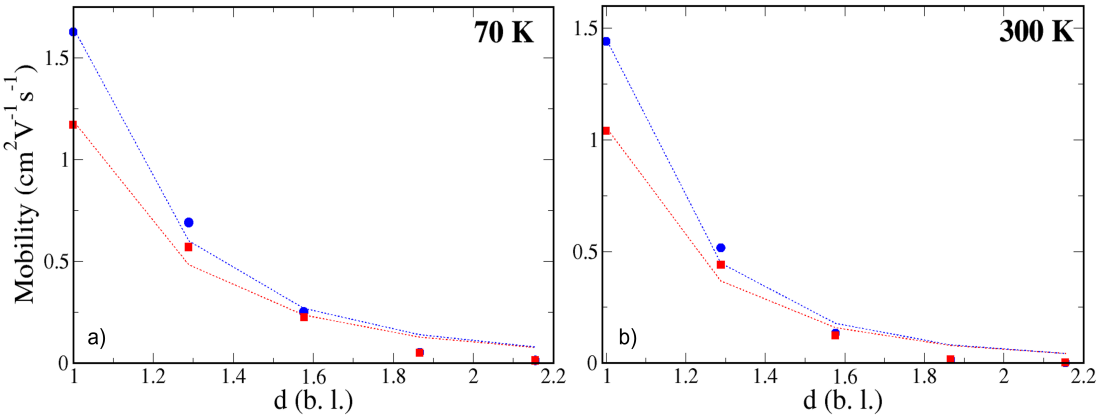

Figure 5.14: Mobility as a function of dot separation for (a) 70 K and (b) 300 K for InAs QD films with stoichiometry-inverted impurity dot. The blue circles and red squares represent the mobility tensor eigenvalues. The blue and red dashed lines are the respective fittings.

The mobility for this system is comparable with that observed in $CsPbBr_3$ perovskite QD films [242] (2 $cm^2V^{-1}s^{-1}$) and an order of magnitude higher compared to conventional PbS and PbSe QD films [230]. This can be attributed to the increased overlap between the wavefunctions of neighbouring dots and to the longer flight times of the carriers that determine the mobility. Indeed, as there is no effect of the impurity dot on the miniband structure in first-order perturbation theory, the resulting minibands for this case are the same as in the case of InAs QD films with anion-rich periodic dots and cation-rich impurities. Consequently, we find that the increase in mobility obtained inverting the stoichiometry of the impurity dot is due to an increase in the flight times, as shown in Fig. 5.12 (where the miniband width is also shown for each material, along with the corresponding flight times for $d = 1$ b.l.). The resulting mobility is higher compared to the CdSe (zinc blende) QD films that were modeled previously [231, 243, 69, 244].

The relation between this width and the interdot separation is illustrated in the inset of Fig. 5.17, where we show that as the interdot separation is increased, the miniband width is reduced due to the decrease in the wave function overlaps. In our case, the mobility and the miniband width have both a decaying trend with increasing interdot separation. The deviation from the expected trend in

the width at the lowest separation for InP and InSb is due to the nature of their miniband structure (see Fig. 5.1), where the lowermost miniband is very close to the second conduction eigenstate. As a consequence, the lowest conduction miniband reaches the lower point in energy of the following miniband, which blocks the expected expansion of the lowermost miniband width.

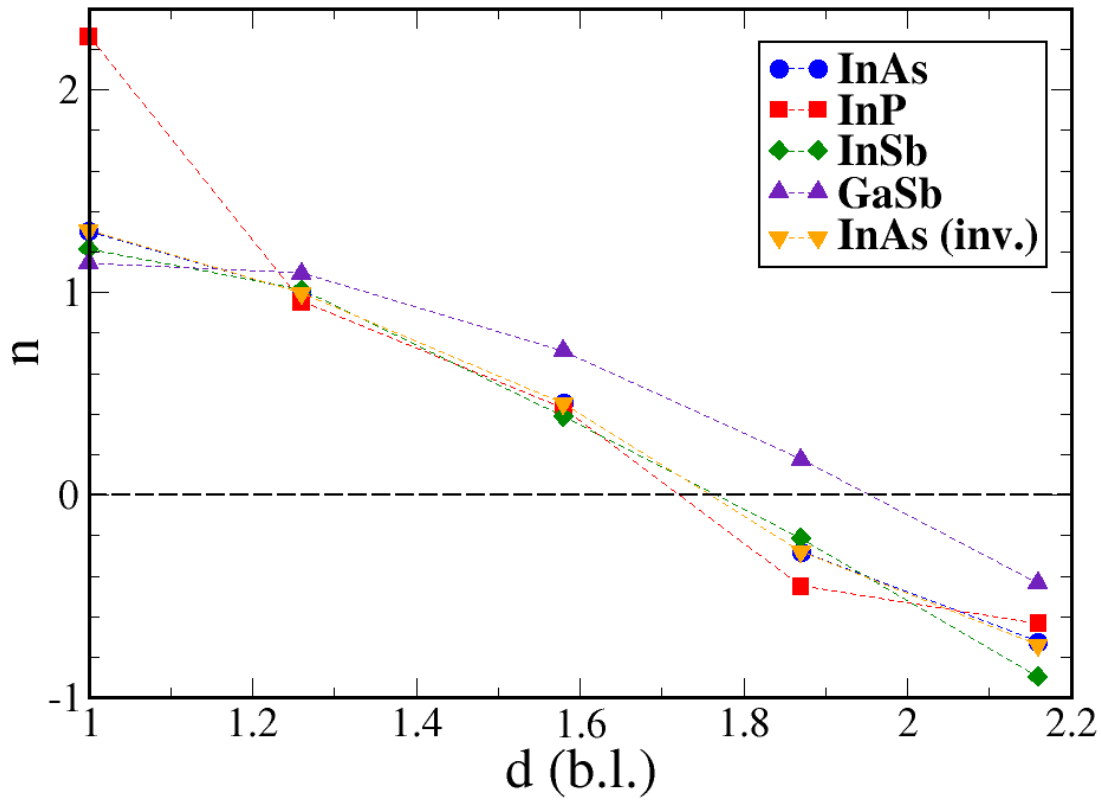

Figure 5.15: Rate of mobility reduction with increasing temperature (n) vs d according to the fitting of $\mu = A + BT^n$.

In order to provide a more quantitative estimate of the mobility dependence on temperature and interdot separation, we fitted our results with a power-law $\mu = A + Bx^n$ (where $x = T, d$). Table B.1 (see Appendix B) contains all the parameter values extracted from the fit to our temperature-dependent results. Parameter n indicates how the temperature affects the mobility. Depending on the interdot separation, we find two separate behaviours: $n > 0$ for dense dot arrays, and $n < 0$ for $d \sim 2$ b.l. Parameter A shows the mobility value at

T = 0 K (for $n > 0$) and T $\rightarrow \infty$ (for $n < 0$). Parameter B is found to always have the opposite sign compared to n. For $n > 0$, the higher the value of B (negative value) the larger the variation of mobility with increasing T. For $n < 0$, the higher the value of B (positive) the smoother the variation is.

The temperature effect on the mobility is an important parameter for devices as higher operating temperatures lead to a significant reduction of mobility. Consequently, the goal is to find materials that combine high mobilities and a 'resilient' behaviour to high operating temperatures. We predict that InP QD films should exhibit the slowest mobility reduction rate with increasing temperature at the smallest separation, as shown in Fig. 5.15. Although we find that n in this case has the largest (more positive) value compared to the other materials, meaning that the mobility (μ) should be affected most with increasing temperature (since $\mu \propto T^n$), this is not the case as the value of B is the smallest leading to the conclusion that the decay rate is the slowest. The value of n becomes negative at d=1.9 b.l. for all In-based QD films considered here, meaning that as the QDs in the array are placed even further apart the mobility is reduced at a higher rate. On the other hand, the behaviour of GaSb QD films is different: even though the decay rate is the fastest at the smallest separation, as d is increased the mobility is affected less with increasing temperature compared to the In-based materials. Specifically, at $d = 1.9$ b.l. GaSb is the only material to keep a positive value for n. This indicates that for GaSb QD films, even though the lowest mobility is predicted, a smaller mobility reduction rate for $1 < d < 2.2$ b.l. is found.

To investigate the effect of interdot separation we used a similar expression $\mu = C/d^m$. The values of the extracted fitting parameters are shown in Table 5.2. Parameters C and m have a similar effect as B and n in the previous analysis: the larger their value the larger the dependence of the mobility to increasing d.

We find that at T = 70 K as m has the lowest value, InP QD films are the least affected by the increase of d, as shown in Fig. 5.16. In addition, the value of C is the smallest among the In-based materials, suggesting that InP QD films would perform well at low operating temperatures, being less sensitive to the interdot separation which, in realistic systems, could easily exceed 1b.l. On the other hand, GaSb QD films exhibit the best behaviour at higher temperatures

T (K)	**70**		**300**	
	μ_1	μ_2	μ_1	μ_2
InAs				
C	1.0229	0.7406	0.9010	0.6547
m	3.9686	3.5647	4.6386	4.1768
InP				
C	0.7414	0.4583	0.6655	0.3633
m	3.5512	3.0216	4.4069	3.4410
InSb				
C	0.9843	0.7309	0.8443	0.6530
m	3.8291	3.4715	4.3738	4.0042
GaSb				
C	0.3251	0.2749	0.2863	0.2421
m	3.7654	3.6176	4.1955	4.0501
InAs(inv)				
C	1.6461	1.1908	1.4515	1.0541
m	3.9681	3.5696	4.6314	4.1708

Table 5.2: Fitting parameters C and m extracted from the fitting of our result to the function $\mu = C/d^m$ at T = 70 K and 300 K for both mobility eigenvalues and all materials considered.

(300 K). Finally, of all materials considered here, InAs QD films are influenced the most by the increase in d at both temperatures.

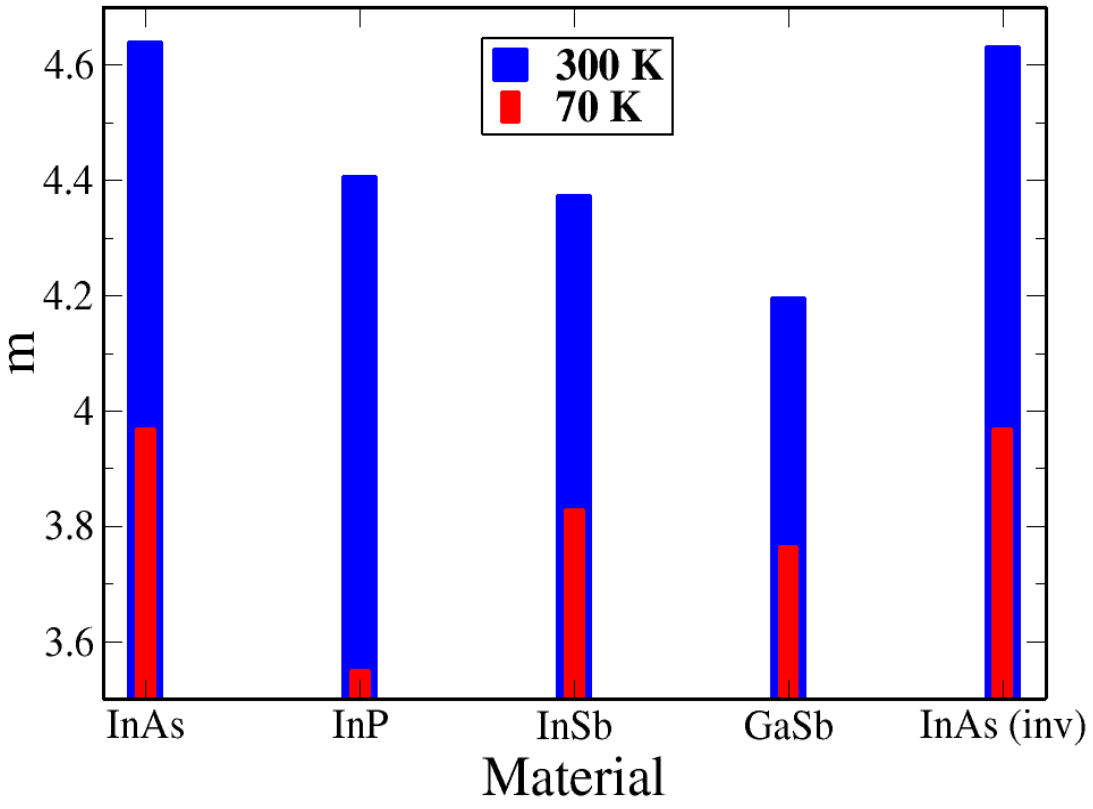

Figure 5.16: Rate of mobility reduction with increasing d (m) at T = 70 K (red) and 300 K (blue), for each material according to the fitting of $\mu = C/d^m$.

5.5 Conclusions

We calculated the transport properties of promising environmentally friendly QD films for replacing their currently used toxic counterparts (e.g. CdSe, PbSe, PbS) in realistic QD films, following a tight-binding model based on an atomistic approach. We find that (i) as the temperature of the film is increased, the mobility decreases, (ii) this reduction rate changes from $\sim$ linear ($n > 0$) to $\sim T^n$ ($n < 0$) as the interdot separation is increased, and (iii) the mobility for a specific temperature is reduced as the separation is increased due to the decreased overlap

between the electron wavefunctions, resulting in reduced miniband widths, flight times and thus mobility values. This is predicted for all materials considered here.

We predict that InAs films exhibit the highest mobility among the rest of In-based QDs, even higher compared to predictions for zinc blende CdSe and to experimental Pb-based systems, making InAs QD films an ideal heavy-metal-free alternative. We see that replacing As with Sb and then with P leads to small changes in the mobility while replacing In with Ga results in a significant decrease of the mobility. Specifically, we show that, the mobilities of ideally passivated InP QD films could be an order of magnitude larger compared to experiment (where the problematic passivation of real InP QDs prevents efficient transport). A quantitative investigation was carried out by applying a theoretical fitting to our results showing that InP QD films are the most 'resilient' to increasing temperature at $d = 1$ b.l. and to increasing d at T = 70K. We conclude that InP QD films be can a good candidate for replacing currently used toxic materials such as PbS. We also show that the mobility of GaSb QD films, is about three times smaller compared to InSb films, even though they have larger miniband width with increasing interdot separation. This is attributed to the smallest flight times (almost four times smaller compared to InSb). Additionally, the two eigenvalues of the mobility tensor calculated for this material are very close in contrast with the other materials due to the isotropic nature of the lowermost miniband, while an anisotropic formation of the miniband structure leads to a larger difference between the mobility eigenvalues. This could affect the performance of realistic systems as an isotropic miniband would imply smaller difference between the two mobility eigenvalues, meaning that no matter in what direction the contacts are placed on the film the observed mobility would be approximately the same. An anisotropic miniband would lead to a larger difference between the mobility eigenvalues. As a result the measured mobilities would depend on the direction along the film at which the contacts are positioned. Finally, inverting the stoichiometry of the impurity dot in InAs films leads to a significant increase of the carrier flight times and thus mobility, leading to the conclusion that the stoichiometry plays an important role in band-like transport as it can lead to a dramatic increase in both the wave function overlap between the QDs in the array and the flight

times. This suggests that a QD film made of QDs with similar surface composition could yield higher mobilities. Our calculated mobilities for InAs QD films exhibit a similar trend with increasing temperature as recently observed in molecular metal-chalcogenide-capped InAs QD films, while in the other cases (InSb, InP and GaSb) we provide the first insights into the band-like transport in QD films made of these materials.

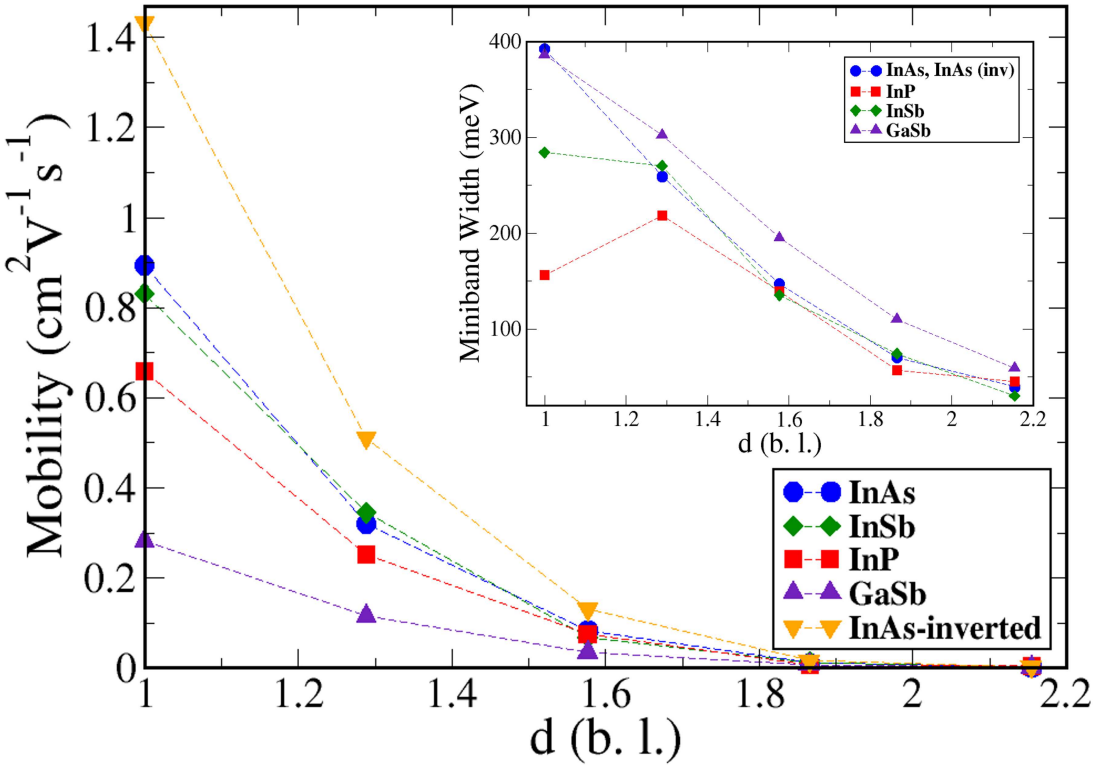

Figure 5.17: Comparison of calculated mobility (μ_1) as a function of d between InAs (blue), InP (red), InSb (green), GaSb (purple) and InAs with stoichiometry-inverted impurity dot (orange). The inset shows the lowermost miniband width as a function of d for all materials considered here (both InAs cases have the same miniband width).

Chapter 6

Spherical GaP NCs

This chapter includes our findings on GaP spherical NCs. The electronic and optical properties for this material were calculated by using the SEMP, as explained in Chapter 2. GaP is an indirect bandgap, environmentally friendly nanomaterial, that has been studied for over 30 years at both experimental and theoretical levels. However, scientists have not provided satisfactory explanations on the optical properties of GaP at the nanoscale, especially when it comes to the determination of the non-radiative processes and the respective lifetimes. This aspect is particularly important in NCs, since in many cases fast Auger Recombination lifetimes dominate over the radiative recombination, limiting the application of such structures. Although our theoretical investigation is at an initial stage and it is to be completed, we calculated the electronic structure, absorption, and emission spectra of small GaP NCs, with radii ranging between 8 Å and 30 Å. We considered trap-free systems by applying an ideal passivation set for our NCs, eliminating any surface traps. In our investigation, we considered various NCs in terms of composition and stoichiometry. Our results on the optical properties were compared with other In-based (InP) and Ga-based (GaSb) materials, showing how changing the NC composition can affect the optical properties. In this way, we could identify the effects of cation or anion replacements and how important the NC composition is. Subsequently, the radiative and Auger recombination lifetimes were calculated, suggesting that GaP NCs have slow radiative lifetimes, even slower compared to InP and GaSb. This gives rise to non-radiative

recombination that was found to be faster compared to InP NCs. Thus the non-radiative dominates in the recombination process. The averaged radiative and non-radiative lifetimes were calculated as described in Chapter 2.

6.1 Introduction

Due to their unprecedented and confinement-dependent electronic and optical properties at the nanoscale, semiconductor nanocrystals (NCs) are considered promising building blocks for a wide range of applications. With the constant technological advancement and commercialization of products, the search for non-toxic material alternatives is larger than ever. Gallium Phosphide (GaP) emerges to be an ideal candidate for a wide range of applications. GaP is a III-V compound, widely studied semiconducting material for more than three decades, widely used in UV-photodetection [245, 246, 247], multi-junction solar cells [248, 249, 250] and piezo-electric [251] applications, while it is being considered as a CMOS-compatible material and promising for photocatalysis [252]. GaP has a ZB crystal structure with an indirect bandgap in the bulk. Several theoretical [253, 254] and many experimental [255, 256, 257, 258, 259, 260, 261, 245] studies throughout the years have reported results on the optical properties of GaP NCs. However, the radiative and non-radiative processes in such systems were not explored. With this motive, we initiated this work intending to calculate the radiative and Auger recombination lifetimes in GaP NCs with a ZB crystal structure, showing the difference compared to other environmentally friendly NCs. As part of this investigation, the NC composition was also taken into consideration by modelling NCs based on another cation (InP) and another anion (GaSb), giving an overview of a comparison between environmentally friendly nanomaterials. This investigation, however, is still to be completed: aspects such as the Brillouin zone decomposition and charge density visualization are in our future tasks. Additionally, the calculation of the Auger recombination lifetimes for all the NC considered here along with the corresponding lifetimes in GaSb NCs would be of great importance for our research.

6.2 Electronic Structure of GaP NCs

The NCs considered here have radii ranging between 8 Å and 30 Å. Our NCs were properly passivated with an ideal passivation set eliminating any surface traps, which can be confirmed by the positioning of the CBM and VBM energies above and below the bulk values for CBM and VBM respectively, as shown in Fig. 6.1. These results are in agreement with previous theoretical [254] studies that show that GaP NCs exhibit a large bandgap, in the visible, near-UV range. The passivation parameters considered here are presented in detail in Table 6.1.

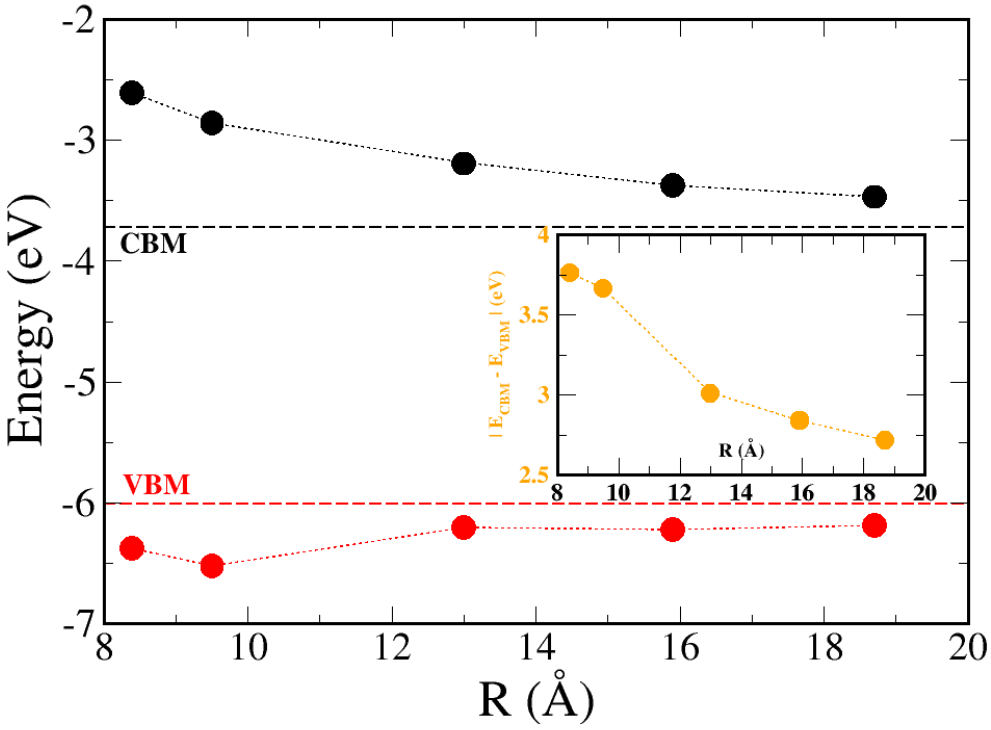

Figure 6.1: Calculated band edge energies as a function of NC size. The black lines represent the positions of CBM and the red lines of the VBM, respectively. The dashed horizontal lines show the band edges in bulk GaP. The inset illustrates the calculated bandgap energy difference $|E_{CBM} - E_{VBM}|$ as a function of NC size.

We see that the CBM has a smooth decay trend with increasing NC size while the VB experiences a not-so-smooth behaviour. This could be attributed to the confinement of charges in the VB.

	cation						anion					
	1 dangling bond			2 dangling bonds			1 dangling bond			2 dangling bonds		
	a	b	c	a	b	c	a	b	c	a	b	c
	0.50	0.50	0.70	0.5	0.15	0.25	-0.6	0.55	0.30	-0.8	0.30	0.20

Table 6.1: Passivation parameters used to passivate surface Ga and P atoms in this work.

As expected from the bulk bandgap, the single-particle gap of GaP NCs is the largest compared to InP and GaSb NCs. This is shown in Fig. 6.2. According to the energy dependence on increasing NC size, the Ga-based materials seem to have a larger dependence, meaning that they exhibit stronger quantum confinement at the nanoscale.

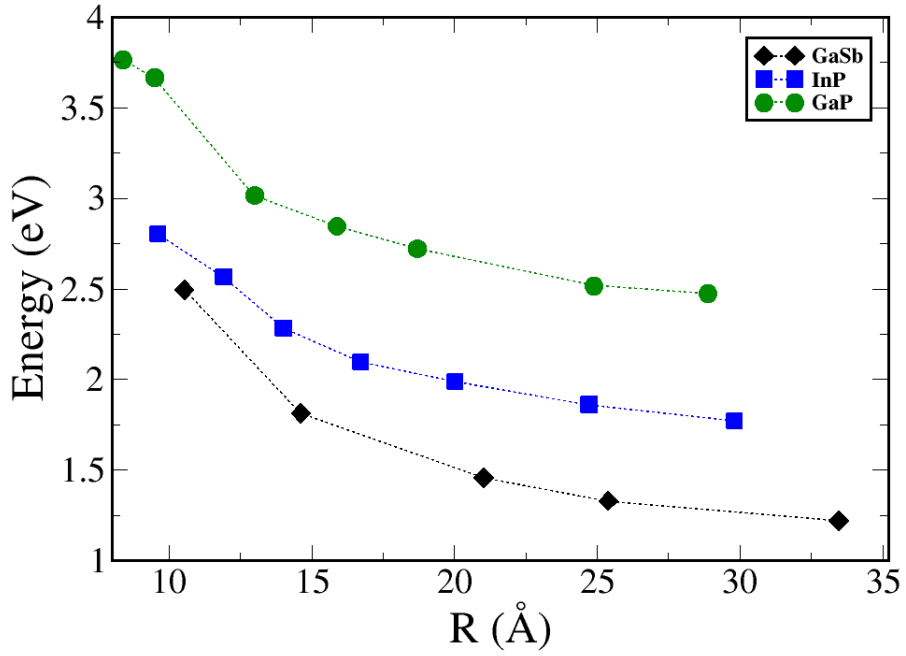

Figure 6.2: Single particle bandgap energy as a function of NC radius R for GaSb (black) InP (blue) and GaP (green).

6.3 Optical Properties of GaP NCs and comparison with other non-toxic NCs

After calculating the electronic structure and wavefunctions, the optical properties were calculated via a CI scheme.

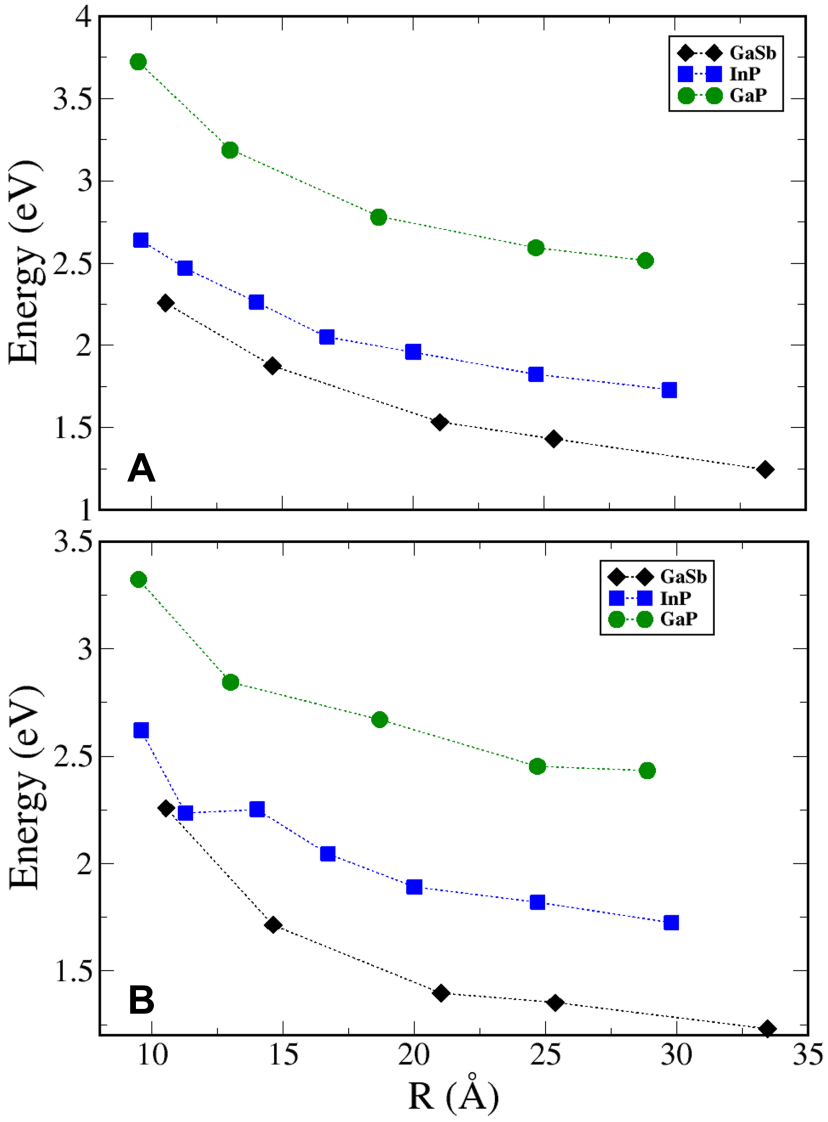

Figure 6.3: Absorption (A) and emission (B) spectra as a function of NC size. A comparison between GaP, InP and GaSb spherical NCs.

The excitonic picture comparison between these materials is shown in Fig. 6.3, where we find that the hierarchy in energy is consistent with the single-particle gap, from where the excitons originate. The excitonic energy decreases with increasing NC size. The sudden drop in emission energy for an InP NC with R = 12 Å originates from the absence of P atoms at the NC surface (explained in Chapter 4). Comparing the respective radiative recombination lifetimes between the three materials (shown in Fig. 6.4), we find that, GaP exhibit the longest lifetimes, followed by GaSb and InP. Although both GaP and GaSb have an indirect bandgap, the latter exhibit faster lifetimes (decreasing with increasing R) compared to the former (increasing with increasing R).

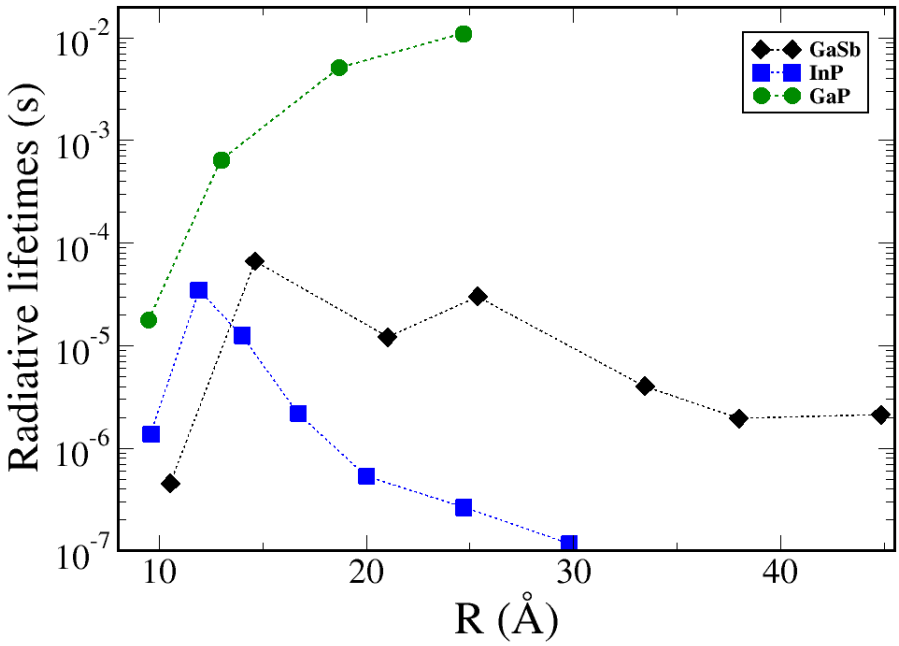

Figure 6.4: Radiative lifetimes as a function of NC radius. A comparison between GaP (green), InP (blue) and GaSb (black) spherical NCs.

This could be attributed to a better overlap between the CBM and VBM wavefunctions in real or reciprocal space. However, this investigation is in our

future plans. Both InP and GaSb have a decreasing trend (apart from the smallest QD considered) with increasing NC size, however, for GaP, the opposite is true.

Our results on the optical gap were compared with available experimental and theoretical studies, as illustrated in Fig. 6.5. A more detailed analysis will follow once we have more information about the origin of optical transitions, dipole matrix elements, and oscillation strengths.

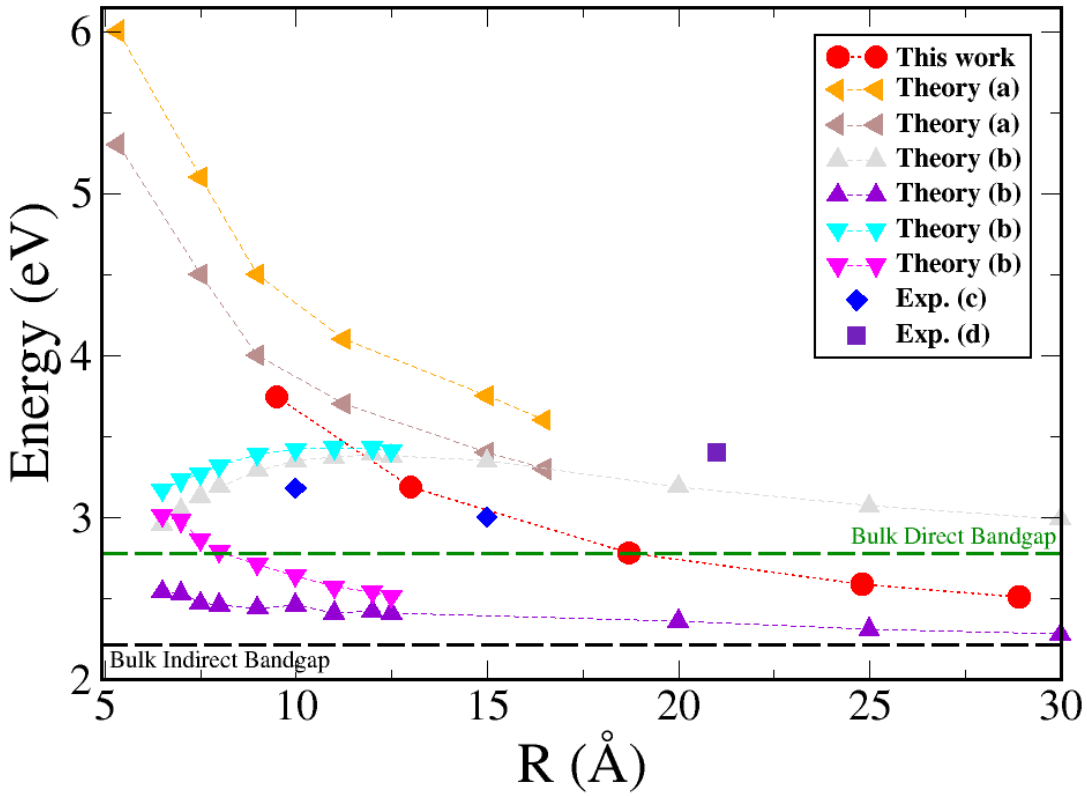

Figure 6.5: Absorption spectra: comparison of our results (red circles) with experimental and theoretical studies: (a) ref [262], (b) ref [253], (c) ref [261], (d) ref [245]. In (a) the orange triangles correspond to the DFT/B3LYP method and the brown triangles to the DFT/B3LYP/TDDFT method. In (b) the grey and purple triangles show the results based on decreasing cluster lattice constant while the cyan and pink triangles correspond to the calculations based on the bulk lattice constant.

Since there is currently no evidence, to our knowledge, regarding the Auger processes in GaP NCs, the non-radiative recombination was another important

aspect to look into. Our lifetimes were calculated based on the approach described in Chapter 2. We find that the Auger recombination lifetime for an InP NC with R = 12 Å is around 130 ps, while a GaP NC with R = 13 Å exhibits lifetimes around 53 ps, more than two times faster. Our results are shown in Fig. 6.6, in terms of Auger Constant, calculated as

$$C_{\mathrm{A}} = \frac{V_0^2}{(8\tau_{AR})} \tag{6.1}$$

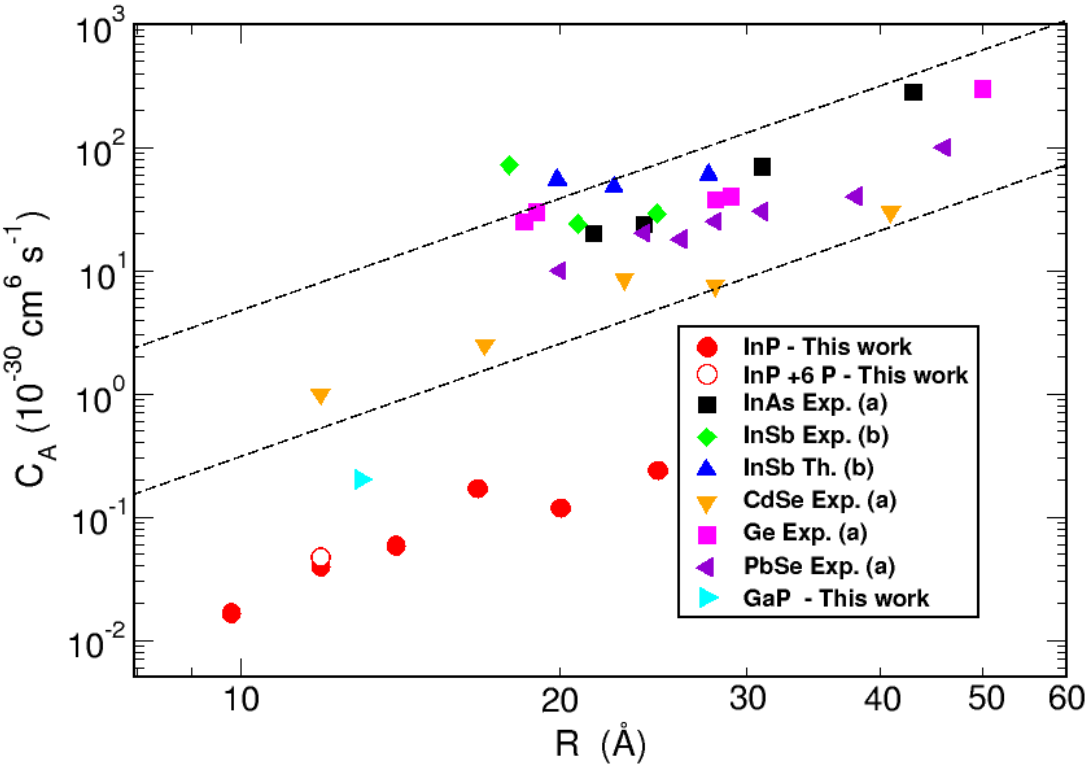

Figure 6.6: Auger constant as a function of NC radius: comparison with experiment: (a) ref [212], (b) ref [209]. The black dashed lines show the universal scaling window proposed by [212].

In this way, we can compare with other environmentally friendly or toxic nanomaterials. We find that GaP is classified outside the universal scaling window developed by [212], similarly with InP. The lifetimes of GaP NCs are faster compared to the latter but slower compared to CdSe, InSb, and PbSe. It was

previously shown that manipulating the NC surface, and thus the total surface electronegativity, it is possible to alter the wavefunction overlap in the reciprocal space, suppressing the Auger recombination, varying the radiative lifetimes and suppressing the PL self-absorption by reducing the Stokes' shift [41]. This was achieved previously in [71, 238], however, this prediction needs to be supported by further proof about GaP NCs. Ideally, this could lead to the selection between radiative or non-radiative recombination channels according to the application of interest, by simply manipulating the NC surface.

The AR lifetimes for the remaining of GaP NCs are still to be calculated and included in this figure. Additionally, the AR lifetimes for GaSb NCs will be calculated, an addition that will give new insights for this material and for Ga-based materials in general. Our investigation of the electronic structure and optical properties will be further expanded in the Brillouin zone decomposition in reciprocal space and charge density visualization in real space. This information can support our findings and predictions, providing a solid characterization of the unexplained properties behind GaP NCs.

6.4 Conclusions

In this chapter, a preliminary study on the calculations of the electronic and optical properties of GaP spherical NCs was presented. GaP, being a widely-used non-toxic nanomaterial, has kept the interest high for experimental groups throughout the years. With no previous calculations nor measurements on the radiative and non-radiative recombination lifetimes for this material, we aimed at filling this gap in the literature by comparing GaP with previously studied non-toxic materials such as InP and GaSb. In this way, the effect of changing the NC composition is also investigated (using different anions and cations in the NC composition). The comparison of the single-particle bandgap energies for these materials was presented. A similar comparison was shown for the absorption and emission energies along with the corresponding radiative lifetimes. The Auger lifetimes were calculated for a single GaP QD, indicating that the non-radiative recombination lifetimes follow the trend of other semiconductor materials. Furthermore, these lifetimes are found to be more than two times faster compared to

the ones calculated for an InP NC with similar size. This work is to be completed by calculating the Auger lifetimes for the rest of GaP NCs. Additionally, the calculation of the Auger lifetimes for GaSb NCs would complete the comparison between the three materials.

Chapter 7

Conclusions

7.1 Summary

We introduced semiconductor nanostructures indicating why they are interesting and the wide range of their applications. We then explained the basic principles of quantum physics that are relevant in such systems, namely, the quantum confinement effect based on the NC size, the energy quantization, and Coulomb interaction.

Chapter 2 discussed the theoretical framework behind the approaches followed in this research. Specifically, the state-of-the-art atomistic semiempirical pseudopotential method was described, and the steps required to calculate the electronic and optical properties of NCs explained: (1) the construction of the atomistic structure (geometry), essential for (2) the calculation of the total nanocrystal potential through a superposition of the screened atomic potentials; (3) the solution of the single-particle Schrödinger equation using the folded spectrum method, which provides the ability to calculate selected eigenstates close to any chosen reference energy, avoiding the calculation of the whole energy spectrum; (4) the inclusion of excitonic effects via the CI method. This procedure allows the calculation of the optical properties of isolated NC (such as absorption and emission spectra, radiative lifetimes, etc.). Finally, the tight-binding model that was used for the calculation of the transport properties in 2D QD films was presented.

Based on the approaches and techniques described in Chapter 2, we were able to perform our investigation in NCs made of various non-toxic materials, starting with GaSb. Specifically, the characterization of GaSb NCs was presented in Chapter 3. GaSb is an environmentally friendly nanomaterial not yet synthesized in colloidal form, with unique properties at the nanoscale, and, according to our findings, promising for a wide range of applications. In our theoretical characterization, we considered NCs with radii ranging between 11 Å, and 45 Å. Our investigation started with the calculation of the electronic structure and the energy-gap dependence on the NC size, showing that GaSb exhibit strong quantum confinement effects with decreasing NC radius. This, along with the closely spaced conduction band minima between Γ and L points in k-space and the difference in the respective effective masses, led us to predict a confinement-induced Γ-to-L transition in the CBM character, and thus a direct-to-indirect bandgap transition. This transition was predicted to occur at NCs with $R < 36$ Å. By providing a detailed analysis of the k-space composition and symmetry of the CB wave functions along with the evolution with size of Γ-, L- and X-derived states in the CB, we provided the first insights regarding the nature of absorption and emission spectral features, radiative lifetimes and Stokes' shifts. We showed that the emission of such NCs can be tuned throughout the visible spectrum, and is accompanied by large Stokes' shifts and long radiative lifetimes due to the indirect nature of the bandgap transition. We proposed that GaSb NCs, thanks to these properties, could be used in a wide range of applications, including photovoltaics and memory storage. We then focused on a particular application: photocatalysis. Specifically, we showed how GaSb NCs could be an ideal candidate for photocatalytic CO_2 reduction with water. Our findings were published in ACS Applied Materials & Interfaces.

The next non-toxic nanomaterial we investigated was InP, presented in Chapter 4. Even though InP NCs have been studied for the past two decades and are used in a variety of applications (especially optoelectronics), they still exhibit low photoluminescence quantum yield and broad emission. This is commonly attributed to the presence of surface traps due to poor surface passivation. In our theoretical characterization, however, we showed that, even with an ideally passivated surface, colloidal InP NCs can still exhibit low QY, depending on their surface

composition (i.e., to whether the surface is In- or P-rich). Specifically, we found that NCs with a P-rich surface exhibit faster radiative lifetimes, stronger emission and smaller Stokes's shifts compared to NCs with an In-rich surface. Visualizing the charge density in real space, we found that the confinement of the VBM plays an important role in the NC optical properties, resulting in low QY (when the hole exhibits poor confinement). It is worth mentioning here that, at the start of this investigation, we had to optimize the passivation parameters previously published, as they did not provide sufficient confinement for the VBM wave function. Additionally, calculation of the Auger recombination and Auger cooling lifetimes showed that they were unaffected by the NC surface stoichiometry. It followed that engineering the NC surface could lead to a variation of the radiative lifetimes by orders of magnitude, without changing the Auger recombination times. Thus, controlling the surface stoichiometry of InP NCs can increase the QY. This effect is found to be strong in InP NCs due to the electronic configuration of P atoms, that lacks d orbitals.

As an extension of our investigation into non-toxic NCs, and in collaboration with our colleagues in Granada, we modelled environmentally friendly 2D colloidal QD films made of In-based and Ga-based binary materials. This work was presented in Chapter 5, where we first calculated the electronic structure of individual dots using the atomistic SEPM, then, we applied the tight-binding model described in Chapter 2 to obtain the transport properties of the array. This approach yields results that are closer to experiment compared to the conventional tight-binding treatment. In this work we modelled band-like transport in QD films made of InAs, InSb, InP and GaSb, investigating them as possible replacements for their currently used toxic counterparts (Cd-based, Pb-based materials) in realistic systems. We found that InAs QD films exhibit the highest mobility among the rest, and even higher compared to previously modelled CdSe QD films, suggesting that InAs could be a potential alternative for CdSe. Investigating the effect of NC composition, we replaced As with Sb and then P, and found that the mobilities are similar. Interestingly, we showed that ideally passivated InP QD films yield mobilities an order of magnitude larger compared to experiment. However, replacing In with Ga, we found that the carrier mobility was reduced

(three times smaller compared to InSb QD films). We showed that, for all materials, the mobility decreased with increasing temperature and increasing interdot separation. In order to have a better picture of these effects, we performed a quantitative investigation showing that InP QD films are the most resilient to increasing temperature for the smallest interdot separation considered and to increasing interdot distance at low operating temperatures. These findings suggest that InP QD films are promising candidates for replacing PbS 2D QD arrays. We also found that, even though the miniband width of GaSb QD films was found to be larger with increasing interdot distance compared to InSb, the mobilities for the former were three times smaller compared to the latter. We attributed this behabviour to the (almost four times) smaller flight times compared to InSb QD films. Additionally, we found that the isotropic nature of the lowermost miniband in GaSb QD films resulted in very close mobility eigenvalues, which can affect the performance of realistic devices in terms of the direction of contact placement on the film and the observed mobility. Finally, the stoichiometry effect was investigated. Inverting the stoichiometry of the impurity dot in InAs QD films lead to an increased wave function overlap between neighbouring dots in the array and thus to higher flight times and carrier mobilities. We concluded that by engineering the QDs in a film to have all similar surface compositions it would be possible to obtain higher mobilities.

Having the incomplete optical properties of GaP NCs a motive, we decided to model this widely-used, non-toxic nanomaterial in order to calculate properties such as radiative and Auger recombination lifetimes that are still missing from the literature. We believe that this would be valuable information for existing experiments, as Auger recombination is known to compete with the radiative recombination in NCs, limiting their applications. Additionally, as we proved in our work so far, the NC composition cannot be neglected since it significantly affects the electronic structure and optical properties of NCs. In this regard, we calculated the radiative and non-radiative lifetimes in GaP NCs, comparing our results with other environmentally friendly NCs (InP and GaSb) that were previously studied. In this overview, we show that GaP NCs exhibit strong quantum confinement effects, just like GaSb. The corresponding radiative lifetimes for the former are very slow, slower than InP and even slower than GaSb (which also has

an indirect bandgap). Interestingly, the calculation of the non-radiative lifetimes showed that GaP NCs have around two times faster lifetimes compared to InP NCs, but, similarly with the latter, exceed the universal scaling window that was previously proposed for semiconductor NCs.

Introducing the potential of colloidal semiconductor NCs and the growing need of replacing the currently used toxic materials with non-toxic alternatives, the objective of this thesis was the investigation of such environmentally friendly materials and the characterization of their electronic and optical properties for being deployed in realistic technological applications. As a reflection to these expectations, the theoretical work presented here has addressed this issue in a high level: (i) a new nanomaterial (GaSb) has been explored and a characterization of its properties at the nanoscale was presented; (ii) new insights regarding the optical properties of InP NCs were provided. Current experimental results, that lacked satisfactory explanations were explained, paving the way for NC synthesis that emphasizes in the NC surface stoichiometry along with a promising alternative to toxic elements; (iii) Explored a new application of CQDs, the 2D CQDs films, where non-toxic QDs are predicted to be a potential replacement of their currently used toxic counterparts; and (iv) initiated an investigation regarding the optical properties of GaP NCs in a comparison with previously studied materials, indicating the effect of NC composition. The publication of our results, participation in conferences and the collaboration with the University of Granada provide a strong indication of the activities and achievements throughout this project.

7.2 Future Work

In this work we presented an investigation on both emerging and widely used environmentally friendly colloidal NCs, proposing them as potential alternatives for the currently dominant Cd- and Pb-based, toxic nanomaterials. Our findings provide new insights and supporting information to properties that were unexplored or lacked satisfactory explanation. However, if time permitted, this investigation could be expanded to cover a wider area of research, including new

materials with different compositions and shapes, promising for different applications. As a continuation of the investigation presented here, there are the following possible developments for future work:

Optical properties of GaP NCs

As to an extension to our ongoing investigation, we will calculate the Auger recombination for the rest of the GaP NCs, fulfilling the Auger Constant graph and thus have a clearer comparison. In this regard, the non-radiative recombination in GaSb will also be calculated as it will provide a more in-depth comparison with GaP and the other environmentally friendly nanomaterials. Additionally, the Brillouin zone decomposition in the reciprocal space along with the charge density visualization in real space can provide more evidence behind the electronic structure of such NCs. Finally, similarly with InP NCs, we are interested in investigating the NC surface effects and see whether similar effects are the case in GaP.

Tetrapod-shaped InP NCs

InP NCs were extensively studied in this work. As shown in this project, InP is a particularly interesting material that when passivated properly can yield good optical properties, beneficial for many applications. A possible extension of the research work presented in Chapter 4, based on very recent experimental reports of the synthesis of tetrapod InP NCs[263], would be the modelling of branched nanostructures, to provide the first theoretical characterization of the electronic and optical properties of tetrapod InP NCs which would be valuable to support and explain the recent experimental findings. This could pave the way for new applications, especially to replace the currently widely used (and studied) Cd-based tetrapods, and provide an alternative to the use of toxic materials, thus allowing an expansion of their commercialization.

Wurtzite InP NCs

Another interesting aspect in this area of research would be the generation of InP NCs with wurtzite (hexagonal) crystal structure and the calculation of the relative electronic and optical properties. The properties can then be compared

with the zincblende structure and identify possible differences attributed to the change of crystal structure. It would also be interesting to see whether the strong surface effect in ZB InP NCs (attributed to the P surface atoms) remain in this case. Very recently[264], WZ InP and GaP QDs were synthesized, paving the way for future research on these WZ nanomaterials.

Investigation of the transport properties of QD films based on other non-toxic materials

As a future task, we would consider the modelling of 2D QD films based on other environmentally friendly materials such as GaP and the comparison of the transport properties with other Ga-, Cd- and Pb-based QD films. Since there are no other theoretical nor experimental studies on such films, this could be potentially a new research field providing the first insights into the transport properties in GaP QD films. Effects such as the NC composition and stoichiometry would also be investigated. The non-toxic character of such films could classify them among the candidates for replacing currently used toxic or heavy-metal-based materials in devices and thus expand their commercialization.

Characterization of Al-based NCs

Based on our investigation of other non-toxic NCs, these materials could be a valuable addition to our list, as they constitute a promising alternative for toxic elements. Al-based NCs are not as widely studied as other III-V nanomaterials, however, can be as promising. AlSb QDs were recently synthesized[265] yielding the brightest core emission among all others III-V QDs. AlSb encountered difficulties in the bulk crystal growth leading to the conclusion that, similarly with Ga-based materials, their difficult synthesis might be a limiting factor. However, the characterization of Al-based materials can stimulate their synthesis in the future. Additionally, Al-based QD films could be modelled and their transport properties calculated in 2D QD films can be exploited.

Appendix A

Crystal Structure

A crystal structure can be determined by a primitive lattice vector (a_1, a_2, a_3) of the underlying Bavias lattice and the position of the atoms in this primitive cell. A set of lattice vectors ($\mathbf{R}$) is used to identify the content of a unit cell by distinguishing the equilibrium position of the nuclei of all the atoms included in the cell. This can interpreted mathematically as

$$\text{crystal structure} = \begin{cases} t_1, t_2, t_3, ... & \text{primitive vector} \\ d_1, d_2, d_3, ... & \text{basis of atoms} \end{cases}$$

Consequently, the formation of a crystal structure depends on the primitive vectors of the Bravias lattice and the basis vector. Therefore, a crystal with a finite number of atoms x can be represented in the following way

$$R^1 = d_1 + x_1 t_1 + x_2 t_2 + x_3 t_3 + ... \tag{A.1}$$

$$R^2 = d_2 + x_1 t_1 + x_2 t_2 + x_3 t_3 + ... \tag{A.2}$$

$$R^3 = d_3 + x_1 t_1 + x_2 t_2 + x_3 t_3 + ... \tag{A.3}$$

$$R^x = d_x + x_1 t_1 + x_2 t_2 + x_3 t_3 + ... \tag{A.4}$$

The NCs modeled in this research have a zinc-blende crystal structure in the bulk, thus this their resulting structure at nanoscale. An example of a zind-blende crystal is represented in Fig.A.1. This type of crystal can be described as two interpenetrating face centered cubic lattice (FCC), displaced by $\frac{a}{4}(1, 1, 1)$ along

the body of diagonal of the conventional cube. The Bravias lattice is an FCC lattice where each atom is surrounded by four atoms at distance $\frac{a}{4}\sqrt{3}$, where a is the lattice constant for each material. The positions of the atoms in the cell are given in terms of the primitive and basis vectors as

$$t_1 = \frac{a}{2}(1,1,0) \tag{A.5}$$

$$t_2 = \frac{a}{2}(0,1,1) \tag{A.6}$$

$$t_3 = \frac{a}{2}(1,0,1) \tag{A.7}$$

$$d_1 = (0,0,0) \tag{A.8}$$

$$d_2 = \frac{a}{4}(1,1,1) \tag{A.9}$$

By changing the integers x_1, x_2, x_3 in these equations, atomic layers are added around the primitive unit cell resulting a spherical NC with a pre-defined radius.

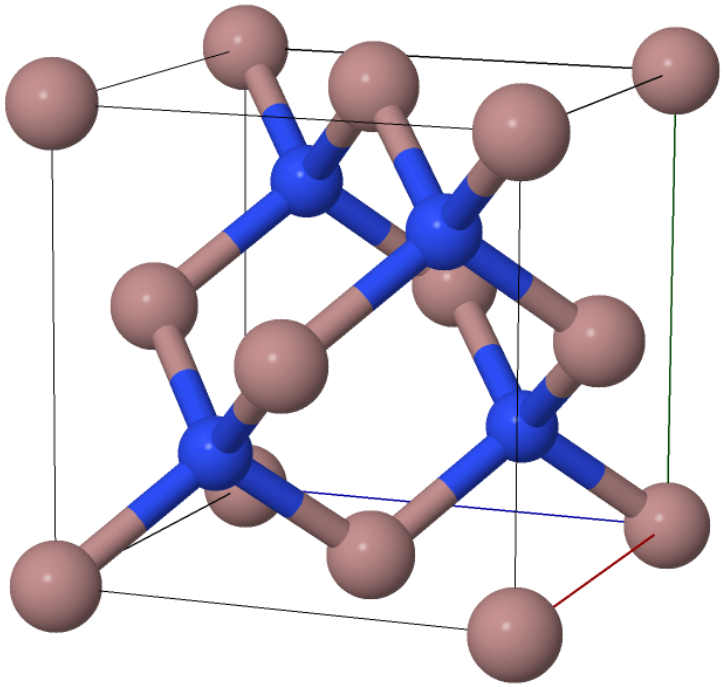

Figure A.1: Zinc-blende crystal structure representation.

Once the atomistic structure is generated the surface atoms are passivated so to remove the unsaturated bonds at the NC surface and thus avoid surface states in our calculations. This procedure is described in depth in the next chapter.

Appendix B

Fitting Parameters

d (b.l.)	**1.0**		**1.3**		**1.6**		**1.9**		**2.2**	
	μ_1	μ_2	μ_1	μ_2	μ_1	μ_2	μ_1	μ_2	μ_1	μ_2
InAs										
A	1.03	0.74	0.47	0.38	0.23	0.20	-0.04	-0.04	-1.80×10^{-3}	-1.73×10^{-3}
B	-8.10×10^{-5}	-8.02×10^{-5}	-4.99×10^{-4}	-2.84×10^{-4}	-11.03×10^{-3}	-6.67×10^{-3}	0.23	0.21	0.22	0.23
n	1.30	1.25	0.99	1.04	0.46	0.51	-0.28	-0.25	-0.73	-0.74
InP										
A	0.72	0.45	0.40	0.29	0.23	0.17	-11.63×10^{-3}	-13.66×10^{-3}	-3.81×10^{-3} 1	-4.20×10^{-3} 1
B	-1.38×10^{-7}	-2.04×10^{-5}	-6.35×10^{-4}	-1.63×10^{-4}	-13.31×10^{-3}	-5.25×10^{-3}	0.22	0.19	0.25	0.22
n	2.30	1.50	0.95	1.11	0.43	0.53	-0.45	-0.40	-0.63	-0.60
InSb										
A	0.99	0.72	0.49	0.40	0.22	0.19	0.062	0.074	-5.42×10^{-4}	-5.97×10^{-4}
B	-1.61×10^{-4}	-2.77×10^{-5}	-4.52×10^{-4}	-1.26×10^{-4}	-16.86×10^{-3}	-8.81×10^{-3}	0.25	0.24	0.21	0.20
n	1.21	1.40	1.01	1.17	0.39	0.46	-0.21	-0.18	-0.90	-0.89
GaSb										
A	0.33	0.28	0.15	0.13	65.13×10^{-3}	59.24×10^{-3}	52.08×10^{-3}	48.42×10^{-3}	-2.51×10^{-3}	-2.68×10^{-3}
B	-6.96×10^{-5}	-6.52×10^{-5}	-6.89×10^{-5}	-6.10×10^{-5}	-5.39×10^{-4}	-4.13×10^{-4}	-16.45×10^{-3}	-14.74×10^{-3}	44.81×10^{-3}	41.69×10^{-3}
n	1.14	1.13	1.09	1.09	0.71	0.73	0.17	0.18	-0.44	-0.43
InAs(inv)										
A	1.66	1.19	0.75	0.61	0.38	0.34	-57.58×10^{-3}	-65.63×10^{-3}	-2.77×10^{-3}	-2.93×10^{-3}
B	-1.32×10^{-4}	-1.23×10^{-4}	-8.01×10^{-4}	-4.55×10^{-4}	-18.61×10^{-3}	-15.07×10^{-3}	0.37	0.34	0.37	0.35
n	1.30	1.26	0.991	1.04	0.45	0.46	-0.28	-0.25	-0.74	-0.73

Table B.1: Parameters A, B and n extracted from the fitting of our result to the function $\mu = A + BT^n$ for both mobility eigenvalues, all interdot separations and all materials considered.

References

[1] Madrid, A.B.; Hyeon-Deuk, K.; Habenicht, B.F.; Prezhdo, O.V. Phonon-Induced Dephasing of Excitons in Semiconductor Quantum Dots: Multiple Exciton Generation, Fission, and Luminescence. *ACS Nano.* **2009**, *3*, 2487-94.

[2] Khan, I.; Saeed, K.; Khan, I. Nanoparticles: Properties, Applications and Toxicities. *Arab. Journ. of Chem.* **2019**, *12*, 908-931.

[3] Riel, B. J. An Introduction to Self-Assembled Quantum Dots. *Am. J. Phys.* **2008**, *76*, 750-757.

[4] Lis, K.; Bednarek, S.; Szafran, B.; Adamowski, J. Electrostatic Quantum Dots with Designed Shape of Confinement Potential *Physica E* **2003**, *17*, 494-497.

[5] Liu, M., Yazdani, N., Yarema, M. et al. Colloidal Quantum Dot Electronics. *Nat Electron* **2021**, *4*, 548–558.

[6] Cotta, M. A. Quantum Dots and Their Applications: What Lies Ahead? *ACS Appl. Nano Mater.* **2020**, *3*, 4920-4924.

[7] Yin, Y.; Alivisatos, P. Colloidal Nanocrystal Synthesis and the Organic–Inorganic Interface. *Nature* **2005**, *437*, 664–670.

[8] Murray, C. B.; Norris, D. J.; Bawendi, M. G. Synthesis and Characterization of Nearly Monodisperse CdE (E = sulfur, selenium, tellurium) Semiconductor Nanocrystallites. *J. Am. Chem. Soc.* **1993**, *115*, 8706–8715.

[9] Qu, L.; Peng, X. Control of Photoluminescence Properties of CdSe Nanocrystals in Growth. *J. Am. Chem. Soc.* **2002**, *124*, 2049-2055.

[10] Peng, X.; Manna, L.; Yang, W.; Wickham, J.; Scher, E.; Kadavanich, A.; Alivisatos, A.P. Shape Control of CdSe Nanocrystals. Nature. *Nature* **2000**, *404*, 59-61.

[11] Reiss, P.; Carrière, M.; Lincheneau, C.; Vaure, L.; Tamang, S. Synthesis of Semiconductor Nanocrystals, Focusing on Nontoxic and Earth-Abundant Materials. *Chem. Rev.* **2016**, *116*, 10731-10819.

[12] Nikazar, S.; Sivasankarapillai, V. S.; Rahdar, A.; Gasmi, S.; Anumol, P. S.; Shanavas, M. S. Revisiting the Cytotoxicity of Quantum Dots: an in-Depth Overview. *Biophysical reviews* **2020**, *12*, 703-718.

[13] Peng, X. Green Chemical Approaches Toward High-Quality Semiconductor Nanocrystals. *Chemistry* **2002**, *18*, 334-9.

[14] Zhang, Z.; Niu, Q.; Shih, C. "Electronic Growth" of Metallic Overlayers on Semiconductor Substrates. *Phys. Rev. Lett.* **1998**, *80*, 5381.

[15] Klimov, V. I. Mechanisms for Photogeneration and Recombination of Multiexcitons in Semiconductor Nanocrystals: Implications for Lasing and Solar Energy Conversion. *J. Phys. Chem. B* **2006**, *110*, 16827-16845.

[16] Heitz, R.; Stier, O.; Mukhametzhanov, I.; Madhukar, A.; Bimberg, D. Quantum Size Effect in Self-Organized InAs/GaAs Quantum Dots. *Phys. Rev. B* **2000**, *62*, 11017 .

[17] Schulte, F. K.; Bross, H. Note on the Band Theory of the Quantum Size Effect. *J. Phys. C: Solid State Phys.* **1972**, *5*, L17.

[18] Efros, A.L. Interband Light Absorption in Semiconductor Spheres *Sov. Phys. Semicond.* **1982**, *16*, 772-775.

[19] Klimov, V.I.; Mikhailovsky, A.A.; McBranch, D.W.; Leatherdale, C.A.; Bawendi, M.G. Quantization of Multiparticle Auger Rates in Semiconductor Quantum Dots. *Science* **2000**, *287*, 1011-1013.

[20] Zaini, M.S.; Liew, J.Y.C.; Ahmad, S.A.A. et al. Quantum Confinement Effect and Photoenhancement of Photoluminescence of PbS and PbS/MnS Quantum Dots. *Appl. Sci.* **2020**, *10*, 6282.

[21] Eric, D; Jiang, J.; Imran, A. et al. Effects of Quantum Confinement on Optical Properties of InN/GaN Quantum Dots. *Proceedings Volume 11336, AOPC 2019: Nanophotonics* **2019**, 113360I.

[22] Efros, A. L. Interband Absorption of Light in a Semiconductor Sphere. *Sov. Phys. Sem.* **1982**, *16*, 772.

[23] Puangmali, T.; Califano, M.; Harrison, P. The Effect of Small Elongations on the Electronic and Optical Signatures in InAs Nanocrystal Quantum Dots. *J. Phys.: Condens. Matter* **1982**, *16*, 772.

[24] Puangmali, T.; Califano, M.; Harrison, P. Monotonic Evolution of the Optical Properties in the Transition from Three- to Quasi-Two-Dimensional Quantum Confinement in InAs Nanorods. *J. Phys. Chem. C* **2010**, *114*, 6901–6908.

[25] Klimov, V., Ivanov, S., Nanda, J. et al. Single-Exciton Optical Gain in Semiconductor Nanocrystals. *Nature* **2007**, *447*, 441–446.

[26] Brus, L. E. Electron–Electron and Electron[U+2010]Hole Interactions in Small Semiconductor Crystallites: The Size Dependence of the Lowest Excited Electronic State. *J. Chem. Phys.* **1984**, *80*, 4403.

[27] Achermann, M.; Hollingsworth, J. A.; Klimov, V.I. Multiexcitons Confined Within a Subexcitonic Volume: Spectroscopic and Dynamical Signatures of Neutral and Charged Biexcitons in Ultrasmall Semiconductor Nanocrystals. *Phys. Rev. B* **2003**, *68*, 245302.

[28] Klimov, V.; Hunsche, S.; Kurz, H. Biexciton Effects in Femtosecond Nonlinear Transmission of Semiconductor Quantum Dots. *Phys. Rev. B* **1994**, *50*, 8110(R).

[29] Franceschetti, A.; Fu, H.; Wang, L. W.; Zunger, A. Many-Body Pseudopotential Theory of Excitons in InP and CdSe Quantum Dots. *Phys. Rev. B* **1999**, *60*, 1819.

[30] Brovelli, S.; Schaller, R.; Crooker, S. et al. Nano-Engineered Electron–Hole Exchange Interaction Controls Exciton Dynamics in Core–Shell Semiconductor Nanocrystals. *Nat Commun* **2011**, *2*, 280.

[31] Efros, A. L.; Rosen, M.; Kuno, M. et al. Band-Edge Exciton in Quantum Dots of Demiconductors Wth a Degenerate Valence Band: Dark and Bright Exciton States. *Phys. Rev. B* **1996**, *54*, 4843.

[32] Nirmal, M.; Norris, D.J.; Kuno, M.; Bawendi, M.G.; Efros, A.L.; Rosen, M. Observation of the "Dark Exciton" in CdSe Quantum Dots. *Phys. Rev. Lett* **1995**, *75*, 3728-31.

[33] Efros, A.L.; Kharchenko, V.A.; Rosen, M. Highly Efficient Multiple Exciton Generation in Colloidal PbSe and PbS Quantum Dots. *Solid State Commun.* **1995**, *93*, 281-284.

[34] Chepic, D.I.; Efros, A.L.; Ekimov, A.I.; Ivanov, M.G.; Kharchenko, V.A.; Kudriavtsev, I.A. Laser Cooling with PbSe Colloidal Quantum Dots. *J. Lumin* **1990**, *47*, 113-127.

[35] Schaller, R.D.; Klimov, V.I. High Efficiency Carrier Multiplication in PbSe Nanocrystals: Implications for Solar Energy Conversion. *Phys. Rev. Lett.* **2004**, *92*, 186601.

[36] Klimov, V.I.; Ivanov, S.A.; Nanda, J.; Achermann, M.; Beze, I.; et al. Single-Exciton Optical Gain in Semiconductor Nanocrystals. *Nature* **2007**, *447*, 441-446.

[37] Hanna, M.C.; Nozik, A.J. Solar Conversion Efficiency of Photovoltaic and Photoelectrolysis Cells with Carrier Multiplication Absorbers. *J. Appl. Phys.* **2006**, *100*, 074510.

[38] Klimov, V.I.; Mikhailovsky, A.A.; Xu, S.; Malko, A.; Hollingsworth, J.A.; Leatherdale, C.A.; Eisler, H.; Bawendi, M.G. Optical Gain and Stimulated Emission in Nanocrystal Quantum Dots. *Science.* **2000**, *290*, 314-7.

[39] Mikhailovsky, A.A.; Malko, A.V.; Hollingsworth, J. A.; Bawendi, M. G.; Klimov, V.I. Multiparticle Interactions and Stimulated Emission in Chemically Synthesized Quantum Dots. *Appl. Phys. Lett.* **2002**, *80*, 2380.

[40] Klimov, V.I. Multicarrier Interactions in Semiconductor Nanocrystals in Relation to the Phenomena of Auger Recombination and Carrier Multiplication. *Annu. Rev. Condens. Matter Phys.* **2014**, *5*, 285-316.

[41] Califano, M. Suppression of Auger Recombination in Nanocrystals via LigandAssisted Wave Function Engineering in Reciprocal Space. *J. Phys. Chem. Lett.* **2018**, *9*, 2098−2104.

[42] Sandberg, R.L.; Padilha, L.A.; Qazilbash, M.M.; Bae, W.K.; Schaller, R.D.; et al. Multiexciton Dynamics in Infrared-Emitting Colloidal Nanostructures Probed by a Superconducting Nanowire Single-Photon Detector. *ACS Nano* **2012**, *6*, 9532-9540.

[43] Padilha, L.A.; Stewart, J.T.; Sandberg, R.L.; Bae, W.K.; Koh, W-K.; et al. Carrier Multiplication in Semiconductor Nanocrystals: Influence of Size, Shape, and Composition. *Acc. Chem. Res.* **2013**, *46*, 1261–1269.

[44] Hou, X.; Kang, J.; Qin, H. et al. Engineering Auger Recombination in Colloidal Quantum Dots via Dielectric Screening. *Nat Commun* **2019**, *10*, 1750.

[45] Melnychuk, C.; Guyot-Sionnest, P. Auger Suppression in n-Type HgSe Colloidal Quantum Dots. *ACS Nano* **2019**, *13*, 10512–10519.

[46] Kim, Y. H.; Wolf, C.; Kim, Y. T. et al. Highly Efficient Light-Emitting Diodes of Colloidal Metal–Halide Perovskite Nanocrystals beyond Quantum Size. *ACS Nano* **2011**, *17*, 6586-6593.

[47] Beard, M. C.; Peng, X.; Hens, Z.; Weiss, E. A. Introduction to special issue: Colloidal Quantum Dots. *J. Chem. Phys.* **2020**, *153*, 240401.

[48] Li, X., Zhao, YB., Fan, F. et al. Bright Colloidal Quantum Dot Light-Emitting Diodes Enabled by Efficient Chlorination. *Nature Photon* **2018**, *12*, 159–164.

[49] Chang, J.; Waclawik, E. R. Colloidal Semiconductor Nanocrystals: Controlled Synthesis and Surface Chemistry in Organic Media. *RSC Adv.* **2014**, *4*, 3505-23527.

[50] Roh, J.; Park, YS.; Lim, J. et al. Optically Pumped Colloidal-Quantum-Dot Lasing in LED-like Devices with an Iintegrated Optical Cavity. *Nat Commun* **2020**, *11*, 271.

[51] Talapin, D.V.; Lee, J.; Kovalenko, M. V.; Shevchenko, E. V. Prospects of Colloidal Nanocrystals for Electronic and Optoelectronic Applications. *Chem. Rev.* **2010**, *110*, 389-458.

[52] Jung, H.; Ahn, N.; Klimov, V.I. Prospects and Challenges of Colloidal Quantum Dot Laser Diodes. *Nat. Photon.* **2021**, *15*, 643–655.

[53] Park, Y. S.; Roh J.; Diroll, B.T. et al. Colloidal Quantum Dot Lasers. *Nat Rev Mater* **2021**

[54] Cao, Z.; Hu, F.; Zhang, C.; Zhu, S. N.; Xiao, M.; Wang, X. Optical Studies of Semiconductor Perovskite Nanocrystals For classical Optoelectronic Applications And Quantum Information Technologies: a Review. *Advanced Photonics* **2020**, *2*, 054001.

[55] Tang, X.; Hu, Z.; Chen, W. et al. Room Temperature Single-Photon Emission and Lasing for All-Inorganic Colloidal Perovskite Quantum Dots. *Nano Energy* **2016**, *28*, 462–468.

[56] Huang, H.; Polavarapu, L.; Sichert, J. et al. Colloidal Lead Halide Perovskite Nanocrystals: Synthesis, Optical Properties and Applications. *NPG Asia Mater* **2016**, *8*, e328.

[57] Yuan, Z.; Nakamura, T. Spectral Tuning of Colloidal Si Nanocrystal Luminescence by Post-Laser Iirradiation in Liquid. *RSC Adv.* **2020**, *10*, 32992-32998.

[58] Weisbuch, C.; Nagle, J. The Physics of the Quantum Well Laser. *Phys. Scr.* **1987**, *209*

[59] Oberg, V. A.; Johansson, M. B.; Zhang, X.; Johansson, E. M. J. Cubic AgBiS2 Colloidal Nanocrystals for Solar Cells. *ACS Appl. Nano Mater.* **2020**, *3*, 4014–4024.

[60] So, D.; Pradhan, D.; Konstantatos, G. Solid-State Colloidal CuInS2 Quantum Dot Solar Cells Enabled by Bulk Heterojunctions. *Nanoscale* **2016**, *8*, 16776-16785.

[61] Hillhouse, H. W.; Beard, M. C. Solar cells from colloidal nanocrystals: Fundamentals, Materials, Devices, and Economics. *Current Opinion in Colloid and Interface Science* **2009**, *14*, 245–259.

[62] Kim, T., Kelley, M.L., Kim, D. et al. Purification of Colloidal Nanocrystals Along the Road to Highly Efficient Photovoltaic Devices. *Int. J. of Precis. Eng. and Manuf.-Green Tech.* **2020**

[63] Zhou, F.; Li, Z.; Chen, H. et al. Application of Perovskite Nanocrystals (NCs)/Quantum Dots (QDs) in Solar Cells. *Nano Energy* **2020**, *73*, 104757.

[64] Que, M.; Zhu, L.; Guo, Y.; Que, W.; Yun, S. Toward Perovskite Nanocrystalline Solar Cells: Progress and Potential. *J. Mater. Chem. C* **2020**, *8*, 5321-5334.

[65] Fu, H. Colloidal Metal Halide Perovskite Nanocrystals: a Promising Juggernaut in Photovoltaic Applications. *J. Mater. Chem. A* **2019**, *7*, 14357-14379.

[66] Song, J.H.; Jeong, S. Colloidal Quantum Dot Based Solar Cells: from Materials to Devices. *Nano Convergence* **2017**, *4*.

[67] Lee, H.; Song, H.; Shim, M.; Lee, C. Towards the Commercialization of Colloidal Quantum Dot Solar Cells: Perspectives on Device Structures and Manufacturing. *Energy Environ. Sci.* **2020**, *13*, 404-431.

[68] Neo, D. C. J.; Stranks, S. D.; Eperon, G. E. Quantum Funneling in Blended Multi-Band Gap Core/Shell Colloidal Quantum Dot Solar Cells. *Appl. Phys. Lett.* **2015**, *107*, 103902.

[69] Gomez-Campos, F. M.; Rodríguez-Bolívar, S.; Skibinsky-Gitlin, E. S.; Califano, M. Efficient, Non-Stochastic, Monte-Carlo-Like-Accurate Method for the Calculation of the Temperature-Dependent Mobility in Nanocrystal Films. *Nanoscale 10*, **(2018)**, 9679-9690.

[70] Talapin, D. V.; Murray, C. B. PbSe Nanocrystal Solids for n- and p-Channel Thin Film Field-Effect Transistors. *Science 310*, **(2005)**, 86–89.

[71] Califano, M.; Rodosthenous, P. Theoretical Characterization of GaSb Colloidal Quantum Dots and Their Application to Photocatalytic CO_2 Reduction with Water. *ACS Appl. Mater. Interfaces* **2019**, *11*, 640−646.

[72] Burke, R.; Bren, K. L.; Krauss, T. D. Semiconductor Nanocrystal Photocatalysis for the Production of Solar Fuels. *J. Chem. Phys.* **2021**, *154*, 030901.

[73] Weiss, E. A. Designing the Surfaces of Semiconductor Quantum Dots for Colloidal Photocatalysis. *ACS Energy Lett.* **2017**, *2*, 1005–1013.

[74] Vaneski, A.; Schneider, J.; Susha, A. S.; Rogach, A. L. Colloidal Hybrid Heterostructures Based on II–VI Aemiconductornanocrystals for Photocatalytic Hydrogen Generation. *Journal of Photochemistry and Photobiology C: Photochemistry Reviews* **2014**, *19*, 52–61.

[75] Kawawaki, T.; Mori, Y.; Wakamatsu, K. et al. Controlled Colloidal Metal Nanoparticles and Nanoclusters: Recent Applications as Cocatalysts for Improving Photocatalytic Water-Splitting Activity. *J. Mater. Chem. A* **2020**, *8*, 16081-16113.

[76] Moroz, P.; Boddy, A.; Zamkov, M. Challenges and Prospects of Photocatalytic Applications Utilizing Semiconductor Nanocrystals. *Frontiers in Chemistry* **2018**, *6*, 353.

[77] Yuan, Y.; Jin, N.; Saghy, P.; Dube, L.; Zhu, H.; Chen, O. Quantum Dot Photocatalysts for Organic Transformations *J. Phys. Chem. Lett.* **2021**, *12*, 7180-7193.

[78] Slussarenko, S.; Pryde, G.J. Photonic Quantum Information Processing: A Concise Review. *Appl. Phys. Rev.* **2019**, *6*, 041303.

[79] Petta, J.R.; Johnson, A.C.; Taylor, J.M. et al. Coherent Manipulation of Coupled Electron Spins in Semiconductor Quantum Dots. *Science.* **2005**, *309*, 2180.

[80] Farahani, J.N.; Pohl, D.W.; Eisler, H.J.; Hecht, B. Single Quantum Dot Coupled to a Scanning Optical Antenna: A Tunable Superemitter. *Phys. Rev. Lett.* **2005**, *95*, 017402.

[81] Scheibner, R.; Buhmann, H.; Reuter, D.; Kiselev, M.N.; Molenkamp, W. Thermopower of a Kondo Spin-Correlated Quantum Dot. *Phys. Rev. Lett.* **2005**, *95*, 176602.

[82] Feng, M.; D'Amico, I.; Zanardi, P.; Rossi, F. Spin-Based Quantum-Information Processing with Demiconductor Wuantum Fots and Cavity QED. *Phys. Rev. A* **2003**, *67*, 014306.

[83] Basso Basset, F.; Salusti, F.; Schweickert, L. et al. Quantum Teleportation with Imperfect Quantum Dots. *npj Quantum Inf* **2021**, *7*, 7.

[84] Abdel-Salam, M.; Omran, B.; Whitehead, K.; Baek, K. Superior Properties and Biomedical Applications of Microorganism-Derived Fluorescent Quantum Dots. *Molecules* **2020**, *25*, 4486.

[85] Waiskopf, N., Rotem, R., Shweky, I. et al. Labeling Acetyl- and Butyrylcholinesterase Using Semiconductor Nanocrystals for Biological Applications. *BioNanoSci.* **2013**, *3*, 1–11.

[86] Fu, A.; Gu, W.; Larabell, C.; Alivisatos, A.P. Semiconductor Nanocrystals for Biological Imaging. *Current Opinion in Neurobiology* **2005**, *15*, 568–575.

[87] Bruchez, M.; Moronne, M.; Gin, P.; Weiss, S.; Alivisatos, A.P. Semiconductor Nanocrystals as Fluorescent Biological Labels. *Science* **1998**, *281*, 2013.

[88] Lavorato, G.C.; Das, R.; Masa, J.A.; Phan, M.; Srikanth, H. Hybrid Magnetic Nanoparticles as Efficient Nanoheaters in Biomedical Applications. *Nanoscale Adv.* **2021**, *3*, 867-888.

[89] Alaghmandfard, A.; Sedighi, O.; Rezaei, N.T. et al. Recent Advances in the Modification of Carbon-Based Quantum Dots for Biomedical Applications. *Materials Science & Engineering C* **2021**, *120*, 11175621.

[90] Xiaohu, G.; Warren , C. W. C.; Shuming , N. Quantum-Dot Nanocrystals for Ultrasensitive Biological Labeling and Multicolor Optical Encoding. *J. of Biomedical Optics* **2002**, *7*, 532-537.

[91] Bester, G. Electronic Excitations in Nanostructures: an Empirical Pseudopotential Based Approach. *J. Phys.: Condens. Matter* **2008**, *21*, 023202.

[92] Hamann, D. R.; Schluter, M.; Chiang, L. Norm-Conserving Pseudopotentials. *Phys. Rev. Lett.* **1979**, *43*,1494.

[93] Vanderbilt, D. Optimally Smooth Norm-Conserving Pseudopotentials. . Rev. B **1985**, *32*, 8412.

[94] Troullier, N.; Martins, J. L. A straightforward Method for Generating Soft Transferable Pseudopotentials. *Chem. Mater.* **1990**, *74*, 613.

[95] Graf, P.A.; Kim, K.; Jones, W.B.; Wang, L.W. Surface Passivation Optimization Using DIRECT. *J. Comput. Phys.* **2007**, *224*, 824-835.

[96] Wang, L.-W.; Zunger, A. Pseudopotential Calculations of Nanoscale CdSe Quantum Dots. *Phys. Rev. B* **1996**, *53*, 9579.

[97] Fu, H.; Zunger A. InP Quantum Dots: Electronic Structure, Surface Effects, and the Redshifted Emission. *Phys. Rev. B* **1997**, *56*, 1496-1508.

[98] Wang, L-W.; Zunger A. Local-Density-Derived Semiempirical Pseudopotentials. *Phys. Rev. B* **1995**, *51*, 17398-17416.

[99] Wang, L-W.; Zunger A. Electronic Structure Pseudopotential Calculations of Large (.apprx.1000 Atoms) Si Quantum Dots. *J. Phys. Chem.* **1994**, *98*, 2158–2165.

[100] Wang, L-W.; Zunger A. Solving Schrödinger's Equation Around a Desired Energy: Application to Silicon Quantum Dots. *J. Chem. Phys.* **1994**, *100*, 2394–2397.

[101] Benedict, L. X.; Screening in the Exchange Term of the Electron–Hole Interaction of the Bethe–Salpeter Equation. *Phys. Rev. B* **2002**, *66*,193105.

[102] Zhonghua, Y.; Jingbo, L.; Donald, B. O.; Lin-Wang, W., Paul, F. B. Large Resonant Stokes Shift in CdS Nanocrystals. *J. Phys. Chem. B* **2203**, *107*, 5670-5674.

[103] Efros, Al. L.; Rosen, M.; Kuno, M.; Nirmal, M.; Norris, D. J.; Bawendi, M. Band-Edge Exciton in Quantum Dots of Semiconductors with a Degenerate Valence Band: Dark and Bright Exciton States. *Phys. Rev. B* **1996**, *54*, 4843–4856.

[104] Calcott, P. D. J. et al . Identification of Radiative Transitions in Highly Porous Silicon. *J. Phys.: Condens. Matter* **1993**, *5*, L91–L98.

[105] Mićić, O.; Sprague, J.; Lu, Z.; Nozik, A. J. Highly Efficient Band–Edge Emission from InP Quantum Dots. *Appl. Phys. Lett.* **1996**, *68*, 3150.

[106] Demchenko, D. O.; Wang, L-W. Optical Transitions and Nature of Stokes Shift in Spherical CdS Quantum Dots. *Phys. Rev. B* **2006**, *73*, 155326.

[107] Fafard, S.; Leonard, D.; Merz, J. L.; Petroff, P. M. Selective Excitation of the Photoluminescence and the Energy Levels of Ultrasmall InGaAs/GaAs Quantum Dots. *Appl. Phys. Lett.* **1994**, *65*, 1388.

[108] Wang, L. W.; Califano, M.; Zunger, A.; Franceschetti, A. Pseudopotential Theory of Auger Processes in CdSe Quantum Dots. *Phys. Rev. Lett.* **2003**, *91*, 056404.

[109] Califano, M. Direct and Inverse Auger Processes in InAs Nanocrystals: Can the Decay Signature of a Trion Be Mistaken for Carrier Multiplication? *ACS Nano* **2009**, *3*, 2706-2714.

[110] Gulati, S.; Sachdeva, M.; Bhasin, K. K. Capping Agents in Nanoparticle Synthesis: Surfactant and Solvent System. *AIP Conf. Proc.* **2018**, *1953*, 030214-1–030214-4.

[111] Dielectric Constants of Common Materials. https://www.kabusa.com/Dilectric-Constants.pdf.

[112] Ablowitz, M. J.; Cole, J. T. Tight-Binding Methods for General Longitudinally Driven Photonic Lattices : Edge States and Solitons. *Phys. Rev. A* **2017**, *96*, 043868.

[113] Po, H. C.; Zou, L.; Senthil, T.; Vishwanath, A. Faithful Tight-Binding Models and Fragile Topology of Magic-Angle Bilayer Graphene. *Phys. Rev. B* **2019**, *99*, 195455.

[114] Efros, A. L.; Shklovskii, B. I. Percolation Theory and Conductivity of Strongly Inhomogeneous Media. *Soviet Physics* **1975**, *18*, 845-862.

[115] Efros, A. L.; Shklovskii, B. I. Coulomb Gap and Low Temperature Conductivity of Disordered Systems. *Journal of Physics C* **1975**, *8*, 49-51.

[116] Suhov, Y.; Kelbert, M. Markov Chains: A Primer in Random Processes and thier Applications. **2008**

[117] Dutta, P. S.; Bhat, H. L.; Kumar V. The Physics and Technology of Gallium Antimonide: An Emerging Optoelectronic Material. *J. Appl. Phys.* **1997**, *81*, 5821-5870.

[118] Motosugi, G.; Kagawa, T. Temperature Dependence of the Threshold Current of AlGaAsSb/GaSb DH Lasers *Jpn. J. Appl. Phys.* **1980**, *19*, 2303.

[119] Ohmori, Y.; Tarucha, S.; Horikoshi, Y.; Okamoto, H. Room Temperature Operation of $Al_{0.17}Ga_{0.83}Sb$/GaSb Multi-Quantum Well Lasers Grown by Molecular Beam Epitaxy, *Jpn. J. Appl. Phys.* **1984**, *23*, L94-L96.

[120] Morosini, M. B. Z.; Herrera-Perez, J. L.; Loural, M. S. S.; Von Zuben, A. A. G.; da Silveira, A. C. F.; Patel, N. B. Low-Threshold GaInAsSb/GaAlAsSb Double-Heterostructure Lasers Grown by LPE *IEEE J. Quantum Electron.* **1993** *29*, 2103-2108.

[121] Hildebrand, O.; Kuebart, W.; Benz, K. W.; Pilkuhn, M. H. $Ga_{1-x}Al_xSb$ Avalanche Photodiodes: Resonant Impact Ionization with Very High Ratio of Ionization Coefficients *IEEE J. Quantum Electron.* **1981** *17*, 284-288.

[122] Hildebrand, O.; Kuebart, W.; Pilkuhn, M. H. Resonant Enhancement of Impact in $Ga_{1-x}Al_xSb$ *Appl. Phys. Lett.* **1980**, *37*, 801.

[123] Segawa, K.; Miki, H.; Otsubo, M.; Shirata, K. Coherent Gunn Oscillations in $Ga_xIn_{1-x}Sb$ *Electron. Lett.* **1976** *12*, 124-125.

[124] Hilsum, C.; Rees, H. D. Three-Level Oscillator: a New Form of Transferred-Electron Device *Electron. Lett.* **1970** *6*, 277-278.

[125] L. M. Fraas, L. M.; Girard, G. R.; Avery, J. E.; Arau, B. A.; Sundaram, V. S.; Thompson, A. G.; Gee, J. M. GaSb Booster Cells for Over 30% Efficient Solar-Cell Stacks. *J. Appl. Phys.* **1989** *66*, 3866-3870.

[126] Juang, B.-C.; Laghumavarapu, R. B.; Foggo, B. J.; Simmonds, P. J.; Lin, A.; Liang, B.; Huffaker, D. L. GaSb Thermophotovoltaic Cells Grown on GaAs by Molecular Beam Epitaxy Using Interfacial Misfit Arrays *Appl. Phys. Lett.* **2015**, *106*, 111101-1–111101-5.

[127] Kazakova, O.; Gallop, J. C.; Cox, D. C.; Brown, E.; Cuenat, A.; Suzuki, K. Optimization of 2DEG InAs/GaSb Hall Sensors for Single Particle Detection. *IEEE Trans. Magn.* **2008**, *44*, 4480-4483.

[128] Ohmori, Y.; Suzuki, Y.; Okamoto, H. Room Temperature CW Operation of GaSb/AlGaSb MQW Laser Diodes Grown by MBE. *Jpn. J. Appl. Phys.*, **1985** *24*, L657-L660.

[129] Johnson, J. L.; Samoska, L. A.; Gossard, A. C.; Merz, J. L.; Jack, M. D.; Chapman, G. R.; Baumgratz, B. A.; Kosai, K.; Johnson S. M. Electrical and Optical Properties of Infrared Photodiodes Using the InAs/$Ga_{1-x}In_xSb$ Superlattice in Heterojunctions with GaSb. *J. Appl. Phys.* **1996**, *80*, 1116.

[130] M. Motyka, M.; Sek, G.; Ryczko, K.; Misiewicz, J.; Lehnhardt, T.; Höfling, S.; Forchel, A. Optical Properties of GaSb-Based Type II Quantum Wells as the Active Region of Midinfrared Interband Cascade Lasers for Gas Sensing Applications *Appl. Phys. Lett.* **2009** *94*, 251901.

[131] Babadi, A. S.; Svensson, J.; Lind, E.; Wernersson, L.-E. Impact of Doping and Diameter on the Electrical Properties of GaSb Nanowires. *Appl. Phys. Lett.* **2017** *110*, 053502.

[132] Dey, A. W.; Svensson, J.; Borg, B. M.; Ek, M.; Wernersson, L.-E. Single InAs/GaSb Nanowire Low-Power CMOS Inverter *Nano Lett.* **2012**, *12*, 5593-5597.

[133] Shterengas, L.; Belenky, G. L.; Gourevitch, A.; Donetsky, D.; Kim, J. G.; Martinelli, R. U.; Westerfeld, D. High-Power 2.3-μm GaSb-Based Linear Laser Array. *IEEE Photonics Technol. Lett.* **2004** *16*, 2218-2220.

[134] Mourad, C.; Gianardi, D.; Kaspi, R. 2 μm GaInAsSb/AlGaAsSb Midinfrared Laser Grown Digitally on GaSb by Modulated-Molecular Beam Epitaxy *J. Appl. Phys.* **2000** *88*, 5543-5546.

[135] Tomlins, P. H.; Wang, R. K. Theory, Developments and Applications of Optical Coherence Tomography. *J Phys D: Appl Phys* **2005**, *38*, 2519-2535.

[136] Marent, A.; Geller, M.; Schliwa, A.; Feise, D.; Pötschke, K.; Bimberg, D. 10^6 Years Extrapolated Hole Storage Time in GaSb/AlAs Quantum Dots *Appl. Phys. Lett.* **2007**, *91*, 242109.

[137] Geller, M.; Marent, A.; Bimberg, D. *Handbook of Nanophysics: Nanoelectronics and Nanophotonics*, K. D. Sattler (CRC Press, Boca Raton, FL.,2010), Sec.2.1.

[138] Hayne, M.; Young, R. J.; Smakman, E. P.; Nowozin, T.; Hodgson, P.; Garleff, J. K.; Rambabu, P.; Koenraad, P. M.; Marent, A.; Bonato, L.; Schliwa, A.; Bimberg, D. The Structural, Electronic and Optical Properties of GaSb/GaAs Nanostructures for Charge-Based Memory *J. Phys. D: Appl. Phys.* **2013** *46* 264001.

[139] Sala, E. M.; Stracke, G.; Selve, S.; Niermann, T.; Lehmann, M.; Schlichting, S.; Nippert, F.; Callsen, G.; Strittmatter, A.; Bimberg, D. Growth and Structure of $In_{0.5}Ga_{0.5}Sb$ Quantum Dots on GaP(001), *Appl. Phys. Lett.* **2016**, *109*, 102102.

[140] Jasieniak, J.; Califano, M.; Watkins, S. E. Size-Dependent Valence and Conduction Band-Edge Energies of Semiconductor Nanocrystals *ACS Nano* **2011**, *5*, 5888-5902.

[141] Miura, N. *Physics of Semiconductors in High Magnetic Fields* Oxford science publications, OUP Oxford, 2008, ISBN: 0198517564, 9780198517566

[142] Luo, J.-W.; Franceschetti, A.; Zunger, A. Quantum-Size-Induced Electronic Transitions in Quantum Dots: Indirect Band-Gap GaAs. *Phys. Rev. B* **2008**, *78*, 035306.

[143] Group IV, Elements, IV-IV and III-V Compounds. Part b - Electronic, Transport, Optical and Other Properties. In *Landolt- Börnstein - Group III Condensed Matter*, Madelung, O.; Rössler, U.; Schulz, M., Eds.; Springer-Verlag: Germany, 2002; Vol. 41A1b.

[144] Allan, G.; Niquet, Y. M.; Delerue, C. Quantum Confinement Energies in Zinc-Blende III-V and Group IV Semiconductors. *Appl. Phys. Lett.* **2000** *77*, 639-641.

[145] Xie, S.; Zhang, Q.; Liu, G.; Wang, Y. Photocatalytic and Photoelectrocatalytic Reduction of CO2 Using Heterogeneous Catalysts with Controlled Nanostructures. *Chem. Commun.* **2016**, *52*, 35-59.

[146] Williamson, A. J.; Zunger, A. Pseudopotential Study of Electron-Hole Excitations in Colloidal Free-Standing InAs Quantum Dots. *Phys. Rev. B* **1999** *61*, 1978-1991.

[147] Califano, M. Suppression of Auger Recombination in Nanocrystals via Ligand-Assisted Wave Function Engineering in Reciprocal Space *J. Phys. Chem. Lett.* **2018** *9*, 2098-2104.

[148] Brus, L. E., Electron-Electron and Electron-Hole Interactions in Small Semiconductor Crystallites: The Size Dependence of the Lowest Excited Electronic State. *J. Chem. Phys.* **1984** *80*, 4403-4409.

[149] Fu, H.; Zunger, A. Local-Density-Derived Semiempirical Nonlocal Pseudopotentials for InP with Applications to Large Quantum Dots *Phys. Rev. B* **1997** *55*, 1642-1653.

[150] Micic, O. I.; Cheong, H. M.; Fu, H.; Zunger, A.; Sprague, J. R.; Mascarenhas, A.; Nozik, A. J. Size-Dependent Spectroscopy of InP Quantum Dots. *J. Phys. Chem. B* **1997**, *101*, 4904-4912.

[151] Reboredo, F.; Franceschetti, A.; Zunger, A. Excitonic Transitions and Exchange Splitting in Si Quantum Dots *Appl. Phys. Lett.* **1999** *75*, 2972-2974.

[152] Tu, C.-C.; Awasthi, K.; Chen, K.-P.; Lin, C.-H.; Hamada, M.; Ohta, N.; Li, Y.K. Time-Gated Imaging on Live Cancer Cells Using Silicon Quantum Dot Nanoparticles with Long-Lived Fluorescence. *ACS Photonics*, **2017**, *4*, 1306-1315.

[153] Meinardi, F.; Colombo, A.; Velizhanin, K. A.; Simonutti, R.; Lorenzon, M.; Beverina, L.; Viswanatha, R.; Klimov, V. I.; Brovelli, S. Large-Area Luminescent Solar Concentrators Based on 'Stokes-Shift-Engineered' Nanocrystals in a Mass-Polymerized PMMA Matrix. *Nat. Phot.* **2014**, *8*, 392-399.

[154] Meinardi, F.; Ehrenberg, S.; Dhamo, L.; carulli, F.; Mauri, M.; Bruni, F.; Simonutti, R.; Kortshagen, U.; Brovelli, S. Highly Efficient Luminescent Solar Concentrators Based on Earth-Abundant Indirect-Bandgap Silicon Quantum Dots. *Nat. Phot.* **2017**, *11*, 177-185.

[155] Luo, J. W.; Franceschetti, A.; Zunger, A. Nonmonotonic Size Dependence of the Dark/Bright Exciton Splitting in GaAs Nanocrystals. *Phys. Rev. B* **2009** *79*, 201301(R)

[156] Yang, B.; Schneeloch, J. E.; Pan, Z.; Furis, M.; Achermann, M. Radiative Lifetimes and Orbital Symmetry of Electronic Energy Levels of CdS Nanocrystals: Size Dependence *Phys. Rev. B* **2010** *81*, 073401.

[157] de Mello Donegá, C.; Bode, M; Meijerink, A. Size- and Temperature-Dependence of Exciton Lifetimes in CdSe Quantum Dots *Phys. Rev. B* **2006** *74*, 085320.

[158] Gong, K.; Zeng, Y.; Kelley, D. F. Extinction Coefficients, Oscillator Strengths, and Radiative Lifetimes of CdSe, CdTe, and CdTe/CdSe Nanocrystals. *J. Phys. Chem. C* **2013**, *117*, 20268-20279.

[159] Yu, P. R.; Beard, M. C.; Ellingson, R. J.; Ferrere, S.; Curtis, C.; Drexler, J.; Luiszer, F.; Nozik, A. J. Absorption Cross-Section and Related Optical Properties of Colloidal InAs Quantum Dots *J. Phys. Chem. B* **2005**, *109*, 7084-7087.

[160] Yu, P.Y.; Cardona, M. Fundamentals of Semiconductors: Physics and Materials Properties. 4th edtion. Springer Berlin Heidelberg, **2010**, ISBN 978-3-642-00709-5.

[161] Xie, S.; Zhang, Q.; Liu, G.; Wang, Y. Photocatalytic and photoelectrocatalytic reduction of CO_2 using heterogeneous catalysts with controlled nanostructures *Chem. Commun.* **2016**, *52*, 35.

[162] Osterloh, F. E. Inorganic Nanostructures for Photoelectrochemical and Photocatalytic Water Splitting *Chem. Soc. Rev.* **2013**, *42*, 2294-2320.

[163] Chen, X.; Zhou, Y.; Liu, Q.; Li, Z.; Liu, J.; Zou, Z. Ultrathin, Single-Crystal WO_3 Nanosheets by Two-Dimensional Oriented Attachment toward Enhanced Photocatalystic Reduction of CO_2 into Hydrocarbon Fuels under Visible Light *ACS Appl. Mater. Interfaces.* **2012** *4*, 3372-3377.

[164] Li, P.; Zhou, Y.; Zhao, Z.; Xu, A.; Wang, X.; Xiao, M.; Zou, Z. Hexahedron Prism-Anchored Octahedronal CeO_2: Crystal Facet-Based Homojunction Promoting Efficient Solar Fuel Synthesis *J. Am. Chem. Soc.* **2015** *137*, 9547-9550.

[165] Xie, S.; Wang, Y.; Zhang, Q.; Deng, W.; Wang, Y. MgO- and Pt-Promoted TiO_2 as an Efficient Photocatalyst for the Preferential Reduction of Carbon Dioxide in the Presence of Water. *ACS Catal.* **2014** *4*, 3644-3653.

[166] Kodaimati, M. S.; Lian, S.; Schatz, G. C.; Weiss, E. A. Energy Transfer-Enhanced Photocatalytic Reduction of Protons within Quantum Dot Light-Harvesting-Catalyst Assemblies. *Proc. Nat. Acad. Sci.* **2018** 201805625.

[167] Talapin, D.V.; Lee, J.; Kovalenko, M. V.; Shevchenko, E. V. Prospects of Colloidal Nanocrystals for Electronic and Optoelectronic Applications. *Chem. Rev.* **2010**, *110*, 389-458.

[168] Kovalenko, M. V.; Manna, L.; Cabot, A.; Hens, Z.; Talapin, D.V.; Kagan, C. R.; Klimov, V. I.; Rogach, A. L.; Reiss, P.; Milliron, D. J.; et al. Prospects of Nanoscience with Nanocrystals. *ACS Nano* **2015**, *9*,1012-1057.

[169] Reiss, P.; Carriere, M.; Lincheneau, C.; Vaure, L.; Tamang, S. Synthesis of Semiconductor Nanocrystals, Focusing on Nontoxic and Earth-Abundant Materials. *Chem. Rev.* **2016**, *116*, 10731-10819.

[170] Tamang, S.; Linchemeau, C.; Hermans, Y.; Jeong, S.; Reiss, P. Chemistry of InP Nanocrystal Syntheses. *Chem. Mater.* **2016**, *28*, 2491-2506.

[171] Xu, G.; Zeng, S.; Zhang,B.; Swihart, M. T.; Yong, K.; Prasad, P. N. New Generation Cadmium-Free Quantum Dots for Biophotonics and Nanomedicine. *Chem. Rev.* **2016**, *116*, 12234-12327.

[172] Seo, H.; Bang, M.; Fu, H.; Kim, Y.; Son, C.; Jeon, H. B.; Kim, S. Unprecedented surface stabilized InP quantum dots with bidentate ligands. *RSC Adv.* **2020**, *10*, 11517-11523.

[173] Koh, S.; Lee, H.; Lee, T.; Park, K.; Kim, W.; Lee, D. C.; Enhanced thermal stability of InP quantum dots coated with Al-doped ZnS shell. *J. Chem. Phys.* **2019**, *151*, 144704.

[174] Jang, E.; Kim, Y.; Won, Y.; Jang, H.; Choi, S. Environmentally Friendly InP-Based Quantum Dots for Efficient Wide Color Gamut Displays. *ACS Energy Lett.* **2020**, *5*, 1316–1327.

[175] Micic, O. I.; Cheong, H. M.; Fu, H.; Zunger, A.; Sprague, J. R.; Mascarenhas, A.; Nozik, A. J. Size-Dependent Spectroscopy of InP Quantum Dots. *J. Phys. Chem. B* **1997**, *101*, 4904-4912.

[176] Li, Y.; Hou, X.; Dai, X.; Yao, Z.; Lv, L.; Jin, Y.; Peng, X. Stoichiometry-Controlled InP-Based Quantum Dots: Synthesis, Photoluminescence, and Electroluminescence. *J. Am. Chem. Soc.* **2019**, *141*, 6448-6452.

[177] Crisp, R. W.; Kirkwood, N.; Grimaldi, G.; Kinge, S.; Siebbeles, L. D. A.; Houtepen A. J. Highly Photoconductive InP Quantum Dots Films and Solar Cells. *ACS Appl. Energy Mater.* **2018**, *1*, 6569-6576.

[178] Zhang, J.; Wang, J.; Yan, T.; Peng, Y.; Xu, D. J.; Deng, D. W. InP/ZnSe/ZnS Quantum Dots With Strong Dual Emissions: Visible Excitonic Emission and Near-Infrared Surface Defect Emission and Their Application in in Vitro and in Vivo Bioimaging. *J. Mater. Chem. B* **2017**, *5*, 8152-8160.

[179] Ikezawa, M.; Pal, B.; Masumoto, Y.; Ignatiev, I.V.; Verbin, S. Y.; Gerlovin, I. Y. Submillisecond Electron Spin Relaxation in InP Quantum Dots. *Phys. Rev. B* **2005**, *72*, 153302.

[180] Yang, X.; Zhao, D.; Leck, K. S.; Tan, S. T.; Tang, Y. X.; Zhao, J.; Demir, H. V.; Sun, X. W. Full Visible Range Covering InP/ZnS Nanocrystals with High Photometric Performance and Their Application to White Quantum Dot Light-Emitting Diodes. *Adv. Mater* **2012**, *24*, 4180-4185.

[181] Micic, O. I.; Ahrenkiel, S. P. ; Nozik, A. J. Synthesis of Extremely Small InP Quantum Dots and Electronic Coupling in Their Disordered Solid Films. *Appl. Phys. Lett.* **2001**, *78*, 4022-4024.

[182] Stein, J. L. ; Mader, E. A.; Cossairt, B. M. Luminescent InP Quantum Dots with Tunable Emission by Post-Synthetic Modification with Lewis Acids. *J. Phys. Chem. Lett.* **2016**, *7*, 1315-1320.

[183] Tessier, M. D.; De Nolf, K.; Dupont, D.; Sinnaeve, D.; De Roo, J.; Hens, Z. Aminophosphines: A Double Role in the Synthesis of Colloidal Indium Phosphide Quantum Dots. *J. Am. Chem. Soc.* **2016**, *138*, 5923-5929.

[184] Hettick, M.; Li, H.; Lien, D.-H.; Yeh, M.; Yang, T.-Y.; Amani, M.; Gupta, N.; Chrzan, D.C.; Chueh, Y.-L.; Javey, A. Shape-Controlled Single-Crystal Growth of InP at Low Temperatures Down To 220 C. *Proc. Natl. Acad. Sci. USA* **2020**, *117*, 902-906.

[185] Biadala, L.; Siebers, B.; Beyazit, Y.; Tessier, M. D.; Dupont, D.; Hens, Z.; Yakovlev D. R.; Bayer, M. Band-Edge Exciton Fine Structure and Recombination Dynamics in InP/ZnS Colloidal Nanocrystals. *ACS Nano* **2016**, *10*, 3356-3364.

[186] Rabouw, F. T.; de Mello Donega, C. Excited-State Dynamics in Colloidal Semiconductor Nanocrystals. *Top. Curr. Chem. (Z)* **2016**, *374*, 58.

[187] Brodu, A.; Ballottin, M. V.; Buhot, J.; Harten, E. J.; Dupont, D.; Porta, A. L.; Prins, P. T.; Tessier, M. D.; Versteegh, M. A. M.; Zwiller, V.; *et al.* Exciton Fine Structure and Lattice Dynamics in InP/ZnSe Core/Shell Quantum Dots. *ACS Photonics* **2018**, *5*, 3353-3362.

[188] Kim, Y.; Ham, S.; Jang, H.; Min, J.H.; Chung, H.; Lee, J.; Kim, D.; Jang, E. Bright and Uniform Green Light Emitting InP/ZnSe/ZnS Quantum Dots for Wide Color Gamut Displays. *ACS Appl. Nano Mater.* **2019**, 2, 1496-1504.

[189] Won, Y.-H.; Cho, O.; Kim, T.; Chung, D.-Y.; Kim, T.; Chung, H.; Jang, H.; Lee, J.; Kim, D.; Jang, E. Highly Efficient and Stable InP/ZnSe/ZnS Quantum Dot Light-Emitting Diodes. *Nature* **2019**, *575*, 634-638.

[190] Janke, E. M.; Williams, N. E.; She, C.; Zherebetskyy, D.; Hudson, M. H.; Wang, L.; Gosztola, D. J.; Schaller, R. D.; Lee, B.; Sun, C.; *et al.* Origin of Broad Emission Spectra in InP Quantum Dots: Contributions from Structural and Electronic Disorder. *J. Am. Chem. Soc.* **2018**, *140*, 15791-15803.

[191] Thomas, A.; Sandeep, K.; Somasundaran, S. M.; Thomas, K. G. How Trap States Affect Charge Carrier Dynamics of CdSe and InP Quantum Dots: Visualization through Complexation with Viologen. *ACS Energy Lett.* **2018**, *3*, 2368-2375.

[192] Mićić, O. I.; Nozik, A. J.; Lifshitz, E.; Rajh, T.; Poluektov, O. G.; Thurnauer, M. C. Electron and Hole Adducts Formed in Illuminated InP Colloidal Quantum Dots Studied by Electron Paramagnetic Resonance. *J. Phys. Chem. B* **2002**, *106*, 4390-4395.

[193] Langof, L.; Ehrenfreund, E.; Lifshitz, E.; Micic, O. I.; Nozik, A. J. Continuous-Wave and Time-Resolved Optically Detected Magnetic Resonance Studies of Nonetched/Etched InP Nanocrystals. *J. Phys. Chem. B* **2002**, *106*, 1606-1612.

[194] Although this is not a realistic configuration, it represents a proof of concept to show the effect of surface P atoms.

[195] Yu, Z.; Li, J.; O'Connor, D. B.; Wang, L.-W.; Barbara, P. F. Large Resonant Stokes Shift in CdS Nanocrystals. *J. Phys. Chem. B* **2003**, *107*, 5670-5674.

[196] Ramsden, J. J.; Webber, S. E.; Grätzel M. Luminescence of Colloidal Cadmium Sulfide Particles in Acetonitrile and Acetonitrile/Water Mixtures. *J. Phys. Chem.* **1985**, *89*, 2740-2743.

[197] Hässelbarth, A.; Eychmüller, A.; Weller, H. Detection of Shallow Electron Traps in Quantum Sized CdS by Fluorescence Quenching Experiments. *Chem. Phys. Lett.* **1993**, *203*, 271-276.

[198] Sapra, S.; Mayilo, S.; Klar, T. A.; Rogach, A. L.; Feldmann, J. Bright White-Light Emission from Semiconductor Nanocrystals: by Chance and by Design. *Adv. Mater.* **2007**, *19*, 569-572.

[199] Hussein, M. T.; Kasim, T.; Abdulsattar, M. A.; Kaka, A. K. Density Functional Theory Study of InP Quantum Dot and Oxidized Surface. *IJAIEM* **2014**, *3*, 1-8.

[200] Wang , L-W.; Li, J. First-principles thousand-atom quantum dot calculations. *Phys. Rev. B* **2004**, *69*, 153302.

[201] We define as "dark" any state whose optical matrix element connecting it to the $|0h; 0e\rangle$ state is over 3 orders of magniture smaller than that relative to the absorption edge transition.

[202] Gong, K.; Zeng, Y.; Kelley, D. F. Extinction Coefficients, Oscillator Strengths, and Radiative Lifetimes of CdSe, CdTe, and CdTe/CdSe Nanocrystals. *J. Phys. Chem. C* **2013**, *117*, 20268-20279.

[203] Micic, O. I.; Smith, B. B.; Nozik, A. J. Core-Shell Quantum Dots of Lattice-Matched ZnCdSe2 Shells on InP Cores: Experiment and Theory. *J. Phys. Chem. B* **2000**, *104*, 12149-12156.

[204] Rowland, C. E.; Liu, W.; Hannah, D. C.; Chan, M. K. Y.; Talapin, D. V.; Schaller, R. D. Thermal Stability of Colloidal InP Nanocrystals: Small Inorganic Ligands Boost High-Temperature Photoluminescence. *ACS Nano* **2014**, *8*, 977-985.

[205] Mnoyan, A. N.; Kirakosyan, A. Gh.; Kim, H.; Jang, H. S.; Jeon, D. Y. Electrostatic Stabilized InP Colloidal Quantum Dots with High Photoluminescence Efficiency. *Langmuir* **2015**, *31*, 7117-7121.

[206] Micic, O. I.; Sprague, J.; Lu, Z.; Nozik, A. J. Highly Efficient Band-Edge Emission from InP Quantum Dots. *Appl. Phys. Lett.* **1996**, *68*, 3150-3152.

[207] Li, H.; Jia, C.; Meng, X.; Li, H. Chemical Synthesis and Applications of Colloidal Metal Phosphide Nanocrystals. *Front. Chem.* **2019**, *6*, 652.

[208] Shen, W.; Tang, H.; Yang, X.; Cao, Z.; Cheng, T.; Wang, X.; Tan, Z.; You, J.; Deng, Z. Synthesis of Highly Fluorescent InP/ZnS Small-Core/Thick-Shell Tetrahedral-Shaped Quantum Dots for Blue Light-Emitting Diodes. *J. Mater. Chem. C* **2017**, *5*, 8243-8249.

[209] Sills, A.; Harrison, P.; Califano, M. Exciton Dynamics in InSb Colloidal Quantum Dots. *J. Phys. Chem. Lett.* **2016**, *7*, 31-35.

[210] Chang, A. Y.; Liu, W.; Talapin, D. V.; Schaller, R. D. Carrier Dynamics in Highly Quantum-Confined, Colloidal Indium Antimonide Nanocrystals. *ACS Nano* **2014**, *8*, 8513-8519.

[211] Klimov, V. I. Optical Nonlinearities and Ultrafast Carrier Dynamics in Semiconductor Nanocrystals. *J. Phys. Chem. B* **2000**, *104*, 6112-6123.

[212] Robel, I.; Gresback, R.; Kortshagen, U.; Schaller, R. D.; Klimov, V. I. Universal Size-Dependent Trend in Auger Recombination in Direct-Gap and Indirect-Gap Semiconductor Nanocrystals. *Phys. Rev. Lett.* **2009**, *102*, 177404.

[213] Li, Y.-H.; Walsh, A.; Chen, S.; Yin, W.-J.; Yang, J.-H.; Li, J.; Da Silva, J.L.F.; Gong, X.G.; Wei, S.-H. Revised *Ab Initio* Natural Band Offsets of All Group IV, II-VI, and III-V Semiconductors. *Appl. Phys. Lett.* **2009**, *94*, 212109.

[214] Adam, S.; Talapin, D.V.; Borchert, H.; Lobo, A.; McGinley, C.; de Castro, A.R.B.; Haase, M.; Weller, H.; Möller, T. The Effect of Nanocrystal Surface Structure on the Luminescence Properties: Photoemission Study of HF-etched InP Nanocrystals. *J. Chem. Phys.* **2005**, *123*, 084706.

[215] Talapin, D. V.; Lee, J.; Kovalenko, M. V. Prospects of Colloidal Nanocrystals for Electronic and Optoelectronic Applications. *Chem. Rev.* **(2010)**, *110*, 389−458.

[216] Kovalenko, M. V.; Manna, L.; Cabot, A.; Hens, Z.; Talapin, D.V.; Kagan, C. R.; Klimov, V. I.; Rogach, A. L.; Reiss, P. D.; Milliron, J.; Guyot-Sionnnestl, P.; Konstantatos, G.; Parak, W. J.; Hyeon, T.; Korgel, B. A.; Murray, C. B.; Heiss, W. Prospects of Nanoscience with Nanocrystals *ACS Nano 9*, **(2015)**, 1012−1057.

[217] Choi, J.-H.; Fafarman, A. T.; Oh, S. J.; Ko, D. K.; Kim, D. K.; Diroll, B. T.; Muramoto, S.; Gillen, J. G.; Murray, C. B.; Kagan, C. R. Bandlike Transport in Strongly Coupled and Doped Quantum Dot Solids: a Route to High-Performance Thin-Film Electronics. *Nano Lett 12*, **(2012)**, 2631−2638.

[218] Yu, D.; Wang, C.; Wehrenberg, B. L.; Guyot-Sionnest, P. Variable Range Hopping Conduction in Semiconductor Nanocrystal Solids. *Phys. Rev. Lett. 92*, **(2004)**, 216802.

[219] Lan, X.; Chen, M.; Hudson, M.H.; Kamysbayev, V.; Wang, Y.; Guyot-Sionnest, P.; Talapin, D. V. Quantum Dot Solids Showing State-Resolved Band-Like Transport. *J. Mater. Chem. C 19*, **(2020)**, 323–329.

[220] Buurma, C.; Pimpinella, R. E.; Ciani, A. J.; Feldman, J. S.; Grein, C. H.; Guyot-Sionnest, P. MWIR Imaging with Low Cost Colloidal Quantum Dot Films *Proc. SPIE 9933*, **(2016)**, 993303.

[221] Hu, L.; Huang, S.; Patterson, R.; Halpert, J. E. Enhanced Mobility in PbS Quantum Dot Films via PbSe Quantum Dot Mixing for Optoelectronic Applications. *J. Mater. Chem. C 7*, **(2019)**, 4497-4502.

[222] Liang, R.; Yan, D.; Tian, R.; Yu, X.; Shi, W.; Li, C.; Wei, M.; Evans, D. G.; Duan, X. Quantum Dots-Based Flexible Films and Their Application as the Phosphor in White Light-Emitting Diodes. *Chem. Mater. 26*, **(2014)**, 2595–2600.

[223] Kim, T.; Lim, S.; Yun, S.; Jeong, S.; Park, T.; Choi, J. Design Strategy of Quantum Dot Thin-Film Solar Cells. *Small 16*, **(2020)**, 2002460.

[224] Xu, G.; Zeng, S.; Zhang, B.; Swihart, M. T.; Yong, K.; Prasad, P.N. New Generation Cadmium-Free Quantum Dots for Biophotonics and Nanomedicine. *Chem. Rev. 116*, **(2016)**, 12234−12327.

[225] Shabaev, A.; Efros, A. L.; Efros, A. L. Dark and Photo-Conductivity in Ordered Array of Nanocrystals. *Nano Lett. 13*, **(2013)**, 5454−5461.

[226] Lee, J. S.; Kovalenko, M. V.; Huang, J.; Chung, D. S.; Talapin, D. V. Band-Like Transport, High Electron Mobility and High Photoconductivity in All-Inorganic Nanocrystal Arrays. *Nat. Nanotechnol. 6*, **(2011)**, 348–352.

[227] D. A. Mirabella, C. M. Aldao, R. R. Deza, *Int J Quant Chem. 68*, 285-291 **(1998)**.

[228] Liu, W.; Lee, J.-S.; Talapin, D. V. III–V Nanocrystals Capped with Molecular Metal Chalcogenide Ligands: High Electron Mobility and Ambipolar Photoresponse. *J. Am. Chem. Soc. 135*, **(2013)**, 1349–1357.

[229] Okamoto, A.; Geka, H.; Shibasaki, I.; Yoshida, K. Transport Properties of InSb and InAs Thin Films on GaAs Substrates. *J.Cryst. Growth 278*, **(2005)**, 604–609.

[230] Sanehira, E.M.; Marshall, A. R.; Christians, J. A.; Harvey, S. P.; Ciesielski, P. N.; Wheeler, L. M.; Schulz, P.; Lin, L. Y.; Beard, M. C.; Luther, J. M. Enhanced Mobility $CsPbI_3$ Quantum Dot Arrays for Record-Efficiency, High-Voltage Photovoltaic Cells. *Sci. Adv. 3*, **(2017)**, eaao4204.

[231] Gomez-Campos, F. M.; Rodríguez-Bolívar, S.; Califano, M. High-Mobility Toolkit for Quantum Dot Films. *ACS Photonics 3*, **(2016)**, 2059−2067.

[232] Guyot-Sionnest, P. Electrical Transport in Colloidal Quantum Dot Films. *J. Phys. Chem. Lett. 3*, **(2012)**, 1169−1175.

[233] Yu, Z.; Li, J.; O'Connor, D. B.; Wang, L.-W.; Barbara, P. F. Large Resonant Stokes Shift in CdS Nanocrystals. *J. Phys. Chem. B 107*, **(2003)**, 5670−5674.

[234] Crisp, R. W.; Kirkwood, N.; Grimaldi, G.; Kinge, S.; Siebbeles, L. D. A.; Houtepen, A. J. Highly Photoconductive InP Quantum Dots Films and Solar Cells. *ACS Appl. Energy Mater. 1*, **(2018)**, 6569−6576.

[235] Crisp, R. W.; Callahan, R.; Reid, O. G.; Dolzhnikov, D. S.; Talapin, D. V.; Rumbles, G.; Luther, J. M.; Kopidakis, N. Effect of Metal Ions on Photoluminescence, Charge Transport, Magnetic and Catalytic Properties of All-Inorganic Colloidal Nanocrystals and Nanocrystal Solids *J. Phys. Chem. Lett. 6*, **(2015)**, 4815−4821.

[236] Zhao, T.; Goodwin, E. D.; Guo, J.; Wang, H.; Diroll, B. T.; Murray, C. B.; Kagan, C. R. Advanced Architecture for Colloidal PbS Quantum Dot Solar Cells Exploiting a CdSe Quantum Dot Buffer Layer. *ACS Nano 10*, **(2016)**, 9267−9273 .

[237] Grimaldi, G.; Crisp, R. W.; ten Brinck, S.; Zapata, F.; van Ouwendorp, M.; Renaud, N.; Kirkwood, N.; Evers, W. H.; Kinge, S.; Infante, I. ; Siebbeles, L. D. A.; Houtepen, A. J. Hot-Electron Transfer in Quantum-Dot Heterojunction Films. *Nat. Commun. 9*, **(2018)**, 2310.

[238] Rodosthenous, P.; Gómez-Campos, F. M.; Califano, M. Tuning the Radiative Lifetime in InP Colloidal Quantum Dots by Controlling the Surface Stoichiometry. *J. Phys. Chem. Lett. 11*, **(2020)**, 10124-10130.

[239] Crisp, R. W.; Hashemi, F. S. M.; Alkemade, J.; Kirkwood, N.; Grimaldi, G.; Kinge, S.; Siebbeles, L. D. A.; van Ommen, J. R.; Houtepen, A. J. Atomic Layer Deposition of ZnO on InP Quantum Dot Films for Charge Separation, Stabilization, and Solar Cell Formation *Adv. Mater. Interfaces 7*, **(2020)**, 1901600.

[240] Busatto, S.; de Ruiter, M.; Jastrzebski, J. T.; Albrecht, W.; Pinchetti, V.; Brovelli, S.; Bals, S.; Moret, M.-E.; de Mello Donega, C. Luminescent Colloidal InSb Quantum Dots from In Situ Generated Single-Source Precursor. *ACS Nano 14*, **(2020)**, 13146−13160.

[241] M. Winslow, S.H. Kodati, S. Lee, et al., *J. Electron. Mater. 50*, 7293–7302 **(2021)**.

[242] Yu, B.; Zhang, C.; Chen, L.; Qin, Z.; Huang, X.; Wang, X.; Xiao, M. Ultrafast Dynamics of Photoexcited Carriers in Perovskite Semiconductor Nanocrystals. *Nanophotonics*, **(2021)**, 20200681.

[243] Gomez-Campos, F. M.; Rodríguez-Bolívar, S.; Califano, M. Effective Approach for an Order-of-Magnitude-Accurate Evaluation of the Electron Mobility in Colloidal Quantum Dot Films *J. Nanomater. 2019*, **(2019)**, 1-9.

[244] Skibinsky-Gitlin, E. S.; Rodríguez-Bolívar, S.; Califano, M.; Gomez-Campos, F. M. Band-Like Electron Transport in 2D Quantum Dot Periodic Lattices: the Effect of Realistic Size Distributions *Phys. Chem. Chem. Phys. 21*, **(2019)**, 25872.

[245] Kim, S.; Lee, K.; Kim, S.; Kwon, O.; Heo, J. H.; Im, S. H.; Jeong, S.; Lee, D. C.; Kim, S. W. Origin of Photoluminescence from Colloidal Gallium phosphide Nanocrystals Synthesized via a Hot-Injection Method. *RSC Adv.* **2015**, *5*, 2466–2469.

[246] Dobrovolsky, Y.; Lipka, V. M.; Strebezhev, V. V.; Sorokatyi, Y. O.; Sorokatyi, M. O.; Andreeva, O. P. Photodiode Based on The Epitaxial Phosphide Gallium with Increased Sensitivity at a Wavelength of 254 nm. *Informatyka, Automatyka, Pomiary W Gospodarce I Ochronie Środowiska* **2020**, *10*, 36-39.

[247] Park, K.; Lee, J.; Kim, D.; Seo, J.; Kim, J.; Ahn, J.P.; Park J. Synthesis of Polytypic Gallium Phosphide and Gallium Arsenide Nanowires and Their Application as Photodetectors. *ACS Omega.* **2019**, *12*, 3098-3104.

[248] Lu, X.; Huang, S. R.; Diaz, M.; Opilia, R.L.; Barnett, A. Wide Band Gap Gallium Phosphide Solar Cells for Multi-Junction Solar Cell System. *35th IEEE Photovoltaic Specialists Conference.* **2010**, 002079-002083.

[249] Khosroabadi, S.; Kazemi, A. High Efficiency Gallium Phosphide Solar Cells Using TC-Doped Absorber Layer. *Physica E: Low-dimensional Systems and Nanostructure* **2018**, *104*, 116–123.

[250] Siao, H. Y.; Bunk, R. J.; Woodall, J. M. Gallium Phosphide Solar Cell Structures with Improved Quantum Efficiencies. *Journal of Elec. Materi.* **2020**, *49*, 3435–3440/

[251] Stockill, R.; Forsch, M.; Beaudoin, G.; Pantzas, K.; Sagnes, I.; Braive, R.; Gröblacher, S. Gallium Phosphide as a Piezoelectric Platform for Quantum Optomechanics. *Phys. Rev. Lett.* **2019**, *123*,163602.

[252] Tilmann, B.; Grinblat, G.; Berte, R.; Ozcan, M.; Kunzelmann, V. F.; Nickel, B.; Sharp, I. D.; Cortes, E.; Maier, S. A.; Li, Y. Nanostructured Amorphous Gallium Phosphide on Silica for Nonlinear and Ultrafast Nanophotonics. *Nanoscale Horiz.* **2020**, *5*,1500-1508.

[253] Krishna, M. V. R.; Friesner, R. A. Quantum Confinement Effects in Semiconductor Clusters. *J. Chem. Phys.* **1991**, *95*, 8309.

[254] Abdulsattar, M. A.; Hussein, M. T.; Jamal, R. K.; Kasim, T. Electronic Structure of Gallium Phosphide Nanocrystals Core and (001)-(1 × 1) Oxidized Surface. *Adv. Mat. Phys. Chem.* **2012**, *2*, 267-274.

[255] Standing, A., Assali, S., Gao, L. et al. Efficient Qater Reduction with Gallium Phosphide Nanowires. *Nat Commun.* **2015**, *6*, 7824.

[256] da Silva, B.C.; Couto, O.D.D.; Obata, H.T. et al. Optical Absorption Exhibits Pseudo-Direct Band Gap of Wurtzite Gallium Phosphide. *Sc.i Rep.* **2020**, *10*, 7904.

[257] Assali, S.; Zardo, I.; Plissard, S. et al. Direct Band Gap Wurtzite Gallium Phosphide Nanowires. *Nano Lett.* **2013**, *13*, 1559−1563.

[258] Greil, J.; Assali, S.; Isono, Y. et al. Optical Properties of Strained Wurtzite Gallium Phosphide Nanowires. *Nano Lett.* **2016**, *16*, 3703−3709.

[259] Aparna.A.R.; Brahmajirao, V.; Karthikeyan, T.V. Review on Synthesis and Characterization of Gallium Phosphide. *Procedia Materials Science* **2014**, *6*, 1650 – 1657.

[260] Maliakkal, C B.; Gokhale, M.; Parmar, J. et al. Growth, Structural and Optical Characterization of Wurtzite GaP Nanowires. *Nanotechnology* **2019**, *30*, 254002.

[261] Micic, O. I.; Sprague, J. R.; Curtis, C. J. et al. Synthesis and Characterization of InP, GaP, and $GaInP_2$ Quantum Dots. *J. Phys. Chem.* **1995**, *99*, 7754–7759.

[262] Xiaoyu, M.; Jingjing, M.; Zaiping, Z.; Garoufalis, C. S.; Baskoutas, S.; Yu, J.; Zuliang, D. Excitons in InP, GaP, and $Ga_xIn_{1-x}P$ Quantum Dots: Insights from Time-Dependent Density Functional Theory. *Phys. Rev. Lett.* **2009**, *100*, 245404.

[263] Kim, Y.; Choi, H.; Lee, Y. et al. Tailored Growth of Single-Crystalline InP Tetrapods. *Nat Commun* **2021**, *12*, 4454.

[264] Xinyao , S.; Binghan , L.; Botao, J. Synthesis of Wurtzite In and Ga Phosphide Quantum Dots Through Cation Exchange Reactions. *Chem. Mater.* **2021**, *33*, 5223–5232.

[265] Jalali, H. B.; Sadeghi, S.; Sahin, M. et al. Colloidal Aluminum Antimonide Quantum Dots . *Chem. Mater* **2019**, *31*, 4743−4747.